Alma Mater Studiorum · University of Bologna

School of Science
Department of Physics and Astronomy
Master Degree in Physics

Magnetic properties of 2D Chromium trihalides by first-principles calculations

Supervisor:
Prof. Cesare Franchini

Co-supervisor:
Dr. Leonid V. Pourovskii

Submitted by:
Matteo Costa

Academic Year 2023/2024

Abstract

This thesis investigates the magnetic properties of the chromium trihalides series CrX_3 with X = Cl, Br, I at both the bulk and monolayer limits, with a particular focus on the effect of low-dimensionality and spin-orbit coupling. Combining the four-states method with very accurate total energy calculations based on density functional theory, we have systematically targeted the isotropic and anisotropic contributions to the exchange interactions within these materials. Our findings reveal that they are significantly enhanced by the spin-orbit coupling of the associated halide atoms. To further understand the behaviour of the monolayers at finite temperatures, we initialized a quadratic spin Hamiltonian with the so obtained exchange couplings and consequently performed Monte Carlo simulations. The results indicate a substantial overestimation of the Curie temperatures for the monolayers. We finally suggest a reasonable explanation of the reported discrepancy, but that is still an open question as it would require further tests to be eventually confirmed.

Contents

List of Figures

List of Tables

Introduction

The advent of two-dimensional (2D) materials is commonly associated with the first realization and characterization of graphene [1] by A. Geim and K. Novoselov in 2004 and it paved the way to the discovery of 2D magnetic systems. Indeed, after several unsuccessful attempts to exfoliate a single layer of K_2CuF_4 following the theoretical suggestion in [2], ferromagnetism was finally reported in the CrI_3 monolayer (ML) [3] and the $CrGeTe_3$ few-layer film [4] in 2017. Prior to this discovery, long-range magnetic order in 2D systems with isotropic short-range exchange interactions was considered impossible due to the Mermin-Wagner theorem, which for instance can be violated by the effect of Spin-Orbit Coupling (SOC) on the magnetic anisotropy or by finite-size effects [5].

During the last decade, a large variety of new 2D magnetic materials were prepared experimentally, ranging from insulators such as $CrCl_3$, $CrBr_3$ and VI_3 [6] to conductors such as Fe_3GeTe_2 [7] and $CrTe_2$ [8], and they are currently regarded as important candidates for next-generation electronic, optoelectronic and spintronic applications due to their unique properties.

The growing interest in the field has highlighted the need for reliable theoretical frameworks to learn more about the underlying exchange interactions. These methods can be broadly categorized into two groups. The first case include those methods which map derivatives of the total energies with respect to the spin tilting angles onto a classical spin Hamiltonian, while those for the second one directly take the total energies of some specific magnetic configurations.

Among the latter energy-mapping techniques, the four-states methodology stands out as particularly effective and powerful, since it can be employed in any magnetic system and also allows for an extensive description of the aimed Intersite Exchange Interaction (IEI) and Single-Ion Anisotropy (SIA) tensors.

The scope of this thesis is to contribute to the current understanding of the exchange interactions in the most relevant bulk and ML phases of the chromium trihalides series CrX_3 with X = Cl, Br and I, with a particular emphasis on the role of the halide's SOC and the low-dimensionality. We thus provide a comprehensive overview of the dominant terms in the IEI and SIA tensors obtained by four-states method and compare them to the available experimental and computational estimates in the literature. To further

comment on the reliability of our finding, we plug the resulting couplings into a Monte Carlo (MC) code that allows to locate the Curie temperature of the ML phases.

In particular, the body of the thesis is structured in four Chapters as follows.

The first Chapter presents a detailed treatment of some exemplary models for the microscopic origin of magnetism, underlining the crucial role of the on-site Coulomb repulsion, the Coulomb exchange and the allowed electron hopping processes in the most common exchange mechanisms in transition metal compounds. Further, it includes a brief introduction to the main anisotropic exchange interactions and the associated quadratic spin Hamiltonians.

The second Chapter outlines the theoretical framework behind all the computational methods that lead to our results. As a first step, we discuss the conceptual core of Density Functional Theory (DFT) and derive the single-electron Kohn-Sham equations within the spin-unrestricted scheme by a variational treatment of the total energy functional. In order to compensate for the well known DFT limitations in capturing the correlation effects of localized d or f orbitals, we introduce the Dudarev's approach to Hubbard-U correction as implemented in the Vienna Ab-initio Simulation Package (VASP) software. Then, we explain how to constrain the direction of local magnetic moments in a system by adding a penalty term to the standard DFT total energy functional. At this point, we present two independent techniques to estimate the target exchange couplings, namely the four-states energy-mapping method and the magnetic force theorem within Hubbard-I (HI) approximation. Finally, we discuss the implementation of the Metropolis MC algorithm for finite-temperature calculations within the Uppsala Atomistic Spin Dynamics (UppASD) code.

The third Chapter provides a general overview of the main physical properties of the chromium trihalides under study both at the bulk and ML limit.

To conclude, the fourth Chapter consists of a summary of the results with further comments and some technical details concerning the adopted procedures.

Chapter 1

Theoretical models of magnetism

This chapter is aimed to provide an overview of the main physical mechanisms, which induce local exchange interactions in magnetic systems. Thus, we delve into a detailed description of kinetic and Coulomb exchange and how they explain the occurrence of magnetic order at finite temperatures, while magnetostatic dipoles' interaction cannot.
In particular, we distinguish between direct and indirect exchange mechanisms, including for example the so called Goodenough-Kanamori rules for superexchange, which often fit to transition metal compounds as in our case.
Finally, a brief introduction to most common anisotropic exchange interactions allows the reader to explore their effects in realistic cases.

The energy difference due to the static interaction between two magnetic dipole moments $\hat{\mu}_1$ and $\hat{\mu}_2$ located at $\mathbf{R}_1$ and $\mathbf{R}_2$ is given by

$$\Delta E_{dip} = \frac{\mu_0}{4\pi|\mathbf{R}_{12}|^3}\left[\hat{\mu}_1 \cdot \hat{\mu}_2 - \frac{3}{|\mathbf{R}_{12}|^2}(\mathbf{R}_{12} \cdot \hat{\mu}_1)(\mathbf{R}_{12} \cdot \hat{\mu}_2)\right] \tag{1.1}$$

with the dipoles' connecting vector $\mathbf{R}_{12} = \mathbf{R}_1 - \mathbf{R}_2$ and the vacuum magnetic permeability $\mu_0 = 4\pi \times 10^{-7}\ H/m$. Moreover, according to the quantum theory of angular momenta, the magnetic dipole moment of an atom is related to the spin and orbital degrees of freedom as follows

$$\hat{\mu} = -\frac{\mu_B}{\hbar}(\hat{L} + 2\hat{S}) \tag{1.2}$$

where $\hat{L}$ and $\hat{S}$ are the operators for the electronic orbital and spin angular momenta, while $\mu_B = 5.7883818060(17) \times 10^{-5}\ eV/T$ and $\hbar = 6.582119569 \times 10^{-16}\ eV \cdot s$ are the Bohr magneton and the reduced Planck constant respectively. Since the eigenvalues of $\hat{L}$ and $\hat{S}$ are usually expressed as low integer or half-integer multiples of $\hbar$, the typical

order of magnitude for the atomic magnetic moments in solid state physics does not exceed few units of μ_B. One can then conclude that the thermal energy required to prevent any magnetic ordering due to magnetostatic dipoles' interaction would be just $\sim 10^{-1} - 10^{-2}$ meV (i.e. $\sim 1 - 10^{-1}$ K in terms of temperature), which is in contrast with the experimental observation of magnetic phases in a large variety of real materials.

The origin of such phenomena is indeed ascribable to the so called exchange interactions between the local magnetic moments. In particular, we distinguish among Couolomb and kinetic exchange interactions according to the underlying physical mechanism, which are discussed in the following sections.

1.1 Coulomb exchange interaction

The well known Pauli exclusion principle states that two or more electrons cannot occupy the same quantum state simultaneously, or in other words that the associated many-electrons wavefunction must be antisymmetric with respect to particles' exchange. The latter property is of significant relevance for the Coulomb repulsion energy between them, as it turns out to encourage electrons with same spins to occupy different spatial orbitals.

We shall indeed prove this point via a simple two-electron model with an interacting Hamiltonian of the form

$$\hat{H} = \hat{H}_0 + \hat{H}_I = \sum_{i=1}^{2} \left[-\frac{1}{2}\nabla_i^2 + v(\mathbf{r}_i) \right] + \frac{1}{|\mathbf{r}_1 - \mathbf{r}_2|} \tag{1.3}$$

with $v(\mathbf{r})$ as a generic single-electron potential and $\mathbf{r}_1$, $\mathbf{r}_2$ as the position coordinates of the two electrons, adopting atomic units. Moreover, let us assume that the solution of the Schrodinger problem of the single-electron terms in $\hat{H}_0$ is already known and consists of an orthonormal set of eigenstates $\{\varphi_\alpha\}$ with associated eigenvalues $\{\epsilon_\alpha\}$.

So, given two specific orbitals $\varphi_{\alpha=a}$ and $\varphi_{\alpha=b}$, we construct the eigenstates of the unpertubed two-electrons Hamiltonian $\hat{H}_0$ in terms of Slater determinants $\{\Psi_{a\sigma;b\sigma'}\}$, as follows

$$\begin{aligned} \Psi_{a\sigma;b\sigma'}(\mathbf{r}_1, s_1; \mathbf{r}_2, s_2) &= \frac{1}{\sqrt{2}} \begin{vmatrix} \varphi_a(\mathbf{r}_1) \otimes \sigma(s_1) & \varphi_a(\mathbf{r}_2) \otimes \sigma(s_2) \\ \varphi_b(\mathbf{r}_1) \otimes \sigma'(s_1) & \varphi_b(\mathbf{r}_2) \otimes \sigma'(s_2) \end{vmatrix} = \\ &= \frac{1}{\sqrt{2}} \left[\varphi_a(\mathbf{r}_1)\varphi_b(\mathbf{r}_2) \otimes \sigma(s_1)\sigma'(s_2) - \varphi_b(\mathbf{r}_1)\varphi_a(\mathbf{r}_2) \otimes \sigma'(s_1)\sigma(s_2) \right]. \end{aligned} \tag{1.4}$$

Since $\hat{H}_0$ is not affected by the spin degrees of freedom, these four wavefunctions are in fact degenerate to the energy eigenvalue $(\epsilon_a + \epsilon_b)$.

However, that condition changes when the Coulomb interaction $\hat{H}_I$ is reintroduced. In order to reveal its effect on the energetics of the system, we shall write its matrix representation H_I by computing the following integrals

$$[H_I]_{lm} = \int \Psi_l^*(\mathbf{r}_1, s_1; \mathbf{r}_2, s_2) \frac{1}{|\mathbf{r}_1 - \mathbf{r}_2|} \Psi_m(\mathbf{r}_1, s_1; \mathbf{r}_2, s_2) d^3\mathbf{r}_1 d^3\mathbf{r}_2 \tag{1.5}$$

where the indices l, m are just a shorthand notation to label all the available Slater determinants, namely $l, m \in \{(a,\uparrow;b,\uparrow),(a,\uparrow;b,\downarrow),(a,\downarrow;b,\uparrow),(a,\downarrow;b,\downarrow)\}$. The only non-vanishing terms in H_I fall within three main case studies:

$$\begin{cases} l = m = (a,\sigma;b,\sigma) \\ l = m = (a,\sigma;b,-\sigma) & \text{with } \sigma = \uparrow,\downarrow \\ l = (a,\sigma;b,-\sigma) \neq (a,-\sigma;b,\sigma) = m \end{cases} \tag{1.6}$$

and they can be parametrized by the Coulomb integral

$$K_{ab} = \int \frac{|\varphi_a(\mathbf{r}_1)|^2 |\varphi_b(\mathbf{r}_2)|^2}{|\mathbf{r}_1 - \mathbf{r}_2|} d^3\mathbf{r}_1 d^3\mathbf{r}_2 \tag{1.7}$$

and the exchange integral

$$J_{ab} = \int \frac{\varphi_a^*(\mathbf{r}_1)\varphi_b(\mathbf{r}_1)\varphi_b^*(\mathbf{r}_2)\varphi_a(\mathbf{r}_2)}{|\mathbf{r}_1 - \mathbf{r}_2|} d^3\mathbf{r}_1 d^3\mathbf{r}_2. \tag{1.8}$$

After some trivial algebraic steps, we end up with an interacting Hamiltonian matrix of the form

$$H_I = \begin{pmatrix} K_{ab} - J_{ab} & 0 & 0 & 0 \\ 0 & K_{ab} & -J_{ab} & 0 \\ 0 & -J_{ab} & K_{ab} & 0 \\ 0 & 0 & 0 & K_{ab} - J_{ab} \end{pmatrix} \tag{1.9}$$

which is clearly symmetric and thus admits an orthonormal set of real-valued eigenvectors, namely $(1,0,0,0)$, $(0,0,0,1)$, $\frac{1}{\sqrt{2}}(0,1,1,0)$ and $\frac{1}{\sqrt{2}}(0,1,-1,0)$.

These four-dimensional vectors correspond to the Slater determinants $\Psi_{a,\uparrow;b,\uparrow}$, $\Psi_{a,\downarrow;b,\downarrow}$, $\frac{1}{\sqrt{2}}(\Psi_{a,\uparrow;b,\downarrow} + \Psi_{a,\downarrow;b,\uparrow})$ and $\frac{1}{\sqrt{2}}(\Psi_{a,\uparrow;b,\downarrow} - \Psi_{a,\downarrow;b,\uparrow})$. The first three states form a low-lying triplet with energy $\Delta E_t = K_{ab} - J_{ab}$, while the last one constitutes a singlet with higher energy $\Delta E_s = K_{ab} + J_{ab}$. Their order is demonstrated by the fact that both the Coulomb and exchange integrals are positive.

Interestingly, one can map this problem into an effective Hamiltonian

$$\begin{aligned} \hat{H}_{eff} &= \left(K_{ab} - \frac{1}{2}J_{ab}\right) \mathbb{I}_1 \otimes \mathbb{I}_2 - \frac{1}{2}\hat{\sigma}_1 \cdot \hat{\sigma}_2 = \\ &= \frac{1}{4}(\Delta E_s + 3\Delta E_t) - (\Delta E_s - \Delta E_t)\hat{s}_1 \cdot \hat{s}_2 \end{aligned} \tag{1.10}$$

by introducing the Pauli vector operator $\hat{\sigma} = (\hat{\sigma}_x, \hat{\sigma}_y, \hat{\sigma}_z)$ to represent the components of the spin-1/2 operators $\{\hat{s}_j\}$ in matrix notation as

$$s_j^x = \frac{1}{2}\sigma_x = \frac{1}{2}\begin{pmatrix} 0 & 1 \\ 1 & 0 \end{pmatrix},\ s_j^y = \frac{1}{2}\sigma_y = \frac{1}{2}\begin{pmatrix} 0 & -i \\ i & 0 \end{pmatrix},\ s_j^z = \frac{1}{2}\sigma_z = \frac{1}{2}\begin{pmatrix} 1 & 0 \\ 0 & -1 \end{pmatrix}. \tag{1.11}$$

In particular, Eq. 1.10 describes the coupling between the two spins and also allows to interpret the exchange integral as an exchange constant $J = -(\Delta E_s - \Delta E_t) = -2J_{ab}$ that favours the maximization of the total spin quantum number (i.e. Hund's first rule).

1.2 Kinetic exchange interactions

When more than one atom is involved, the electrons can perform hopping processes from one site to the others if the Pauli exclusion principle allows for it. In this sense the competition between the kinetic energy and the on-site Coulomb repulsion gains a non-trivial spin dependence, which emerges as an effective kinetic exchange interaction. The resulting effect is however influenced by the geometric arrangement of the given atoms and orbitals.

1.2.1 Direct exchange mechanism

For the sake of simplicity, we consider a minimal two-sites Hubbard model with only two atomic orbitals $\{\varphi_1, \varphi_2\}$ and also we adopt the second quantization formalism to simplify the notation of the problem. So, in the spirit of tight-binding models, we define $\hat{c}_{i\sigma}^\dagger$ ($\hat{c}_{i\sigma}$) as the creation (annihilation) operator for a spin-σ electron in the atomic orbital φ_i centered at the site i and they satisfy the usual anticommutation relation for fermions

$$\begin{cases} \{\hat{c}_{i\sigma}, \hat{c}_{j\sigma'}\} = 0 \\ \{\hat{c}_{i\sigma}^\dagger, \hat{c}_{j\sigma'}^\dagger\} = 0 \\ \{\hat{c}_{i\sigma}, \hat{c}_{j\sigma'}^\dagger\} = \delta_{ij}\delta_{\sigma\sigma'} \end{cases} \qquad \forall ij, \sigma\sigma'. \tag{1.12}$$

The Hamiltonian thus reads as

$$\hat{H} = -t\sum_{ij\sigma} \hat{c}_{j\sigma}^\dagger \hat{c}_{i\sigma} + U\sum_i \hat{n}_{i\uparrow}\hat{n}_{i\downarrow}, \tag{1.13}$$

where the first term accounts for the allowed hopping processes, while the second one represents the on-site Coulomb repulsion between electrons with opposite spins. Further, the two parameters t and U are given by the following integrals

$$t = \int \varphi_1^*(\mathbf{r}) \left[-\frac{1}{2}\nabla^2 + v(\mathbf{r})\right] \varphi_2(\mathbf{r}) d^3\mathbf{r} \tag{1.14}$$

and

$$U = \int \frac{|\varphi_i(\mathbf{r})|^2 |\varphi_i(\mathbf{r}')|^2}{|\mathbf{r} - \mathbf{r}'|} d^3\mathbf{r} d^3\mathbf{r}' \text{ with i=1,2.} \tag{1.15}$$

Then, if we choose the two-electron basis set to consist of two purely covalent states $\{\hat{c}^\dagger_{1\uparrow}\hat{c}^\dagger_{2\downarrow}|0\rangle, \hat{c}^\dagger_{1\downarrow}\hat{c}^\dagger_{2\uparrow}|0\rangle\}$ and two purely ionic states $\{\hat{c}^\dagger_{1\uparrow}\hat{c}^\dagger_{1\downarrow}|0\rangle, \hat{c}^\dagger_{2\uparrow}\hat{c}^\dagger_{2\downarrow}|0\rangle\}$ with $|0\rangle$ as the vacuum, we can write the Hamiltonian matrix as

$$H = \begin{pmatrix} 0 & 0 & -t & -t \\ 0 & 0 & +t & +t \\ -t & +t & U & 0 \\ -t & +t & 0 & U \end{pmatrix} \tag{1.16}$$

and a convienent basis for its diagonalization is given by the following linear combinations of the previous states

$$\begin{aligned} |\text{cov}_\pm\rangle &= \frac{1}{\sqrt{2}}(\hat{c}^\dagger_{2\downarrow}\hat{c}^\dagger_{1\uparrow} \pm \hat{c}^\dagger_{1\downarrow}\hat{c}^\dagger_{2\uparrow})|0\rangle, \\ |\text{ion}_\pm\rangle &= \frac{1}{\sqrt{2}}(\hat{c}^\dagger_{1\downarrow}\hat{c}^\dagger_{1\uparrow} \pm \hat{c}^\dagger_{2\downarrow}\hat{c}^\dagger_{2\uparrow})|0\rangle. \end{aligned} \tag{1.17}$$

Indeed, the eigenvalue problem of H is solved by the eigenpairs

$$\begin{aligned} |\Psi_\pm\rangle &= \frac{\left(2\sqrt{2t^2}|\text{cov}_-\rangle - 2\epsilon_\pm|\text{ion}_+\rangle\right)}{\sqrt{8t^2 + 2\epsilon_\pm^2}} \qquad & \epsilon_\pm &= \frac{U}{2} \pm \frac{\sqrt{U^2 + 16t^2}}{2} \\ |\Psi_{\text{cov}}\rangle &= |\text{cov}_+\rangle & \epsilon_{\text{cov}} &= 0 \\ |\Psi_{\text{ion}}\rangle &= |\text{ion}_-\rangle & \epsilon_{\text{ion}} &= U \end{aligned} \tag{1.18}$$

which show a non-trivial dependence on the two parameters t and U, depicted in Fig. 1.1.

In the strongly correlated limit $U >> t$, we have that the four eigenstates separate into two distinct groups: one ($|\Psi_-\rangle$, $|\Psi_{\text{cov}}\rangle$) settles down to very low energies and the other ($|\Psi_+\rangle$, $|\Psi_{\text{ion}}\rangle$) instead grows linearly with U. Moreover, due to $\epsilon_- \to 0$ the exact ground state $|\Psi_-\rangle$ reduces to $|\text{cov}_-\rangle$, implying that the lowest-energy states have mainly covalent character.

Therefore, the energetics of the system can be conveniently described using the so called downfolding technique, which exploits the latter consideration to partition the Hilbert space into lower-dimensional subspaces. This allows to project out the high-energy eigenstates and express the essential physics of the problem in terms of an effective Hamiltonian $\hat{H}_{eff}$, that in our case reads as

$$\begin{aligned} \hat{H}_{eff} &= -\frac{2t^2}{U}(\hat{c}^\dagger_{2\uparrow}\hat{c}^\dagger_{1\downarrow}\hat{c}_{1\downarrow}\hat{c}_{2\uparrow} - \hat{c}^\dagger_{2\downarrow}\hat{c}^\dagger_{1\uparrow}\hat{c}_{1\downarrow}\hat{c}_{2\uparrow} - \hat{c}^\dagger_{2\uparrow}\hat{c}^\dagger_{1\downarrow}\hat{c}_{1\uparrow}\hat{c}_{2\downarrow} + \hat{c}^\dagger_{2\downarrow}\hat{c}^\dagger_{1\uparrow}\hat{c}_{1\uparrow}\hat{c}_{2\downarrow}) = \\ &= \frac{4t^2}{U}\left(\hat{s}_1 \cdot \hat{s}_2 - \frac{\hat{n}_1\hat{n}_2}{4}\right) \end{aligned} \tag{1.19}$$

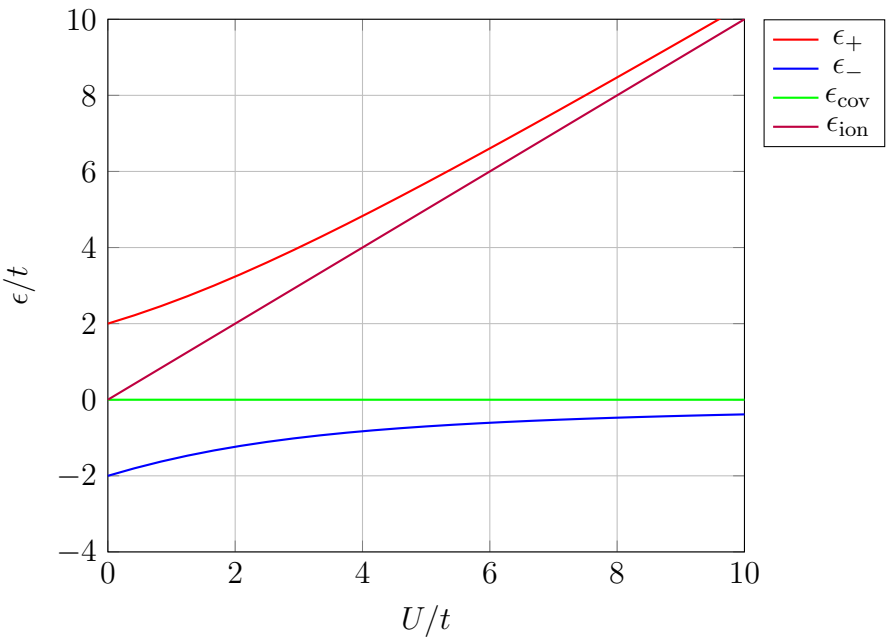

Figure 1.1: Energy spectrum of the two-sites Hubbard model. Dependence of the energy eigenvalues of the Hamiltonian in Eq. 1.13 on the on-site Coulomb repulsion parameter U.

since the components of the spin-1/2 operator $\hat{s}_j$ of the j-th site have the following second quantized form

$$\hat{s}_j^x = \frac{1}{2}(\hat{c}_{j\uparrow}^\dagger \hat{c}_{j\downarrow} + \hat{c}_{j\downarrow}^\dagger \hat{c}_{j\uparrow}) \quad \hat{s}_j^y = -\frac{i}{2}(\hat{c}_{j\uparrow}^\dagger \hat{c}_{j\downarrow} - \hat{c}_{j\downarrow}^\dagger \hat{c}_{j\uparrow}) \quad \hat{s}_j^z = \frac{1}{2}(\hat{n}_{j\uparrow} - \hat{n}_{j\downarrow}). \tag{1.20}$$

To conclude, even though the model Hamiltonian does not depend on the electrons' spins explicitly, it actually gives rise to a spin-spin interaction with a positive exchange coupling $J = 4t^2/U$. So the direct exchange mechanism favours states with antiparallel spins, leading to antiferromagnetism in real materials.

1.2.2 Antiferromagnetic superexchange

The direct exchange interaction between neighbouring spins is not always sufficient to justify the experimental observation of magnetic phases in real materials, as the inter-atomic distance can reduce considerably the overlap between the atomic orbitals. Such cases usually involve indirect exchange mechanisms, which instead are mediated by other particles or fields.

One among these is the so called superexchange mechanism that often occurs in transition metal oxides, where the localized electrons can hop from one site to the other via the intermediate O p orbital.

Similiarly to the previous section, we restrict ourselves to a system with two d orbitals centered at the two magnetic sites and a doubly-occupied p orbital connecting them, as shown in Fig. 1.2. Next, we introduce the creation (annihilation) operator for a spin-σ electron in the d orbital of the i-th site as $\hat{c}^\dagger_{i\sigma}$ ($\hat{c}_{i\sigma}$) and the creation (annihilation) operator for a spin-σ electron in the p orbital as $\hat{c}^\dagger_{p\sigma}$ ($\hat{c}_{p\sigma}$), which allow to write the Hamiltonian for a generic 180°-oriented superexchange path in second quantized form

$$\hat{H} = \epsilon_d \sum_{i\sigma} \hat{n}_{i\sigma} + \epsilon_p \sum_{\sigma} \hat{n}_{p\sigma} - t_{pd} \sum_{i\sigma} (\hat{c}^\dagger_{i\sigma}\hat{c}_{p\sigma} + \hat{c}^\dagger_{p\sigma}\hat{c}_{i\sigma}) + U_d \sum_{i} \hat{n}_{i\uparrow}\hat{n}_{i\downarrow}. \tag{1.21}$$

The first (second) term sets the energy ϵ_d (ϵ_p) of the two d (p) electrons at the atomic limit, while the third and fourth contributions account for the allowed hopping processes between the neighbouring d and p orbitals and the on-site Coulomb repulsion at each magnetic site, respectively.

By intuition, we can deduce that the lowest energy states will be those admitting two unpaired d electrons and a doubly-occupied p orbital. This means that they will differ by the relative orientation of the d-spins, specifically:

$$\begin{aligned} \text{parallel configurations:} &\quad \begin{cases} \hat{c}^\dagger_{2\uparrow}\hat{c}^\dagger_{p\downarrow}\hat{c}^\dagger_{p\uparrow}\hat{c}^\dagger_{1\uparrow}|0\rangle \\ \hat{c}^\dagger_{2\downarrow}\hat{c}^\dagger_{p\downarrow}\hat{c}^\dagger_{p\uparrow}\hat{c}^\dagger_{1\downarrow}|0\rangle \end{cases} \\ \text{antiparallel configurations:} &\quad \begin{cases} \hat{c}^\dagger_{2\uparrow}\hat{c}^\dagger_{p\downarrow}\hat{c}^\dagger_{p\uparrow}\hat{c}^\dagger_{1\downarrow}|0\rangle \\ \hat{c}^\dagger_{2\downarrow}\hat{c}^\dagger_{p\downarrow}\hat{c}^\dagger_{p\uparrow}\hat{c}^\dagger_{1\uparrow}|0\rangle \end{cases} . \end{aligned} \tag{1.22}$$

The Hilbert space generated by the first state and its elementary excitations is three-dimensional and the corresponding Hamiltonian is represented by the following 3×3 matrix

$$H^{(para)} = \begin{pmatrix} 0 & t_{pd} & t_{pd} \\ t_{pd} & U_d + \Delta_{pd} & 0 \\ t_{pd} & 0 & U_d + \Delta_{pd} \end{pmatrix} \tag{1.23}$$

with $2(\epsilon_p + \epsilon_d)$ as the zero of the energy scale and $\Delta_{pd} = \epsilon_d - \epsilon_p$. After downfolding, we end up with a scalar effective Hamiltonian matrix of the form

$$H^{(para)}_{eff} = -\frac{2t^2_{pd}}{U_d + \Delta_{pd}} \tag{1.24}$$

and the same is also valid if we start from the second state and its elementary excitations.

Differently, the Hilbert space generated by the last two states of Eq. 1.22 and their elementary excitations is nine-dimensional. So if the basis states in question are properly ordered, the Hamiltonian matrix $H^{(anti)}$ now reads as

$$\begin{pmatrix} 0 & 0 & +t_{pd} & +t_{pd} & 0 & 0 & 0 & 0 & 0 \\ 0 & 0 & 0 & 0 & +t_{pd} & +t_{pd} & 0 & 0 & 0 \\ +t_{pd} & 0 & U_d + \Delta_{pd} & 0 & 0 & 0 & -t_{pd} & 0 & -t_{pd} \\ +t_{pd} & 0 & 0 & U_d + \Delta_{pd} & 0 & 0 & 0 & -t_{pd} & -t_{pd} \\ 0 & +t_{pd} & 0 & 0 & U_d + \Delta_{pd} & 0 & +t_{pd} & 0 & +t_{pd} \\ 0 & +t_{pd} & 0 & 0 & 0 & U_d + \Delta_{pd} & 0 & +t_{pd} & +t_{pd} \\ 0 & 0 & -t_{pd} & 0 & +t_{pd} & 0 & U_d & 0 & 0 \\ 0 & 0 & 0 & -t_{pd} & 0 & +t_{pd} & 0 & U_d & 0 \\ 0 & 0 & -t_{pd} & -t_{pd} & +t_{pd} & +t_{pd} & 0 & 0 & 2U_d + 2\Delta_{pd} \end{pmatrix}, \tag{1.25}$$

which reduces to a 2×2 effective Hamiltonian matrix

$$H_{eff}^{(anti)} = -\frac{2t_{pd}^2}{U_d + \Delta_{pd}} \begin{pmatrix} 1 & 0 \\ 0 & 1 \end{pmatrix} - \frac{2t_{pd}^4}{(U_d + \Delta_{pd})^2} \left(\frac{1}{U_d} + \frac{1}{U_d + \Delta_{pd}} \right) \begin{pmatrix} +1 & -1 \\ -1 & +1 \end{pmatrix} \tag{1.26}$$

using both the downfolding technique to project out the high-energy states with at least one doubly-occupied d orbital and second-order perturbation theory. As a consequence, the associated operator only depends on the creation and annihilation operators for the d electrons as follows

$$\begin{aligned} \hat{H}_{eff}^{(anti)} = -2t_{eff}(\hat{c}_{2\uparrow}^\dagger \hat{c}_{1\downarrow}^\dagger \hat{c}_{1\downarrow} \hat{c}_{2\uparrow} + \hat{c}_{2\downarrow}^\dagger \hat{c}_{1\uparrow}^\dagger \hat{c}_{1\uparrow} \hat{c}_{2\downarrow}) - 2t_{eff}^2 \left(\frac{1}{U_d} + \frac{1}{U_d + \Delta_{pd}} \right) \cdot \\ \cdot (\hat{c}_{2\uparrow}^\dagger \hat{c}_{1\downarrow}^\dagger \hat{c}_{1\downarrow} \hat{c}_{2\uparrow} - \hat{c}_{2\downarrow}^\dagger \hat{c}_{1\uparrow}^\dagger \hat{c}_{1\downarrow} \hat{c}_{2\uparrow} - \hat{c}_{2\uparrow}^\dagger \hat{c}_{1\downarrow}^\dagger \hat{c}_{1\uparrow} \hat{c}_{2\downarrow} + \hat{c}_{2\downarrow}^\dagger \hat{c}_{1\uparrow}^\dagger \hat{c}_{1\uparrow} \hat{c}_{2\downarrow}) \end{aligned} \tag{1.27}$$

with the effective hopping parameter defined as $t_{eff} = t_{pd}^2/(U_d + \Delta_{pd})$.

This expression can be finally simplified by exploiting the relations in Eq. 1.20, which lead to

$$\hat{H}_{eff}^{(anti)} = -2t_{eff}\mathbb{I} + 4t_{eff}^2 \left(\frac{1}{U_d} + \frac{1}{U_d + \Delta_{pd}} \right) \left(\hat{s}_1 \cdot \hat{s}_2 - \frac{\hat{n}_1 \hat{n}_2}{4} \right) \tag{1.28}$$

where the effective Hamiltonian is decomposed into a constant additive term and a spin-spin interaction energy that clearly reminds the last step in Eq. 1.19 for the direct exchange mechanism. Indeed, the factor to the left of the spin operators can be interpreted again as an antiferromagnetic exchange coupling J that is now given by

$$J = 4t_{eff}^2 \left(\frac{1}{U_d} + \frac{1}{U_d + \Delta_{pd}} \right). \tag{1.29}$$

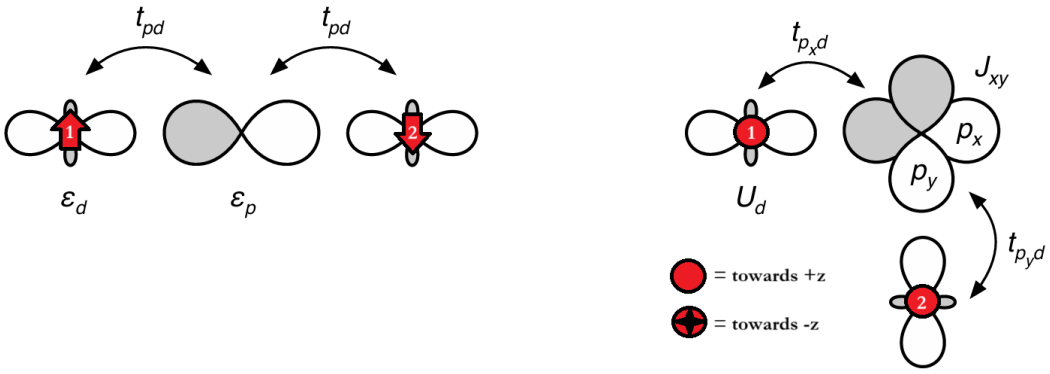

Figure 1.2: (Orbitals' orientation for AFM and FM superexchange models) Pictorial representation of the geometrical arrangement of the p and d orbitals adopted in the treatment of 180°-oriented (left) and 90°-oriented (right) superexchange mechanisms. Source: [9].

1.2.3 Ferromagnetic superexchange

As suggested by the curly arrows in Fig. 1.2, the hopping processes between p and d orbitals strongly depend on their relative orientation. Indeed, while the 180° configuration on the left only requires a single p orbital to accomplish an effective electron transfer between the two magnetic sites, for the 90° path on the right it is not sufficient. Thus, we have to introduce the p_x and p_y orbitals, respectively pointing towards the d orbital on site 1 and 2. This results in two main hopping channels (i.e. p_x-d_1 and p_y-d_2) with associated energies $t_{px,d} = t_{py,d}$ $(= t_{pd})$ and a new model Hamiltonian of the form

$$\begin{aligned}\hat{H} =&\epsilon_d \sum_{i\sigma} \hat{n}_{i\sigma} + \epsilon_p \sum_{\substack{p\sigma \\ p\in\{x,y\}}} \hat{n}_{p\sigma} - t_{pd} \sum_{\sigma} (\hat{c}^\dagger_{1\sigma}\hat{c}_{x\sigma} + \hat{c}^\dagger_{x\sigma}\hat{c}_{1\sigma} + \hat{c}^\dagger_{2\sigma}\hat{c}_{y\sigma} + \hat{c}^\dagger_{y\sigma}\hat{c}_{2\sigma}) + \\ &+ U_d \sum_i \hat{n}_{i\uparrow}\hat{n}_{i\downarrow} - J_{xy} \sum_{\sigma} \hat{n}_{x\sigma}\hat{n}_{y\sigma}\end{aligned} \tag{1.30}$$

that basically coincides with Eq. 1.21 if it was not for the creation-annihilation pair $\hat{c}^\dagger_{x\sigma}$, $\hat{c}_{x\sigma}$ ($\hat{c}^\dagger_{y\sigma}$, $\hat{c}_{y\sigma}$) for a spin-σ electron in the p_x (p_y) orbital and the Coulomb exchange interaction between p-electrons at the intermediary site.

Due to the on-site Coulomb repulsion between d-electrons we expect the states with at least one doubly-occupied d orbital to be at higher energy than the others. So again we can separate the states of the latter group into parallel and antiparallel configurations of the unpaired d-electrons' spins, as follows

$$\begin{aligned} \text{parallel configurations:} \quad & \begin{cases} \hat{c}^\dagger_{1\uparrow}\hat{c}^\dagger_{x\downarrow}\hat{c}^\dagger_{x\uparrow}\hat{c}^\dagger_{y\downarrow}\hat{c}^\dagger_{y\uparrow}\hat{c}^\dagger_{2\uparrow}|0\rangle \\ \hat{c}^\dagger_{1\downarrow}\hat{c}^\dagger_{x\downarrow}\hat{c}^\dagger_{x\uparrow}\hat{c}^\dagger_{y\downarrow}\hat{c}^\dagger_{y\uparrow}\hat{c}^\dagger_{2\downarrow}|0\rangle \end{cases} \\ \text{antiparallel configurations:} \quad & \begin{cases} \hat{c}^\dagger_{1\uparrow}\hat{c}^\dagger_{x\downarrow}\hat{c}^\dagger_{x\uparrow}\hat{c}^\dagger_{y\downarrow}\hat{c}^\dagger_{y\uparrow}\hat{c}^\dagger_{2\downarrow}|0\rangle \\ \hat{c}^\dagger_{1\downarrow}\hat{c}^\dagger_{x\downarrow}\hat{c}^\dagger_{x\uparrow}\hat{c}^\dagger_{y\downarrow}\hat{c}^\dagger_{y\uparrow}\hat{c}^\dagger_{2\uparrow}|0\rangle \end{cases} \end{aligned} \quad . \tag{1.31}$$

In particular, the Hilbert space generated by each of the first two states and their elementary excitations is four-dimensional, implying that if the basis states of interest are properly ordered the Hamiltonian of Eq. 1.30 can be represented as the 4×4 matrix

$$H^{(para)} = \begin{pmatrix} 0 & t_{pd} & t_{pd} & 0 \\ t_{pd} & U_d + \Delta_{pd} & 0 & t_{pd} \\ t_{pd} & 0 & U_d + \Delta_{pd} & t_{pd} \\ 0 & t_{pd} & t_{pd} & 2U_d + 2\Delta_{pd} - J_{xy} \end{pmatrix} \tag{1.32}$$

which reduces to a mere scalar effective Hamiltonian

$$H^{(para)}_{eff} = -\frac{2t^2_{pd}}{U_d + \Delta_{pd}} - \frac{4t^4_{pd}}{(U_d + \Delta_{pd})^2} \frac{1}{2(U_d + \Delta_{pd}) - J_{xy}} \tag{1.33}$$

by projecting out the high-energy states with doubly-occupied d orbitals using the downfolding technique.

However, the relevant physical considerations pertain to the remaining two states in Eq. 1.31, namely those from the antiparallel configurations. Not only they generate a eight-dimensional Hilbert space with all their elementary excitations, but also they allow to compute the 8×8 Hamiltonian matrix $H^{(anti)}$

$$\begin{pmatrix} 0 & 0 & t_{pd} & 0 & t_{pd} & 0 & 0 & 0 \\ 0 & 0 & 0 & t_{pd} & 0 & t_{pd} & 0 & 0 \\ t_{pd} & 0 & U_d + \Delta_{pd} & 0 & 0 & 0 & t_{pd} & 0 \\ 0 & t_{pd} & 0 & U_d + \Delta_{pd} & 0 & 0 & 0 & t_{pd} \\ t_{pd} & 0 & 0 & 0 & U_d + \Delta_{pd} & 0 & t_{pd} & 0 \\ 0 & t_{pd} & 0 & 0 & 0 & U_d + \Delta_{pd} & 0 & t_{pd} \\ 0 & 0 & t_{pd} & 0 & t_{pd} & 0 & 2U_d + 2\Delta_{pd} & -J_{xy} \\ 0 & 0 & 0 & t_{pd} & 0 & t_{pd} & -J_{xy} & 2U_d + 2\Delta_{pd} \end{pmatrix} \tag{1.34}$$

Since now two states with unpaired d-electrons are actually included in the Hilbert space under study, the downfolding technique provides a 2×2 effective Hamiltonian matrix that reads as

$$
\begin{aligned}
H_{eff}^{(anti)} = & -\frac{2t_{pd}^2}{U_d+\Delta_{pd}}\begin{pmatrix}1 & 0\\ 0 & 1\end{pmatrix} - \frac{4t_{pd}^4}{(U_d+\Delta_{pd})^2}\frac{1}{4(U_d+\Delta_{pd})^2 - J_{xy}^2}\cdot \\
& \cdot\begin{pmatrix}2U_d+2\Delta_{pd} & J_{xy}\\ J_{xy} & 2U_d+2\Delta_{pd}\end{pmatrix} = \\
= & -\left[\frac{2t_{pd}^2}{U_d+\Delta_{pd}} + \frac{4t_{pd}^4}{(U_d+\Delta_{pd})^2}\frac{1}{2(U_d+\Delta_{pd})-J_{xy}}\right]\begin{pmatrix}1 & 0\\ 0 & 1\end{pmatrix} + \\
& + \frac{4t_{pd}^4}{(U_d+\Delta_{pd})^2}\frac{J_{xy}}{4(U_d+\Delta_{pd})^2 - J_{xy}^2}\begin{pmatrix}+1 & -1\\ -1 & +1\end{pmatrix}.
\end{aligned}
\tag{1.35}
$$

In analogy to Eq. 1.26, it can be mapped into an interacting spin Hamiltonian with a negative exchange coupling

$$
J = -\frac{4t_{pd}^4}{(U_d+\Delta_{pd})^2}\frac{2J_{xy}}{4(U_d+\Delta_{pd})^2 - J_{xy}^2}, \tag{1.36}
$$

which favours the ferromagnetic alignment of the d-electrons' spins and shows a non-linear dependence on the Coulomb exchange interaction parameter J_{xy} for the p_x and p_y orbitals.

Despite the similarities of the here presented models for the superexchange interaction, the predicted couplings (i.e. Eqs. 1.29 and 1.36) even have opposite signs, implying that the angle between the magnetic and intermediary sites is a key feature for such kind of exchange mechanisms. This was in fact demonstrated by Goodenough and Kanamori in the papers [10–12], summarizing their findings in the form of two rules:

1. The electrons can only hopping between non-orthogonal orbitals with a non-negligible overlap.

2. The effective interaction for the 180°(90°)-oriented superexchange path is antiferromagnetic (ferromagnetic).

The validity of the latter statement may be compromised for example when various exchange mechanisms compete with each other or when the distinctive angle deviates from 180° and 90°.

1.3 Anisotropic exchange interactions

If we restrict ourselves to a quadratic dependence on the spin operators, the least symmetrical expression for the Hamiltonian describing the IEIs within a generic system of N spins reads as

$$\hat{H}_{IEI} = \sum_{\substack{ij,\alpha\beta \\ i<j}} \hat{S}^{(i)}_{\alpha} J^{(ij)}_{\alpha\beta} \hat{S}^{(j)}_{\beta}, \tag{1.37}$$

which features $\hat{S}^{(i)}_{\alpha}$ and $J^{(ij)}_{\alpha\beta}$ respectively as the α-th component of the i-th spin operator and the IEI tensor element which couples $\hat{S}^{(i)}_{\alpha}$ to $\hat{S}^{(j)}_{\beta}$. In particular, since there are no specific requirements on the values of the IEI tensor elements, all the possible contributions are actually taken into account.

The leading term in Eq. 1.37 usually involves the diagonal elements of the IEI tensors and follows the prescriptions of the well known Heisenberg model

$$\hat{H}_{heis} = \sum_{ij,\, i<j} \bar{J}^{(ij)} \hat{S}^{(i)} \cdot \hat{S}^{(j)} \rightsquigarrow J^{(ij)} = \begin{pmatrix} \bar{J}^{(ij)} & 0 & 0 \\ 0 & \bar{J}^{(ij)} & 0 \\ 0 & 0 & \bar{J}^{(ij)} \end{pmatrix} \tag{1.38}$$

where the IEI tensor is assumed to be fully rotational invariant. In this sense the associated energy is isotropic, meaning that it only depends on the relative orientation of the spins regardless of the crystalline axes.

Hence we can introduce anisotropy by breaking such a rotational symmetry condition on the IEI tensor. As an example, we may allow the diagonal elements $\{J^{(ij)}_{\alpha\alpha}\}$ to deviate from the isotropic contribution $\bar{J}^{(ij)}$ and thus to assign a preferential direction or plane for the spins' alignment. This case is in fact described by the so called XXZ and XYZ Heisenberg models, which only differ by the number of degenerate diagonal elements (i.e. two for XXZ and one for XYZ) and are encoded by the Hamiltonians

$$\hat{H}_{XXZ} = \sum_{ij,\, i<j} \left[J^{(ij)}_{xx} \left(\hat{S}^{(i)}_{x} \hat{S}^{(j)}_{x} + \hat{S}^{(i)}_{y} \hat{S}^{(j)}_{y} \right) + J^{(ij)}_{zz} \hat{S}^{(i)}_{z} \hat{S}^{(j)}_{z} \right] \rightsquigarrow J^{(ij)} = \begin{pmatrix} J^{(ij)}_{xx} & 0 & 0 \\ 0 & J^{(ij)}_{xx} & 0 \\ 0 & 0 & J^{(ij)}_{zz} \end{pmatrix}$$

$$\hat{H}_{XYZ} = \sum_{ij,\, i<j} \left[J^{(ij)}_{xx} \hat{S}^{(i)}_{x} \hat{S}^{(j)}_{x} + J^{(ij)}_{yy} \hat{S}^{(i)}_{y} \hat{S}^{(j)}_{y} + J^{(ij)}_{zz} \hat{S}^{(i)}_{z} \hat{S}^{(j)}_{z} \right] \rightsquigarrow J^{(ij)} = \begin{pmatrix} J^{(ij)}_{xx} & 0 & 0 \\ 0 & J^{(ij)}_{yy} & 0 \\ 0 & 0 & J^{(ij)}_{zz} \end{pmatrix} \tag{1.39}$$

For instance, by setting $J^{(ij)}_{xx} = J^{(ij)}_{yy} = 0$ we can also recover the Ising limit, which admits exact analytical solutions in one and two dimensions and often serves as a benchmark for testing novel computational techniques. However, since the size of the diagonal anisotropic exchange interactions is typically much weaker than the associated isotropic contribution, it is hardly applicable to real materials.

For what regards the off-diagonal terms instead, we shall distinguish among the symmetric and antisymmetric parts of the IEI tensor. Indeed, the first one is usually indicated as $\Gamma^{(ij)}$ and represented by the following 3×3 matrix

$$\Gamma^{(ij)} = \begin{pmatrix} \Gamma_{xx}^{(ij)} & \Gamma_{xy}^{(ij)} & \Gamma_{xz}^{(ij)} \\ \Gamma_{xy}^{(ij)} & \Gamma_{yy}^{(ij)} & \Gamma_{yz}^{(ij)} \\ \Gamma_{xz}^{(ij)} & \Gamma_{yz}^{(ij)} & \Gamma_{zz}^{(ij)} \end{pmatrix} \tag{1.40}$$

with six inequivalent elements, which couple the components of the i-th and j-th spin operators in the same fashion as Eq. 1.37 for the whole IEI tensor.

On the other hand, the antisymmetric part can be mapped into a three-dimensional vector $\vec{D}^{(ij)}$ in such a way that the corresponding Hamiltonian term reads as

$$\hat{H}_{DM} = \sum_{ij,\, i<j} \vec{D}^{(ij)} \cdot (\hat{S}^{(i)} \times \hat{S}^{(j)}) \quad \text{with} \begin{cases} D_x^{(ij)} = \frac{1}{2}(J_{yz}^{(ij)} - J_{zy}^{(ij)}) \\ D_y^{(ij)} = \frac{1}{2}(J_{zx}^{(ij)} - J_{xz}^{(ij)}) \\ D_z^{(ij)} = \frac{1}{2}(J_{xy}^{(ij)} - J_{yx}^{(ij)}). \end{cases} \tag{1.41}$$

This is commonly known as the Dzyaloshinskii-Moriya (DM) interaction [13, 14] after the name of the two theoretical physicists, who identified its microscopic origin through a second-order perturbative analysis of the SOC interaction and also provided a set of rules for $\vec{D}^{(ij)}$. The key points are briefly enumerated in Tab. 1.1.

Local symmetry	Condition	Effect on DM vector
Inversion	Center of inversion coincides with C	$\vec{D}^{(ij)} = 0$
Reflection	Mirror plane $\perp$ AB passes through C	$\vec{D}^{(ij)} \parallel$ mirror plane
	Mirror plane includes both A and B	$\vec{D}^{(ij)} \perp$ mirror plane
Rotation	Two-fold rot. axis $\perp$ AB passes through C	$\vec{D}^{(ij)} \perp$ rot. axis
	n-fold rot. axis passes through A and B	$\vec{D}^{(ij)} \perp$ rot. axis

Table 1.1: Summary of the Moriya rules. Schematic representation of the effect of local crystal symmetries on the orientation of the DM vector, given that A, B and C indicate the two associated magnetic sites and the midpoint of the line connecting them respectively.

In addition, since the spin operators enter Eq. 1.41 in the form of a cross product, the DM interaction acts as a source of spin canting in otherwise collinear magnetic phases and thus leads exotic magnetic phenomena, such as spin spirals and skyrmions.

Another interesting feature of anisotropic exchange interactions involves the experimental observation of magnetic ordering in 2D materials. As a matter of fact, the Mermin-Wagner theorem [15] provides a remarkable result of statistical mechanics and quantum field theory, asserting that any 1D or 2D system with continuous symmetry and short-range interactions (e.g. fully rotational invariant IEI tensors) cannot exhibit spontaneous symmetry breaking at finite temperatures due to the low energy cost to excite

long-wavelength thermal fluctuations. So the emergence of non-negligible anisotropic contributions is a sufficient condition to yield a violation of the initial assumptions and thus help the system to stabilize long-range order.

Chapter 2

Computational methods

During the last decades, several numerical techniques have been developed and employed by researchers to investigate the exotic phenomena associated to materials with strongly correlated electrons. At the heart of many of these tools we find DFT either within its Local Density Approximation (LDA) or Generalized Gradient Approximation (GGA) schemes, which alone are not sufficient to assess their physical properties with high precision.
Since chromium trihalides are featured by strong electronic correlations, as well as SOC, we present two of the solutions available in literature to overcome these limitations: firstly the Dudarev's approach to the Hubbard-U correction and secondly the formulation of a DFT+DMFT framework within the HI approximation, where DMFT stands for Dynamical Mean Field Theory. The resulting magnetic interactions are thus computed by two independent techniques, namely the four-states energy-mapping method and the magnetic force theorem within HI approximation.
Finally, we employ Monte Carlo simulations for the determination of some thermodynamical properties, such as the critical temperature, from the temperature dependence of the average magnetization.

2.1 Density Functional Theory

The conceptual core and the most relevant equations of DFT were first outlined by the papers [16,17] of Hohenberg, Kohn and Sham in 1964 and 1965, respectively. In the next years, they were followed by the implementation of several DFT-based codes, such as VASP [18–20], which have led the scientific community to ground-breaking achievements in the fields of chemistry, materials' science and condensed matter physics.

One of the main advantages of DFT against other quantum mechanical methods is

indeed to solve the so called many-electrons Schrödinger problem employing a variational principle on the total energy with respect to the net electron density, rather than the individual electron orbitals. This aspect in particular significantly reduces the computational effort required to perform such a task with high accuracy and predicting power.

Even though it serves as a valuable tool for the development of new materials and the elucidation of the underlying physical mechanisms of existing ones, it does have certain limitations. As a matter of fact, scientists have faced and continue to face challenges in elaborating more advanced theoretical frameworks. These include the formulation of novel exchange-correlation functionals (e.g. PBE [21], SCAN [22], etc.), hybrid functionals (e.g. HSE [23], PBE0 [24], B3LYP [25], etc.) and Hubbard-U corrections (e.g. Liechtenstein's or Dudarev's approaches [26, 27]), as well as the integration of DFT with quantum many-body techniques such as GW [28] and DMFT [29].

2.1.1 The Hohenberg-Kohn formulation

A generic system of N electrons with coordinates $\{\mathbf{r}_i\}_{i=1}^N$ and an external environment with M nuclei fixed at the sites $\{\mathbf{R}_n\}_{n=1}^M$ is described by the following electronic Hamiltonian in atomic units

$$\begin{aligned}\hat{H}_e &= \hat{T}_e + \hat{U}_{ee} + \hat{U}_{en} = \\ &= -\frac{1}{2}\sum_{i=1}^{N}\nabla_i^2 + \frac{1}{2}\sum_{\substack{i,j=1\\ i\neq j}}^{N}\frac{1}{|\mathbf{r}_i-\mathbf{r}_j|} - \sum_{n=1}^{M}\sum_{i=1}^{N}\frac{Z_n}{|\mathbf{r}_i-\mathbf{R}_n|}\end{aligned} \tag{2.1}$$

with $\hat{T}_e$ as the electronic kinetic energy and $\hat{U}_{ee}$, $\hat{U}_{en}$ as the Coulomb potential energies from the pairwise electrons-electrons repulsion and the electrons-nuclei attraction. For the sake of completeness, the symbol Z_n stands for the atomic number of the n-th nucleus in the system.

According to the Born-Oppenheimer approximation, the nuclear and electronic degrees of freedom can be treated separately due to the huge mass ratio $\frac{m_n}{m_e} \sim 10^3 - 10^4$, implying that any functional dependence on the nuclear coordinates $\{\mathbf{R}_n\}$ reduces to a mere parametrization. Thus, the electrons-nuclei Coulomb interaction becomes a system-dependent single-electron external potential $v_{ext}(\mathbf{r})$ that modifies the electronic Hamiltonian to

$$\hat{H}_e = \sum_{i=1}^{N}\left[-\frac{1}{2}\nabla_i^2 + v_{ext}(\mathbf{r}_i)\right] + \frac{1}{2}\sum_{\substack{i,j=1\\ i\neq j}}^{N}\frac{1}{|\mathbf{r}_i-\mathbf{r}_j|}. \tag{2.2}$$

The electronic Schrödinger problem is then given by

$$\hat{H}_e\Psi(\{\mathbf{r}_i\}) = \epsilon\Psi(\{\mathbf{r}_i\}) \tag{2.3}$$

with Ψ and ϵ as an energy eigenfunction that can be expressed as one or a linear combination of Slater determinants of single-electron wavefunctions $\{\psi_i(\mathbf{r}_i)\}$ due to Pauli exclusion principle and the associated energy eigenvalue.

As mentioned above, DFT addresses this assignment by a variational approach to the total energy

$$E_0 \leq \langle \Psi | \hat{H}_e | \Psi \rangle \tag{2.4}$$

in terms of the electron density ρ, which is normalized to N and defined as

$$\rho(\mathbf{r}) = \sum_{i=1}^{N} |\psi_i(\mathbf{r})|^2, \tag{2.5}$$

aiming at the estimation of the ground-state energy E_0.

Now, the work of Hohenberg and Kohn [16] provides us with a solid link between ρ and the ground-state properties of the many-electrons system.

For instance, the first Hohenberg-Kohn theorem states that the external potential $v_{ext}(\mathbf{r})$ is uniquely determined by the ground-state electron density ρ_0 up to a constant shift, allowing us to indicate it in the functional form $v_{ext}[\rho]$. This also implies that any other observable can be expressed as a functional of the electron density and the total energy is no exception, indeed:

$$E[\rho] = F_{HK}[\rho] + \int \rho(\mathbf{r}) v_{ext}[\rho](\mathbf{r}) d^3\mathbf{r} \tag{2.6}$$

where the first term derives from the kinetic energy and the electron-electron Coulomb interaction, while the second one accounts for the energy contribution from the external potential. Since ideally $F_{HK}[\rho]$ would fit to any system, it goes under the name of the universal Hohenberg-Kohn functional. However, its exact analytical expression is still unknown. Hence one usually takes good approximations for it, which as a drawback make it strongly system-dependent. For example, in non-relativistic cases the Levy constrained-search method can be used to obtain an estimate of $F_{HK}[\rho]$ as

$$F_{HK}[\rho] = min_{\Psi \to \rho} \langle \Psi | \hat{T}_e + \hat{U}_{ee} | \Psi \rangle \tag{2.7}$$

with the minimization process confined to all the many-electrons wavefunctions Ψ that yield the electron density ρ and also are eigenfunctions of the $\hat{S}^2$ operator.

On the other hand, the second Hohenberg-Kohn theorem offers the actual variational principle for the total energy functional in Eq. 2.6. In fact, any well-defined electron density leads to

$$E_0 \leq E[\rho] \tag{2.8}$$

in the same fashion as Eq. 2.4.

The here presented treatment has discarded the occurrence of energy degeneracies so far, but it is actually a recurring eventuality in the study of magnetic systems where the spin degrees of freedom play an essential role.

For spin-polarized calculations, the electron density can be separated into spin-up (α) and spin-down (β) terms, as follows

$$\rho(\mathbf{r}) = \rho_\alpha(\mathbf{r}) + \rho_\beta(\mathbf{r}), \tag{2.9}$$

which respectively integrate to the number of spin-up N_α and spin-down electrons N_β with the constraint $N = N_\alpha + N_\beta$. So the total energy functional becomes

$$E[\rho_\alpha, \rho_\beta] = F_{HK}[\rho_\alpha, \rho_\beta] + \int [\rho_\alpha(\mathbf{r}) + \rho_\beta(\mathbf{r})] v_{ext}[\rho_\alpha, \rho_\beta](\mathbf{r}) d^3\mathbf{r} \tag{2.10}$$

with the universal Hohenberg-Kohn functional in the Levy constrained-search formalism as

$$F_{HK}[\rho_\alpha, \rho_\beta] = min_{\Psi \to \rho_\alpha, \rho_\beta} \langle \Psi | \hat{T}_e + \hat{U}_{ee} | \Psi \rangle. \tag{2.11}$$

Finally, the variational principle is straightforwardly given by

$$E_0 \leq E[\rho_\alpha, \rho_\beta]. \tag{2.12}$$

2.1.2 The Kohn-Sham scheme

Despite the exactness of the Hohenberg-Kohn formulation of DFT, it also presents some non-trivial computational challenges: one for all, the approximation of the universal Hohenberg-Kohn functional.

The solution proposed by Kohn and Sham in the paper [17] consists of introducing a reference system of non-interacting electrons with the same electron density of the true system of interacting electrons. Hereafter any physical quantity A of the reference system will be labeled by a subscript character s, namely A_s.

Under such notation, this condition reads as

$$\rho(\mathbf{r}) = \rho_s(\mathbf{r}), \tag{2.13}$$

but it is important to stress that the existence of the fictitious system is already quite a strong assumption, since that is not always guaranteed.

Two different paths may be chosen to proceed with the treatment at issue: the so called spin-restricted and spin-unrestricted schemes.

In the first case, only the total electron densities of the two systems are required to meet the condition in Eq. 2.13, while in the second one both the spin-up and spin-down components must agree. Indeed, the two approaches are basically equivalent for closed-shell systems where $N_\alpha = N_\beta = \frac{N}{2}$, but they strongly differ for open-shell ones.

Since magnetism predominantly occurs in open-shell systems, we focus on the spin-unrestricted scheme, which can also be regarded as a generalization of the other one.

In particular, the Hamiltonian for the reference system reads as

$$\hat{H}_s = \sum_{i=1}^{N} \left\{ -\frac{1}{2}\nabla_i^2 + \left[v_s^{\alpha}(\mathbf{r}_i) \left|\downarrow\right\rangle \left\langle\downarrow\right| + v_s^{\beta}(\mathbf{r}_i) \left|\uparrow\right\rangle \left\langle\uparrow\right| \right] \right\} \tag{2.14}$$

with $v_s^{\alpha}(\mathbf{r})$ and $v_s^{\beta}(\mathbf{r})$ being spin-dependent external potentials, which can be interpreted as if an inhomogeneous magnetic field of the form

$$\vec{B}(\mathbf{r}) = (0, 0, B_z(\mathbf{r}) \text{ with } B_z(\mathbf{r}) = -2v_s^{SPIN}(\mathbf{r}) = [v_s^{\beta}(\mathbf{r}) - v_s^{\alpha}(\mathbf{r})] \tag{2.15}$$

was applied to the electrons' spins on top of a spin-independent external potential $v_s(\mathbf{r}) = \frac{1}{2}[v_s^{\alpha}(\mathbf{r}) + v_s^{\beta}(\mathbf{r})]$. This is supported by the following equalities

$$\begin{aligned}
\hat{H}_s &= \sum_{i=1}^{N} \left\{ -\frac{1}{2}\nabla_i^2 + \left[\left(v_s(\mathbf{r}_i) + v_s^{SPIN}(\mathbf{r}_i)\right) \left|\downarrow\right\rangle \left\langle\downarrow\right| + \left(v_s(\mathbf{r}_i) - v_s^{SPIN}(\mathbf{r}_i)\right) \left|\uparrow\right\rangle \left\langle\uparrow\right| \right] \right\} \\
&= \sum_{i=1}^{N} \left\{ -\frac{1}{2}\nabla_i^2 + \left[v_s(\mathbf{r}_i) \left(\left|\downarrow\right\rangle \left\langle\downarrow\right| + \left|\uparrow\right\rangle \left\langle\uparrow\right| \right) + v_s^{SPIN}(\mathbf{r}_i) \left(\left|\downarrow\right\rangle \left\langle\downarrow\right| - \left|\uparrow\right\rangle \left\langle\uparrow\right| \right) \right] \right\} \\
&= \sum_{i=1}^{N} \left\{ -\frac{1}{2}\nabla_i^2 + v_s(\mathbf{r}_i) - v_s^{SPIN}(\mathbf{r}_i)\hat{\sigma}_z^i \right\} \\
&= \sum_{i=1}^{N} \left\{ -\frac{1}{2}\nabla_i^2 + v_s(\mathbf{r}_i) + B_z(\mathbf{r}_i)\hat{S}_z^i \right\}
\end{aligned} \tag{2.16}$$

where $\hat{\sigma}_z^i$ is the third component of the Pauli vector operator of the i-th electron.

The Schrodinger equation for such a Hamiltonian is solved by a Slater determinant with single-electron spatial orbitals $\{\phi_i^{\alpha}, \phi_i^{\beta}\}$ which depend on the associated spin factors.

Therefore, we can separate the problem in the two spin channels and thus find the single-electron equations

$$\left[-\frac{1}{2}\nabla_i^2 + v_s^{\gamma}(\mathbf{r}) \right] \phi_i^{\gamma}(\mathbf{r}) = \epsilon_i^{\gamma}\phi_i^{\gamma}(\mathbf{r}) \text{ with } \gamma = \alpha, \beta \tag{2.17}$$

that must hold alongside with the following orthonormality conditions for the spatial orbitals

$$\langle \phi_i^{\alpha} | \phi_j^{\alpha} \rangle = \langle \phi_i^{\beta} | \phi_j^{\beta} \rangle = \delta_{ij}. \tag{2.18}$$

In addition, using the last step of Eq. 2.16 and the linearity of the commutator in both the arguments, we can also conclude that

$$
\begin{aligned}
[\hat{H}_s, \hat{S}_z] &= \sum_{i=1}^{N} \left[-\frac{1}{2}\nabla_i^2 + v_s(\mathbf{r}_i) \right] \cdot [\mathbb{I}, \hat{S}_z] + \sum_{i=1}^{N} B_z(\mathbf{r}_i)[\hat{S}_z^i, \hat{S}_z] = \\
&= \sum_{i=1}^{N} \left[-\frac{1}{2}\nabla_i^2 + v_s(\mathbf{r}_i) \right] \cdot \sum_{i=1}^{N} [\mathbb{I}, \hat{S}_z^i] + \sum_{i,j=1}^{N} B_z(\mathbf{r}_i)[\hat{S}_z^i, \hat{S}_z^j] = 0
\end{aligned}
\tag{2.19}
$$

which allows the Slater determinant given by the solutions of Eq. 2.17 to be an eigenfunction of the $\hat{S}_z$ operator with the associated eigenvalue M_s satisfying $|M_s| \leq S$. Furthermore, since the ground-state configuration is found by filling all the spatial orbitals of Eq. 2.17 from the lowest energy upwards, the value for M_s is fixed by the difference in population of the two available spin channels.

In analogy to Eq. 2.10 from the previous section, the total energy functional for the reference system reads as

$$
E_s[\rho_\alpha, \rho_\beta] = T_s[\rho_\alpha, \rho_\beta] + \int \rho_\alpha(\mathbf{r}) v_s^\alpha[\rho_\alpha, \rho_\beta](\mathbf{r}) d^3\mathbf{r} + \int \rho_\beta(\mathbf{r}) v_s^\beta[\rho_\alpha, \rho_\beta](\mathbf{r}) d^3\mathbf{r} \tag{2.20}
$$

with two main differences: firstly the universal Hohenberg-Kohn functional reduces a kinetic energy functional due to the absence of electron-electron interactions and secondly the volume integration for the external potential separates into two additional terms because of the two spin-dependent potentials.

For what regards the true system of interacting electrons instead, the universal Hohenberg-Kohn functional has the non-trivial form

$$
F_{HK}[\rho_\alpha, \rho_\beta] = T_s[\rho_\alpha, \rho_\beta] + J[\rho] + E_{xc}[\rho_\alpha, \rho_\beta] \tag{2.21}
$$

with the Coulomb integral functional as

$$
J[\rho] = \frac{1}{2} \int \frac{\rho(\mathbf{r})\rho(\mathbf{r}')}{|\mathbf{r} - \mathbf{r}'|} d^3\mathbf{r} d^3\mathbf{r}' \tag{2.22}
$$

and the exchange-correlation functional $E_{xc}[\rho_\alpha, \rho_\beta]$ accounting for the energy amount to keep the exactness of the Hohenberg-Kohn formulation. The total energy functional for the true system is then given by the expression in Eq. 2.10.

Next, we target the minimization of the total energy functionals $E_s[\rho_\alpha, \rho_\beta]$ and $E[\rho_\alpha, \rho_\beta]$ of the two system in question. As a result of the spin-up and spin-down electron densities being constrained to integrate to N_α and N_β respectively, the task is suitably solved by the method of Lagrange multipliers. Thus, we define the associated Lagrange functionals as

$$\begin{cases} L_s[\rho_\alpha,\rho_\beta] = E_s[\rho_\alpha,\rho_\beta] - \mu_\alpha\left[\int \rho_\alpha(\mathbf{r})d^3\mathbf{r} - N_\alpha\right] - \mu_\beta\left[\int \rho_\beta(\mathbf{r})d^3\mathbf{r} - N_\beta\right] \\ L[\rho_\alpha,\rho_\beta] = E[\rho_\alpha,\rho_\beta] - \mu_\alpha\left[\int \rho_\alpha(\mathbf{r})d^3\mathbf{r} - N_\alpha\right] - \mu_\beta\left[\int \rho_\beta(\mathbf{r})d^3\mathbf{r} - N_\beta\right] \end{cases} \tag{2.23}$$

and proceed with their minimization by imposing

$$\begin{cases} \frac{\delta L_s}{\delta\rho_\gamma}[\rho_\alpha,\rho_\beta] = 0 \\ \frac{\delta L}{\delta\rho_\gamma}[\rho_\alpha,\rho_\beta] = 0 \end{cases} \quad \text{with } \gamma = \alpha,\beta \tag{2.24}$$

which leads to

$$\begin{cases} \frac{\delta T_s}{\delta\rho_\gamma}[\rho_\alpha,\rho_\beta] + v_s^\gamma[\rho_\alpha,\rho_\beta](\mathbf{r}) - \mu_\gamma = 0 \\ \frac{\delta T_s}{\delta\rho_\gamma}[\rho_\alpha,\rho_\beta] + v_{ext}[\rho_\alpha,\rho_\beta](\mathbf{r}) + v_{coul}[\rho](\mathbf{r}) + v_{xc}^\gamma[\rho_\alpha,\rho_\beta](\mathbf{r}) - \mu_\gamma = 0 \end{cases} \quad \text{with } \gamma = \alpha,\beta \tag{2.25}$$

with the new potentials $v_{coul}[\rho] = \frac{\delta J}{\delta\rho}[\rho]$ and $v_{xc}^\gamma[\rho_\alpha,\rho_\beta] = \frac{\delta E_{xc}}{\delta\rho_\gamma}[\rho_\alpha,\rho_\beta]$.

So the only way these two minimization processes return the same ground-state electron densities ρ_α^0 and ρ_β^0 is to set the spin-dependent potentials $v_s^\alpha[\rho_\alpha,\rho_\beta]$ and $v_s^\beta[\rho_\alpha,\rho_\beta]$ for the reference system to

$$\begin{cases} v_{KS}^\alpha[\rho_\alpha,\rho_\beta](\mathbf{r}) = v_{ext}[\rho_\alpha,\rho_\beta](\mathbf{r}) + v_{coul}[\rho](\mathbf{r}) + v_{xc}^\alpha[\rho_\alpha,\rho_\beta](\mathbf{r}) \\ v_{KS}^\beta[\rho_\alpha,\rho_\beta](\mathbf{r}) = v_{ext}[\rho_\alpha,\rho_\beta](\mathbf{r}) + v_{coul}[\rho](\mathbf{r}) + v_{xc}^\beta[\rho_\alpha,\rho_\beta](\mathbf{r}) \end{cases} \tag{2.26}$$

that go under the name of spin-dependent Kohn-Sham potentials.

If we substitute them into the single-electron equations in Eq. 2.17, we end up with the so called Kohn-Sham equations

$$\left[-\frac{1}{2}\nabla_i^2 + v_{KS}^\gamma(\mathbf{r})\right]\phi_i^\gamma(\mathbf{r}) = \epsilon_i^\gamma\phi_i^\gamma(\mathbf{r}) \text{ with } \gamma = \alpha,\beta \tag{2.27}$$

that are solved for the single-electron energies $\{\epsilon_i^\alpha,\epsilon_i^\beta\}$ and orbitals $\{\phi_i^\alpha,\phi_i^\beta\}$.

These quantities are finally used to compute the ground-state electron densities

$$\rho_\alpha^0(\mathbf{r}) = \sum_{i=1}^{N_\alpha}|\phi_i^\alpha(\mathbf{r})|^2 \quad \text{and} \quad \rho_\beta^0(\mathbf{r}) = \sum_{i=1}^{N_\beta}|\phi_i^\beta(\mathbf{r})|^2 \tag{2.28}$$

and the associated total energy by substituting them into Eq. 2.10

$$E[\rho_\alpha^0,\rho_\beta^0] = \sum_{\gamma\in\{\alpha,\beta\}}\sum_{i=1}^{N_\gamma}\epsilon_i^\gamma + E_{xc}[\rho_\alpha^0,\rho_\beta^0] - \sum_{\gamma\in\{\alpha,\beta\}}\int v_{xc}^\gamma[\rho_\alpha^0,\rho_\beta^0](\mathbf{r})\rho_\gamma^0(\mathbf{r})d^3\mathbf{r} - 2J[\rho^0]. \tag{2.29}$$

It is worth to mention that the exact analytical expression for the exchange-correlation energy is actually unknown and thus it requires the development of approximations. The two most commonly chosen approaches are the LDA and the GGA. One relies on the assumption that the electron density of many materials presents a local homogeneous gas behaviour, the other instead is meant to improve the LDA accuracy by modeling the functional dependence on the density gradient.

2.2 Dudarev's approach to the Hubbard-U correction

The use of standard DFT calculations within LDA or GGA in the study of materials with ions containing partially-filled d or f shells (e.g. transition metal oxides) often predicts unphysical metallic ground-states, which in practice translates to non-vanishing conducibility due to the underestimation or even the absence of a gap between the valence and the conduction bands. On the side, the equilibrium lattice constants (binding energies) are also underestimated (overestimated).

Such a problem can be attributed to an inaccurate description of the strong Coulomb repulsion between localized d or f electrons. Indeed, if the effective on-site Coulomb repulsion at play is comparable with the valence bandwidth, the probability of electronic transfer between neighbouring sites becomes negligible, causing the system to undergo the so called Mott transition.

One of the easiest ways to compensate for the DFT limitations was proposed by Dudarev et al. in a paper [27] dating back to 1998. The starting point is a single-site Hamiltonian of the form

$$\hat{H}_U = \frac{\bar{U}}{2} \sum_{m,m',\sigma} \hat{n}_{m,\sigma}\hat{n}_{m',-\sigma} + \frac{\bar{U}-\bar{J}}{2} \sum_{\substack{m,m',\sigma \\ m\neq m'}} \hat{n}_{m,\sigma}\hat{n}_{m',\sigma} \tag{2.30}$$

where $\bar{U}$, $\bar{J}$ are the spherically-averaged matrix elements of the screened Coulomb electron-electron interaction and $\hat{n}_{m,\sigma}$ indicates the number operator for localized electrons with the orbital quantum number l (usually $l = 2$ or 3 for d or f cases), the orbital momentum projection m ranging from $-l$ to $+l$ by unit steps and the spin projection $\sigma = \pm\frac{1}{2}$.

For an integer number of localized electrons, the energy expectation value is given by

$$\langle N_\sigma|\hat{H}_U|N_\sigma\rangle = \frac{\bar{U}}{2} \sum_{\sigma} N_\sigma N_{-\sigma} + \frac{\bar{U}-\bar{J}}{2} \sum_{\sigma} N_\sigma(N_\sigma - 1) \tag{2.31}$$

with N_σ as the expectation value of the total number operator for spin-σ localized electrons, namely $\hat{N}_\sigma = \sum_m \hat{n}_{m,\sigma}$.

For a non-integer number of localized electrons instead, it can be approximated by the Unrestricted Hartree-Fock (UHF) formula

$$\langle N_\sigma|\hat{H}_U|N_\sigma\rangle_{UHF} = \frac{\bar{U}}{2}\sum_{m,m',\sigma} n_{m,\sigma}n_{m',-\sigma} + \frac{\bar{U}-\bar{J}}{2}\sum_{\substack{m,m',\sigma \\ m\neq m'}} n_{m,\sigma}n_{m',\sigma} \tag{2.32}$$

where the number operators $\{\hat{n}_{m,\sigma}\}$ have been substituted by the associated expectation values $\{n_{m,\sigma}\}$ accordingly.

Therefore, the DFT total energy functional is supplied by an additional correction that consists of the substraction between the two energy expectation values in Eqs. 2.31 and 2.32 as follows

$$\begin{aligned}
E_{DFT+U} &= E_{DFT} + [\langle N_\sigma|\hat{H}_U|N_\sigma\rangle_{UHF} - \langle N_\sigma|\hat{H}_U|N_\sigma\rangle] = \\
&= E_{DFT} + \frac{\bar{U}-\bar{J}}{2}\left[\sum_{\substack{m,m',\sigma \\ m\neq m'}} n_{m,\sigma}n_{m',\sigma} - \sum_\sigma N_\sigma(N_\sigma-1)\right] = \\
&= E_{DFT} + \frac{\bar{U}-\bar{J}}{2}\left[\sum_{\substack{m,m',\sigma \\ m\neq m'}} n_{m,\sigma}n_{m',\sigma} - \sum_{m,m',\sigma} n_{m,\sigma}n_{m',\sigma} + \sum_{m,\sigma} n_{m,\sigma}\right] = \\
&= E_{DFT} + \frac{\bar{U}-\bar{J}}{2}\sum_{m,\sigma}(n_{m,\sigma} - n_{m,\sigma}^2),
\end{aligned} \tag{2.33}$$

which is already quite a compact expression, but it can be further simplified by the construction of the so called on-site occupancy matrix $\tilde{n}_\sigma$. In fact, the latter one takes a diagonal form with eigenvalues $\{n_{m,\sigma}\}$ within the real spherical harmonics' representation of the orbital degrees of freedom, implying that the DFT+U functional becomes

$$E_{DFT+U} = E_{DFT} + \frac{\bar{U}-\bar{J}}{2}\sum_\sigma \mathrm{Tr}[\tilde{n}_\sigma - \tilde{n}_\sigma\tilde{n}_\sigma] \tag{2.34}$$

So the correction term proposed by Dudarev et al. can be interpreted as a penalty term which forces the on-site occupancy matrix $\tilde{n}_\sigma$ towards idempotency (i.e. $\tilde{n}_\sigma = \tilde{n}_\sigma\tilde{n}_\sigma$). As a consequence, its eigenvalues $\{n_{m,\sigma}\}$ will tend to either 0 or 1, avoiding any fractional occupation of the interested orbitals.

2.3 Constraining local magnetic moments

Non-collinear magnetic phases can be investigated within VASP framework by imposing constraints on the direction of the local atomic magnetic moments $\vec{M}_I$ in the physical system under study. This task is achieved by adding a penalty term E_p to the standard DFT total energy functional E_{DFT} with a set of Lagrange multipliers $\{\lambda_I\}$ [30].

An intuitive way to define the local magnetic moment reads as

$$\vec{M}_I = \int_{\Omega_I} \vec{m}(\mathbf{r}) d^3\mathbf{r} \tag{2.35}$$

with the Wigner-Seitz sphere Ω_I of radius $\mathbf{R}_I$ centered on the atomic site $\mathbf{r}_I$ and the magnetization density vector $\vec{m}(\mathbf{r}) = \frac{1}{2}[\rho_\alpha(\mathbf{r}) - \rho_\beta(\mathbf{r})]$, but in practical calculations it is actually modified to

$$\vec{M}_I^F = \int_{\Omega_I} \vec{m}(\mathbf{r}) F_I\left(\frac{\pi|\mathbf{r}-\mathbf{r}_I|}{|\mathbf{R}_I|}\right) d^3\mathbf{r}, \tag{2.36}$$

where $F_I(x) = \frac{\sin x}{x}$ decreases to zero towards the boundary of Ω_I.

As anticipated above, the minimization of the total energy functional is constrained to a specific magnetic configuration by an additional term, which opposes any tilting of the local magnetic moments from the chosen directions $\{\hat{e}_I\}$ assigning positive energy contributions as follows

$$\begin{aligned} E = E_{DFT} + E_p = E_{DFT} + \sum_I \lambda_I(|\vec{M}_I^F| - \hat{e}_I \cdot \vec{M}_I^F) = \\ = E_{DFT} + \sum_I \lambda_I |\vec{M}_I^F|(1 - \cos\theta_I) \end{aligned} \tag{2.37}$$

with θ_I being the angle between the current smoothly-integrated local magnetic moment $\vec{M}_I^F$ and the unit vector for the desired direction $\hat{e}_I$.

The main parameters at play here are the radii $\{\mathbf{R}_I\}$ of the Wigner-Seitz spheres and the Lagrange multipliers $\{\lambda_I\}$, which respectively affect the volume integration for the local magnetic moments and the energy scale of the penalty term. For an optimal choice of $\{\mathbf{R}_I\}$, one should just avoid any overlap between adjacent Wigner-Seitz spheres. For what concerns the values of $\{\lambda_I\}$ instead, a more accurate analysis on the convergence of the penalty energy is needed.

It all starts with the critical angles $\{\theta'_I\}$ that are obtained by solving the variational equations

$$\begin{aligned} \left.\frac{\delta E}{\delta \theta_I}\right|_{\theta_I=\theta'_I} &= \left.\frac{\delta E_{DFT}}{\delta \theta_I}\right|_{\theta_I=\theta'_I} + \lambda_I |\vec{M}_I^F| \sin\theta'_I = 0 \\ \Rightarrow\ \sin\theta'_I &= -\frac{1}{\lambda_I |\vec{M}_I^F|} \left.\frac{\delta E_{DFT}}{\delta \theta_I}\right|_{\theta_I=\theta'_I} . \end{aligned} \tag{2.38}$$

If the current magnetic configuration is a sufficiently good guess, one expects the solutions $\{\theta'_I\}$ to be small enough to apply first-order Taylor expansion to both sides, leading to

$$\begin{aligned} \theta'_I &\simeq -\frac{1}{\lambda_I |\vec{M}_I^F|} \left(\left.\frac{\delta E_{DFT}}{\delta \theta'_I}\right|_{\theta'_I=0} + \left.\frac{\delta^2 E_{DFT}}{\delta {\theta'_I}^2}\right|_{\theta'_I=0} \theta'_I \right) \\ \Rightarrow\ \theta'_I &\simeq -\frac{K_1}{\lambda_I |\vec{M}_I^F| + K_2} \end{aligned} \tag{2.39}$$

with the coefficients $K_1 = \left.\frac{\delta E_{DFT}}{\delta \theta'_I}\right|_{\theta'_I=0}$ and $K_2 = \left.\frac{\delta^2 E_{DFT}}{\delta {\theta'_I}^2}\right|_{\theta'_I=0}$.

As a result, the penalty energy close to the minimum behaves as follows

$$E_p \simeq \sum_I \lambda_I |\vec{M}_I^F| \frac{{\theta'_I}^2}{2} \simeq \frac{1}{2} \sum_I \lambda_I |\vec{M}_I^F| \left(\frac{K_1}{\lambda_I |\vec{M}_I^F| + K_2} \right)^2 \tag{2.40}$$

implying that $E_p \sim \lambda_I^{-1}$ for large λ_I. Then, for very accurate total energy calculations it is often suggested to perform convergence tests of E_p against λ_I or eventually restart the electronic self-consistent cycles with increasing values of λ_I.

2.4 Four-states energy-mapping method

The four-states methodology was firstly introduced by H. J. Xiang et al. in the papers [31, 32] as an extension of the usual energy-mapping methods based on DFT electronic structure calculations for the determination of both isotropic and anisotropic exchange couplings. However, the actual derivation of the main equations without any assumptions on the shape of the resulting interaction tensors was only presented in [33], which is indeed the reference to this section.

The most convenient way to model quadratic spin-spin interactions for a magnetic system is to introduce the so called generalized Heisenberg Hamiltonian

$$\hat{H}_I = \hat{H}_{IEI} + \hat{H}_{SIA} = \sum_{\substack{ij,\alpha\beta \\ i<j}} \hat{S}_\alpha^{(i)} J_{\alpha\beta}^{(ij)} \hat{S}_\beta^{(j)} + \sum_{i,\alpha\beta} \hat{S}_\alpha^{(i)} A_{\alpha\beta}^{(i)} \hat{S}_\beta^{(i)} \tag{2.41}$$

where $\hat{S}_{\alpha}^{(i)}$ stands for the α-th component of the spin vector operator of the i-th magnetic site, while $J_{\alpha\beta}^{(ij)}$ and $A_{\alpha\beta}^{(i)}$ represent the (α,β)-th matrix element of the IEI tensor for the spin pair (ij) and the SIA tensor for the i-th spin respectively.

First, we focus on the procedure for the determination of an arbitrarily chosen exchange coupling $J_{\alpha^*\beta^*}^{(i^*j^*)}$, which is based on rewriting the two terms in Eq. 2.41 as

$$\begin{aligned}\hat{H}_{IEI} = &\sum_{\alpha\beta} \hat{S}_{\alpha}^{(i^*)} J_{\alpha\beta}^{(i^*j^*)} \hat{S}_{\beta}^{(j^*)} + \sum_{j\neq j^*} \sum_{\alpha\beta} \hat{S}_{\alpha}^{(i^*)} J_{\alpha\beta}^{(i^*j)} \hat{S}_{\beta}^{(j)} + \sum_{i\neq i^*} \sum_{\alpha\beta} \hat{S}_{\alpha}^{(i)} J_{\alpha\beta}^{(ij^*)} \hat{S}_{\beta}^{(j^*)} + \\ &+ \sum_{\substack{i\neq i^* \\ j\neq j^*}} \sum_{\alpha\beta} \hat{S}_{\alpha}^{(i)} J_{\alpha\beta}^{(ij)} \hat{S}_{\beta}^{(j)}\end{aligned} \tag{2.42}$$

$$\hat{H}_{SIA} = \sum_{\alpha\beta} \hat{S}_{\alpha}^{(i^*)} A_{\alpha\beta}^{(i^*)} \hat{S}_{\beta}^{(i^*)} + \sum_{\alpha\beta} \hat{S}_{\alpha}^{(j^*)} A_{\alpha\beta}^{(j^*)} \hat{S}_{\beta}^{(j^*)} + \sum_{i\neq i^*j^*} \sum_{\alpha\beta} \hat{S}_{\alpha}^{(i)} A_{\alpha\beta}^{(i)} \hat{S}_{\beta}^{(i)} \tag{2.43}$$

in order to separate out all the contributions involving at least one of the components of the spin operators under consideration, namely $\hat{S}^{(i^*)}$ and $\hat{S}^{(j^*)}$.

Next, the $J_{\alpha^*\beta^*}^{(i^*j^*)}$ coupling can be isolated by computing the energies $\{E_1, E_2, E_3, E_4\}$ of four distinct magnetic states $\{\Lambda_1, \Lambda_2, \Lambda_3, \Lambda_4\}$, which differ by the direction of the spin expectation values $\{\vec{S}^{(i)} = \langle \hat{S}^{(i)} \rangle\}$ at each site as follows

$$\begin{aligned}
\Lambda_1 &: \vec{S}^{(i^*)} = +S\hat{e}_{\alpha^*},\ \vec{S}^{(j^*)} = +S\hat{e}_{\beta^*} \text{ and } \vec{S}^{(k\neq i^*j^*)} = \pm S\hat{e}_{\gamma\neq\alpha^*,\beta^*} \\
\Lambda_2 &: \vec{S}^{(i^*)} = +S\hat{e}_{\alpha^*},\ \vec{S}^{(j^*)} = -S\hat{e}_{\beta^*} \text{ and } \vec{S}^{(k\neq i^*j^*)} = \pm S\hat{e}_{\gamma\neq\alpha^*,\beta^*} \\
\Lambda_3 &: \vec{S}^{(i^*)} = -S\hat{e}_{\alpha^*},\ \vec{S}^{(j^*)} = +S\hat{e}_{\beta^*} \text{ and } \vec{S}^{(k\neq i^*j^*)} = \pm S\hat{e}_{\gamma\neq\alpha^*,\beta^*} \\
\Lambda_4 &: \vec{S}^{(i^*)} = -S\hat{e}_{\alpha^*},\ \vec{S}^{(j^*)} = -S\hat{e}_{\beta^*} \text{ and } \vec{S}^{(k\neq i^*j^*)} = \pm S\hat{e}_{\gamma\neq\alpha^*,\beta^*}
\end{aligned} \tag{2.44}$$

with $\{\hat{e}_x, \hat{e}_y, \hat{e}_z\}$ as the set of unit vectors for the Cartesian axes of the global reference frame. The basic idea behind such non-trivial configurations is to direct the interested spins $\hat{S}^{(i^*)}$ and $\hat{S}^{(j^*)}$ respectively along $\hat{e}_{\alpha*}$ and $\hat{e}_{\beta*}$ towards the positive or negative sides alternating parallel and antiparallel setups. All the other spins $\vec{S}^{(k\neq i^*j^*)}$ are instead perpendicular to $\hat{S}^{(i^*)}$ and $\hat{S}^{(j^*)}$ without any specific requirement about the sign factor.

The associated energies can be thus obtained by substituting the spin operators in Eqs. 2.42 and 2.43 with the vectors in Eq. 2.44

$$
\begin{aligned}
E_1 =& + J^{(i^*j^*)}_{\alpha^*\beta^*} S^2 + \sum_{k\neq j^*} J^{(i^*k)}_{\alpha^*\gamma} S^2 + \sum_{k\neq i^*} J^{(kj^*)}_{\gamma\beta^*} S^2 + \sum_{\substack{k\neq i^*\\ k'\neq j^*}} J^{(kk')}_{\gamma\gamma} S^2 + \\
&+ A^{(i^*)}_{\alpha^*\alpha^*} S^2 + A^{(j^*)}_{\beta^*\beta^*} S^2 + \sum_{k\neq i^*j^*} A^{(k)}_{\gamma\gamma} S^2 \\
E_2 =& - J^{(i^*j^*)}_{\alpha^*\beta^*} S^2 + \sum_{k\neq j^*} J^{(i^*k)}_{\alpha^*\gamma} S^2 - \sum_{k\neq i^*} J^{(kj^*)}_{\gamma\beta^*} S^2 + \sum_{\substack{k\neq i^*\\ k'\neq j^*}} J^{(kk')}_{\gamma\gamma} S^2 + \\
&+ A^{(i^*)}_{\alpha^*\alpha^*} S^2 + A^{(j^*)}_{\beta^*\beta^*} S^2 + \sum_{k\neq i^*j^*} A^{(k)}_{\gamma\gamma} S^2 \\
E_3 =& - J^{(i^*j^*)}_{\alpha^*\beta^*} S^2 - \sum_{k\neq j^*} J^{(i^*k)}_{\alpha^*\gamma} S^2 + \sum_{k\neq i^*} J^{(kj^*)}_{\gamma\beta^*} S^2 + \sum_{\substack{k\neq i^*\\ k'\neq j^*}} J^{(kk')}_{\gamma\gamma} S^2 + \\
&+ A^{(i^*)}_{\alpha^*\alpha^*} S^2 + A^{(j^*)}_{\beta^*\beta^*} S^2 + \sum_{k\neq i^*j^*} A^{(k)}_{\gamma\gamma} S^2 \\
E_4 =& + J^{(i^*j^*)}_{\alpha^*\beta^*} S^2 - \sum_{k\neq j^*} J^{(i^*k)}_{\alpha^*\gamma} S^2 - \sum_{k\neq i^*} J^{(kj^*)}_{\gamma\beta^*} S^2 + \sum_{\substack{k\neq i^*\\ k'\neq j^*}} J^{(kk')}_{\gamma\gamma} S^2 + \\
&+ A^{(i^*)}_{\alpha^*\alpha^*} S^2 + A^{(j^*)}_{\beta^*\beta^*} S^2 + \sum_{k\neq i^*j^*} A^{(k)}_{\gamma\gamma} S^2,
\end{aligned}
\tag{2.45}
$$

finally implying that the target coupling constant reads as

$$
J^{(i^*j^*)}_{\alpha^*\beta^*} = \frac{1}{4S^2}(E_1 + E_4 - E_2 - E_3). \tag{2.46}
$$

A similar procedure also provides the matrix elements for the SIA tensor, which indeed has to be symmetric (i.e. $A^{(i)}_{\alpha\beta} = A^{(i)}_{\beta\alpha}\ \forall i, \alpha, \beta$) due to the fact that the spin components involved in the associated interaction terms are always referred to a single site. The latter property reduces its inequivalent coupling constants to 6: namely, 3 along the diagonal and other 3 above (or below) the diagonal. Moreover, since $(\hat{S}^{(i)}_x)^2 = (\hat{S}^{(i)})^2 - (\hat{S}^{(i)}_y)^2 - (\hat{S}^{(i)}_z)^2$, the diagonal part of the SIA Hamiltonian becomes

$$
\begin{aligned}
\hat{H}^{diag}_{SIA} &= \sum_i [A^{(i)}_{xx}(\hat{S}^{(i)}_x)^2 + A^{(i)}_{yy}(\hat{S}^{(i)}_y)^2 + A^{(i)}_{zz}(\hat{S}^{(i)}_z)^2] = \\
&= \sum_i A^{(i)}_{xx}(\hat{S}^{(i)})^2 + \sum_i \sum_{\alpha\in\{y,z\}} (A^{(i)}_{\alpha\alpha} - A^{(i)}_{xx})(\hat{S}^{(i)}_\alpha)^2
\end{aligned}
\tag{2.47}
$$

where the first term acts as a mere additive constant and also the relevant target quantities shrink to $(A^{(i)}_{yy} - A^{(i)}_{xx})$ and $(A^{(i)}_{zz} - A^{(i)}_{xx})$.

As anticipated above, the determination of these parameters $\{A^{(i^*)}_{\alpha^*\alpha^*} - A^{(i^*)}_{xx}\}$ reminds the previous treatment for $\{J^{(i^*j^*)}_{\alpha^*\beta^*}\}$. The main difference regards the definition of the four distinct magnetic states

$$\begin{aligned}
\Lambda_1 &: \vec{S}^{(i^*)} = +S\hat{e}_{\alpha^*} \text{ and } \vec{S}^{(k\neq i^*j^*)} = \pm S\hat{e}_{\gamma\neq\alpha^*,x} \\
\Lambda_2 &: \vec{S}^{(i^*)} = -S\hat{e}_{\alpha^*} \text{ and } \vec{S}^{(k\neq i^*j^*)} = \pm S\hat{e}_{\gamma\neq\alpha^*,x} \\
\Lambda_3 &: \vec{S}^{(i^*)} = +S\hat{e}_{x} \text{ and } \vec{S}^{(k\neq i^*j^*)} = \pm S\hat{e}_{\gamma\neq\alpha^*,x} \\
\Lambda_4 &: \vec{S}^{(i^*)} = -S\hat{e}_{x} \text{ and } \vec{S}^{(k\neq i^*j^*)} = \pm S\hat{e}_{\gamma\neq\alpha^*,x},
\end{aligned} \tag{2.48}$$

which are thus associated with the energies

$$\begin{aligned}
E_1 &= +\sum_k J^{(i^*k)}_{\alpha^*\gamma} S^2 + \sum_{\substack{k\neq i^* \\ k'>k}} J^{(kk')}_{\gamma\gamma} S^2 + A^{(i^*)}_{\alpha^*\alpha^*} S^2 + \sum_{k\neq i^*} A^{(k)}_{\gamma\gamma} S^2 \\
E_2 &= -\sum_k J^{(i^*k)}_{\alpha^*\gamma} S^2 + \sum_{\substack{k\neq i^* \\ k'>k}} J^{(kk')}_{\gamma\gamma} S^2 + A^{(i^*)}_{\alpha^*\alpha^*} S^2 + \sum_{k\neq i^*} A^{(k)}_{\gamma\gamma} S^2 \\
E_3 &= +\sum_k J^{(i^*k)}_{x\gamma} S^2 + \sum_{\substack{k\neq i^* \\ k'>k}} J^{(kk')}_{\gamma\gamma} S^2 + A^{(i^*)}_{xx} S^2 + \sum_{k\neq i^*} A^{(k)}_{\gamma\gamma} S^2 \\
E_4 &= -\sum_k J^{(i^*k)}_{x\gamma} S^2 + \sum_{\substack{k\neq i^* \\ k'>k}} J^{(kk')}_{\gamma\gamma} S^2 + A^{(i^*)}_{xx} S^2 + \sum_{k\neq i^*} A^{(k)}_{\gamma\gamma} S^2.
\end{aligned} \tag{2.49}$$

So the summation of energies needed to extract the sought-for parameter is

$$A^{(i^*)}_{\alpha^*\alpha^*} - A^{(i^*)}_{xx} = \frac{1}{2S^2}(E_1 + E_2 - E_3 - E_4) \tag{2.50}$$

and it slightly differs from the previous Eq. 2.46.

Further details on the three inequivalent off-diagonal elements of the SIA tensor and some related symmetry considerations can be found in Ref. [33].

2.5 Magnetic force theorem within Hubbard-I approximation

All the theoretical aspects about the here presented method are deeply described in Ref. [34] and most of the computational details concerning its implementation can be found in Ref. [35].

To summarize, the approach in question allows an in-depth characterization of both the electronic structure and the magnetic interactions of strongly correlated materials

at the quasi-atomic limit, combining self-consistent DFT cycles with DMFT calculations within the so called HI approximation. This merged theoretical framework will be indicated as DFT+DMFT(HI) from here on out.

The standard procedure includes a preliminary DFT cycle for the paramagnetic phase using the LDA exchange-correlation functional. The latter is indeed better suited to the double-counting correction that must be introduced with the on-site Coulomb repulsion at the DMFT level. Moreover, the relativistic SOC effect is also taken into account.

In the meantime, we identify the energy window W that contains the localized states to be projected onto the Wannier-like basis by plotting the partial Density of States (pDOS) at the DFT level. Ideally, the correlated bands should exhibit sharp peaks with a negligible hybridization, otherwise a larger energy window should be taken. This would imply a significant increase in the computational effort to achieve energy convergence or even the loss of quasi-exactness for reasons that will be shortly detailed.

Once the DFT convergence criterion is met, the LDA+DMFT(HI) cycle can be finally initialized. First of all, the wannierization of the selected localized states is addressed by defining the matrix elements of the Wannier projectors $\hat{P}^{\alpha,\sigma}_{l,m}$ in k-space representation as

$$P^{j\sigma}_{l\nu}(\mathbf{k}) = \langle \chi^{j\sigma}_{l} | \psi^{\sigma}_{\mathbf{k}\nu} \rangle \tag{2.51}$$

where $|\chi^{j\sigma}_{l}\rangle$ and $|\psi^{\sigma}_{\mathbf{k}\nu}\rangle$ respectively stand for the Wannier-like function of the orbital l centered at the atom j and the DFT Bloch state with band index ν evaluated at the wave vector $\mathbf{k}$ within the first Brillouin zone (1°BZ). σ simply specifies the spin component.

Afterwards, the on-site Coulomb interaction term is introduced. The most general expression within second quantization formalism reads as

$$\hat{H}_U = \sum_j \hat{H}^{(j)}_U = \sum_{jlmno\sigma\sigma'} U_{lmno} \hat{c}^{\dagger\sigma}_{jl} \hat{c}^{\dagger\sigma'}_{jm} \hat{c}^{\sigma'}_{jn} \hat{c}^{\sigma}_{jo} \tag{2.52}$$

with $\hat{c}^{\dagger\sigma}_{jl}$ ($\hat{c}^{\sigma}_{jl}$) being the creation (annihilation) operator for an electron with orbital configuration l, spin component σ and localized at the atomic site j.

However, it is needlessly complicated to treat computationally; so the following parametrization fits better

$$\begin{aligned} \hat{H}_U = U \sum_{jl\sigma} \hat{n}^{\sigma}_{jl} \hat{n}^{-\sigma}_{jl} + \sum_{\substack{jlm\sigma\sigma' \\ l\neq m}} (V - \delta_{\sigma\sigma'} J_H) \hat{n}^{\sigma}_{jl} \hat{n}^{\sigma'}_{jm} - \frac{J_H}{2} \sum_{\substack{jlm\sigma \\ l\neq m}} \hat{c}^{\dagger\sigma}_{jl} \hat{c}^{-\sigma}_{jl} \hat{c}^{\dagger-\sigma}_{jm} \hat{c}^{\sigma}_{jm} + \\ - \frac{\tilde{J}}{2} \sum_{\substack{jlm\sigma \\ l\neq m}} \hat{c}^{\dagger\sigma}_{jl} \hat{c}^{\dagger-\sigma}_{jl} \hat{c}^{\sigma}_{jm} \hat{c}^{-\sigma}_{jm} - \sum_{jl\sigma} \Delta\epsilon \hat{n}^{\sigma}_{jl} \end{aligned} \tag{2.53}$$

with the number operator $\hat{n}^{\sigma}_{jl} = \hat{c}^{\dagger\sigma}_{jl} \hat{c}^{\sigma}_{jl}$, the intra-orbital Coulomb repulsion U, the inter-orbital Coulomb repulsion $V(= U - 2J_H)$, the Hund exchange J_H, the pair-hopping

parameter $\tilde{J}(= J_H)$ and the double-counting correction $\Delta\epsilon = U(n_d - \frac{1}{2}) - J_H(\frac{n_d}{2} - \frac{1}{2})$.

Such an interacting many-body Hamiltonian can be solved by DMFT, which is based on mapping the true lattice problem into an effective periodic Anderson Impurity Model (AIM) for each inequivalent correlated site. The single-site AIM Hamiltonian takes the form

$$\begin{aligned}\hat{H}^{(j)}_{AIM} = &\sum_{\mathbf{k}l\sigma} \epsilon_l(\mathbf{k}) \hat{a}^{\dagger\sigma}_{\mathbf{k}l} \hat{a}^{\sigma}_{\mathbf{k}l} + \sum_{\mathbf{k}lm\sigma} [V_{lm}(\mathbf{k}) \hat{a}^{\dagger\sigma}_{\mathbf{k}l} \hat{c}^{\sigma}_{jm} + \text{h.c.}] + \\ &+ \sum_{m\sigma} \epsilon_0 \hat{c}^{\dagger\sigma}_{im} \hat{c}^{\sigma}_{jm} + \hat{H}^{(j)}_U\end{aligned} \tag{2.54}$$

and consists of four parts. The first and third terms represent the kinetic energy for the conduction electrons in the bath and the impurity electron respectively. Indeed, $\hat{a}^{\dagger\sigma}_{\mathbf{k}l}$ ($\hat{a}^{\sigma}_{\mathbf{k}l}$) stands for the creation (annihilation) operator for a conduction electron with band index l and spin component σ at wavevector $\mathbf{k}$, while $\hat{c}^{\dagger\sigma}_{im}$ ($\hat{c}^{\sigma}_{jm}$) is now interpreted as the creation (annihilation) operator for an impurity electron with orbital configuration m and spin component σ localized at site j. The second term instead provides the hybridization effects, which originates from the chance of an impurity electron to hop into the conduction bath or viceversa. Moreover, $\epsilon_l(\mathbf{k})$ and $V_{lm}(\mathbf{k})$ indicate respectively the l-th band dispersion relation for a conduction electron and the so called hybridization potential energy.

As for the effective Weiss model of ferromagnetism, the DMFT mapping is ensured by a self-consistency condition. In this case it requires that the interacting Green's functions (GF) of the two models, as well as the associated self-energies, coincide with each other.

This is encoded by

$$\begin{aligned}G_{loc}(i\omega_n) &= G_{imp}(i\omega_n) \\ \Sigma_{loc}(i\omega_n) &= \Sigma_{imp}(i\omega_n),\end{aligned} \tag{2.55}$$

where G_{loc} and Σ_{loc} (G_{imp} and Σ_{imp}) are the $\mathbf{k}$-integrated local interacting GF and the $\mathbf{k}$-independent self-energy for the lattice many-body (periodic Anderson impurity) model, while $\omega_n = \frac{\pi}{\beta}(2n-1)$ is the fermionic Matsubara frequency with $\beta = (k_B T)^{-1}$.

The control variable is the so called Weiss field $\mathcal{G}_0$, namely the non-interacting GF of the impurity model, that is given by the matrix elements

$$[\mathcal{G}_0^{-1}(i\omega_n)]^{\sigma}_{lm} = (i\omega_n - \mu - \Sigma_{dc})\delta_{lm} + \sum_{\substack{\mathbf{k}\in 1BZ \\ \nu\nu'}} P^{j\sigma}_{l\nu}(\mathbf{k}) E^{\mathbf{k}\sigma}_{LDA,\nu\nu'} P^{\dagger j\sigma}_{m\nu'}(\mathbf{k}) \tag{2.56}$$

within the spin-orbital degrees of freedom of the correlated space. In particular, μ, Σ_{dc} and $E^{\mathbf{k}\sigma}_{LDA,\nu\nu'} = \langle \psi^{\sigma}_{\mathbf{k}\nu} | \hat{H}^{\mathbf{k}\sigma}_{LDA} | \psi^{\sigma}_{\mathbf{k}\nu} \rangle$ respectively symbolize the chemical potential, the double-counting contribution to self-energy and the matrix elements for the LDA Hamiltonian in k-space representation $\hat{H}^{\mathbf{k}\sigma}_{LDA}$ within the Kohn-Sham bands' space.

However, the relation in Eq. 2.54 is only valid when the HI approximation is taken, meaning that the hybridization effects are assumed to be negligible. Otherwise, the complete version of Eq. 2.54 would also include a further additional term $\Delta(i\omega_n)$.

Another interesting consequence of HI approximation involves the AIM Hamiltonian in Eq. 2.52, which reduces to an atomic Hamiltonian of the form

$$\hat{H}_{at}^{(j)} = \sum_{lm\sigma} \epsilon_{lm} \hat{c}_{jl}^{\dagger\sigma} \hat{c}_{jm}^{\sigma} + \hat{H}_U^{(j)} \tag{2.57}$$

with $\{\epsilon_{lm}\}$ as the orbital-resolved single-electron energies. Such an operator can be diagonalized numerically to find its eigenvectors $|\gamma\rangle$ ($|\gamma'\rangle$) and energy eigenvalues E_γ ($E_{\gamma'}$) if the total number of localized electrons per correlated site is n_d ($n_d + 1$). They allow to determine the matrix elements of the atomic (i.e. impurity) interacting GF as

$$[G_{at}(i\omega_n)]_{lm}^{\sigma} = \sum_{\gamma\gamma'} \frac{\langle\gamma|\hat{c}_{jl}^{\sigma}|\gamma'\rangle\langle\gamma'|\hat{c}_{jm}^{\dagger\sigma}|\gamma\rangle}{i\omega_n + \mu + E_\gamma - E_{\gamma'}} \left[X_{\gamma'}^{(n_d+1)} - X_{\gamma}^{(n_d)}\right] \tag{2.58}$$

where $X_\gamma^{(n_d)} = \frac{1}{Z^{(n_d)}} e^{-\beta[E_\gamma - \mu(n_d)]}$ and $Z^{(n_d)}$ are the Boltzmann weight and the n_d-particle canonical partition function respectively.

The atomic self-energy is finally computed by inverting the **k**-integrated Dyson equation as follows

$$\Sigma_{at}(i\omega_n) = \mathcal{G}_0^{-1}(i\omega_n) - G_{at}^{-1}(i\omega_n). \tag{2.59}$$

This can be used to obtain a new trial charge density, which is then passed as input to the next LDA+DMFT(HI) iteration unless a target quantity (e.g. the atomic self-energy, the DFT total energy or the charge density) converges.

Once the final atomic self-energy is found, the focus shifts on the IEI tensors as they were the target quantities from the beginning. The magnetic force theorem within HI approximation comes at play now, as it allows to determine them by considering two-site fluctuations of the J-multiplet density matrix ρ. In particular, the effective low-energy Hamiltonian within the multipolar formalism takes the general form

$$\hat{H}_{IEI} = \sum_{\substack{ij \\ KK'QQ'}} V_{KK'}^{QQ'}(i,j) \hat{O}_K^Q(i) \hat{O}_{K'}^{Q'}(j) \tag{2.60}$$

with $V_{KK'}^{QQ'}(i,j)$ and $\hat{O}_K^Q(i)$ being the IEI tensor between the two correlated sites (i,j) and the multipolar operator of rank $K \in \{0, 1, ..., 2J\}$ and projection $Q \in \{-K, -K+1, ..., K-1, K\}$ defined within the J-multiplet ground state. The analytical expression for the IEI tensors derived by the FT-HI method reads as

$$V_{KK'}^{QQ'}(i,j) = \sum_{1234} \langle 13|V(i,j)|24\rangle \left[\hat{O}_K^Q(i)\right]_{21} \left[\hat{O}_{K'}^{Q'}(j)\right]_{43} \tag{2.61}$$

where $|1\rangle = |J, M_1\rangle$ is one of J-multiplet basis states, $\left[\hat{O}_K^Q(i)\right]_{21} = \langle 2|\hat{O}_K^Q(i)|1\rangle$ is a generic matrix element of the multipolar operator and

$$\langle 13|V(i,j)|24\rangle = \frac{1}{\beta}\mathrm{Tr}\left[G_{ij}\frac{\delta\Sigma_{at}}{\delta\rho_{34}}(i)G_{ji}\frac{\delta\Sigma_{at}}{\delta\rho_{12}}(j)\right]. \tag{2.62}$$

This last equation requires the knowledge of a formula for the intersite GF G_{ij}. Its matrix elements are given by

$$\begin{aligned}[G_{ij}(i\omega_n)]^{\sigma}_{lm} = \sum_{\substack{\mathbf{k}\in 1BZ \\ \nu\nu'}} e^{-i\mathbf{k}\cdot(\mathbf{R}_j-\mathbf{R}_i)}P^{i\sigma}_{l\nu}(\mathbf{k})\cdot \\ \cdot\left[(i\omega_n+\mu) - E^{\mathbf{k}\sigma}_{LDA,\nu\nu'} - P^{\dagger j\sigma}_{m\nu}(\mathbf{k})\Delta\Sigma P^{j\sigma}_{m\nu'}(\mathbf{k})\right]P^{\dagger i\sigma}_{l\nu'}(\mathbf{k})\end{aligned} \tag{2.63}$$

and for the derivative of atomic self-energy over a fluctuation of the density matrix element (i.e. $\delta\rho_{12}$) at site j

$$\frac{\delta\Sigma_{at}}{\delta\rho_{12}}(j) = G^{-1}_{at}(j)\left([G_{at}]_{12} - \frac{\mathrm{Tr}[G_{at}]}{n_d}\delta_{12}\right)G^{-1}_{at}(j). \tag{2.64}$$

2.6 Monte Carlo simulations

The Monte Carlo method is a powerful computational technique that expoits the generation of pseudo-random numbers to simulate the behaviour of a large variety of systems and thus finds interesting applications in physics and many other areas of knowledge.

In particular, the here presented simulations are carried out using the UppASD package [36–39], which not only focuses on the numerical solution of the Landau-Lifshitz-Gilbert (LLG) equations of motion for atomic magnetic moments in a solid, but also provides an efficient implementation of MC algorithms to study interacting spin systems at finite temperatures.

Among the available options we choose the Metropolis algorithm [40], which allows to explore the phase space of magnetic configurations by applying a precise set of steps. First of all, the atomic magnetic moments are aligned to the input directions defining the initial phase Ξ_0 and the associated energy is given by

$$E(\Xi) = -\frac{1}{2}\sum_{\substack{ij,\alpha\beta \\ i\neq j}} m^{(i)}_{\alpha}J^{(ij)}_{\alpha\beta}m^{(j)}_{\beta} - \sum_i (A^{(i)}_{zz} - A^{(i)}_{xx})(m^{(i)}_z)^2, \tag{2.65}$$

including both IEI and SIA coupling terms. Then, we build a new candidate configuration Ξ_1 by randomly flipping some of the magnetic moments. If that is energetically favoured (i.e. $\Delta E = E(\Xi_1) - E(\Xi_0) < 0$), Ξ_1 will be straightforwardly accepted as a new point in the overall trajectory of the system within the magnetic phase space. Otherwise, we

shall set an acceptance probability $P_{acc} = e^{-\beta \Delta E} < 1$ with $\beta = (k_B T)^{-1}$. Indeed, as these last two steps of proposal and eventually acceptance are iterated, the system will unavoidably tend to lower and lower energy phases.

However, since the initial configuration is most likely not close enough to thermal equilibrium, it is common practice to start collecting data only after a quite large number N_{init} of preliminary MC iterations.

So once this thermalization process is concluded, we proceed with the calculation of the thermodynamical properties of interest. For instance, the instantaneous average magnetization at a generic MC iteration k is given by

$$\langle \vec{M}_k \rangle = \frac{1}{N} \sum_{i=1}^{N} \vec{m}^{(i)} \quad \text{with } \vec{m}^{(i)} \in \Xi_{N_{init}+k} \tag{2.66}$$

which contributes to the cumulated magnetization as

$$\langle \vec{M} \rangle_{cum} = \frac{1}{k} \sum_{k'=N_{init}+1}^{N_{init}+k} \langle \vec{M}_{k'} \rangle \tag{2.67}$$

Similarly, we can also estimate the magnetic specific heat

$$C_{mag} = \frac{\partial E}{\partial T} = \frac{\langle E_k^2 \rangle_{cum} - \langle E_k \rangle_{cum}^2}{k_B T} \tag{2.68}$$

and the magnetic susceptibility

$$X = \frac{\partial M}{\partial T} = \frac{\langle M_k^2 \rangle_{cum} - \langle M_k \rangle_{cum}^2}{k_B T}, \tag{2.69}$$

since they are good candidates to mark the typical fluctuations that emerge close to magnetic phase transitions. A common approach to stabilize these effects is to initialize more than a single replica of the spin system under study and let them evolve according to instructions of the Metropolis algorithm independently. This will add more statistics for the evaluation of the observables, leading to more stable results. Finally, we can also minimize the effects of autocorrelation between consecutive averages by storing data at regular intervals, rather than for all accepted magnetic configurations.

Chapter 3

Chromium trihalides

This chapter outlines the current state of knowledge regarding the fundamental properties of chromium trihalides within the scientific community from a predominantly experimental perspective.
The growing interest in these compounds derives from their peculiar van der Waals layered magnetic structure, which makes them suitable for the exfoliation into ultra-thin films. This feature is of significant relevance in the field of next-generation spintronics, where low-dimensionality finds numerous applications. However, the effect of quantum confinement on their electronic, optical and magnetic properties is still widely debated both in theoretical and experimental collectives.
Here we focus on a specific series of chromium trihalides, namely CrX_3 with X = Cl, Br, I, where the ligand atom X is substituted by one of the listed halogens with increasing atomic number Z = 17, 35, 53 in order from left to right.

3.1 Crystal structure

The X-ray diffraction (XRD) measurements reported in [41–43] show that chromium trihalides at the bulk limit crystallize into a rhombohedral phase at low temperatures and also undergo a structural transition to a less symmetrical monoclinic one at about 240, 374 and 210 K respectively for $CrCl_3$, $CrBr_3$ and CrI_3.

For instance, both the phases feature a van der Waals (vdW) layered structure, where the Cr atoms at each layer arrange in a honeycomb net with an edge-sharing octahedral coordination due to the surrounding ligand atoms.

However, they differ by three main aspects: the stacking geometry, the interlayer distance and the in-plane symmetry. Indeed, adjacent layers in the rhombohedral phase are displaced upon stacking by the shift vector $\vec{s} = \vec{a} + \vec{b}$ with $\vec{a}$ and $\vec{b}$ being the in-

plane lattice vectors, while for the monoclinic phase the shift vector becomes $\vec{s} \simeq \frac{1}{4}\vec{a}$. This results in an ideal (approximate) ABC stacking pattern for the first (second) case. Moreover, when passing from low to high temperatures, not only the interlayer distance turns out to decrease by almost 5%, but also the in-plane symmetry is slightly broken. As a matter of fact, the bond lengths and the characteristic angles split up into two groups, implying non-negligible distortions to the octahedra.

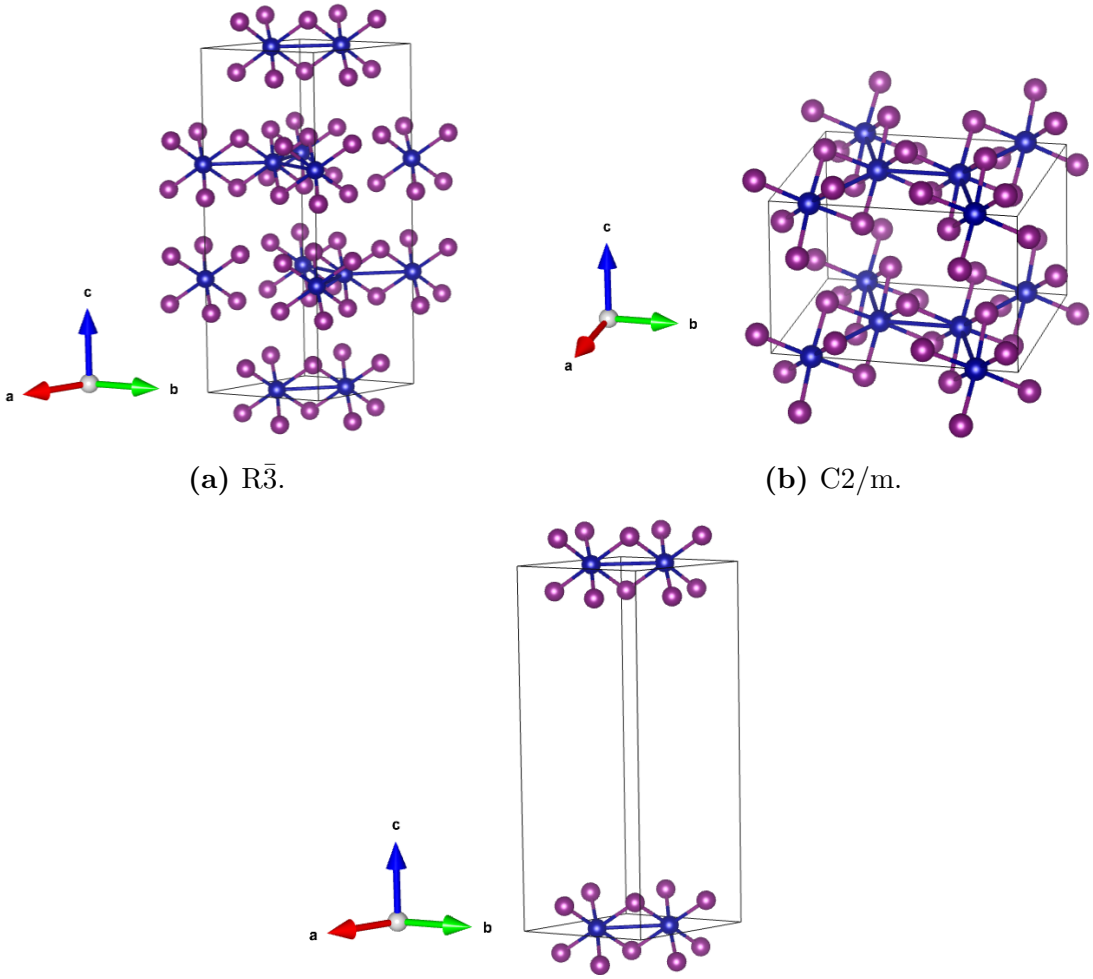

(a) R$\bar{3}$.

(b) C2/m.

(c) P$\bar{3}$1m.

Figure 3.1: Crystal structure of the CrX_3 bulk and ML phases. Conventional unit cells for the rhombohedral **(a)** and monoclinic **(b)** bulk phases, alongside with the primitive one for the trigonal monolayer **(c)**, using the VESTA software [44–47].

Rhombohedral bulk phase ($R\bar{3}$)

	$CrCl_3$[a]	$CrBr_3$[b]	CrI_3[c]
$a = b$ (Å)	5.942	6.306	6.867
c (Å)	17.33	18.37	19.81
d_{Cr-Cr} (Å)	3.431	3.641	3.965
$\theta_{Cr-X-Cr}$ (°)	93.93	90.29	93.31
T (K)	225	273	90

Monoclinic bulk phase (C2/m)

	$CrCl_3$[a]	$CrBr_3$	CrI_3[c]
a (Å)	5.959	—	6.866
b (Å)	10.32	—	11.89
c (Å)	6.114	—	6.984
d_{Cr-Cr} (Å)	3.441, 3.439	—	3.959, 3.965
$\theta_{Cr-X-Cr}$ (°)	94.57, 94.26	—	93.63, 93.10
T (K)	298	—	250

[a] : Ref. [41]
[b] : Ref. [42]
[c] : Ref. [43]

Table 3.1: Experimental data on the CrX_3 structures at the bulk limit. The lattice constants (a, b, c), the Cr-Cr bondlength (d_{Cr-Cr}) and the Cr-X-Cr angle ($\theta_{Cr-X-Cr}$) for the rhombohedral and monoclinic structures obtained in various XRD experiments.

For what regards the monolayer limit instead, the determination of the main structural properties is actually challenging for experimental physicists and cannot be achieved by standard XRD experiments, since they typically require the samples to be at least 10 nm thick. A common approach to overcome this limitation is to perform scanning tunneling microscopy. This technique provides useful insights on the height profile of the CrX_3 monolayers at the atomic level [48, 49], but still cannot distinguish features ~ 0.1 Å. Thus, their structure is usually extracted from the associated bulk counterparts and later relaxed using DFT-based algorithms.

3.2 Electronic properties

The strong correlations between Cr d electrons are responsible for the insulating behaviour in all the chromium trihalides both at the bulk and the monolayer limit. This mechanism in fact allows to classify them as standard Mott insulators with indirect energy bandgaps, whose values scale as reported in Tab. 3.2.

Rhombohedral bulk phase ($R\bar{3}$)

	$CrCl_3$	$CrBr_3$	CrI_3
PBE[b]	1.45	1.18	0.91
HSE06[b]	3.31	2.40	1.29
Exp. Refs.	2.5[a]	2.0[a]	1.2[b]

Trigonal ML phase ($P\bar{3}1m$)

	$CrCl_3$	$CrBr_3$	CrI_3
PBE[b]	1.52	1.33	1.14
HSE06[b]	3.44	2.54	1.52

[a] : Ref. [50]
[b] : Ref. [51]

Table 3.2: Energy bandgaps for the rhombohedral bulk phases and the trigonal MLs. The experimental reference values are obtained via photoemission spectroscopy and are only given in the first table, while the computational estimates are derived from DFT-based electronic structure calculations with the PBE exchange-correlation functional of the HSE06 hybrid functional.

As expected, the results from photoemission experiments are reproduced by the numerical analogues only when the DFT treatment of d bands is improved using more advanced approaches, such as hybrid functionals, Hubbard (+U) corrections or even quantum many-body techniques.

Furthermore, according to crystal-field theory for edge-sharing octahedral systems, the Cr d orbitals are energetically separated to form a low-lying triply-degenerate t_{2g} and high-lying doubly-degenerate e_g levels. At the same time, the effective number of d electrons localized at the Cr sites is actually lower than what we could expect from the electronic configuration of the isolated Cr atom ($[Ar]3d^5 4s$) and the cause of this phenomenon has to be attributed to the strong electronegativity of ligands' atoms.

Therefore, the ground state configuration is straightforwardly obtained by populating the t_{2g} states with three spin-up electrons in such a way that both the Pauli exclusion principle and the empirical Hund's rules are satisfied. This implies that the orbital and spin quantum numbers for the whole d shell are respectively $L = 0$ and $S = 3/2$, using the quantum mechanical laws for the summation of angular momentum operators. When SOC is included, the Cr electronic ground state is indeed a $J = 3/2$ multiplet.

3.3 Magnetic properties

All bulk chromium trihalides are known to undergo a magnetic phase tansition at low temperatures, but the most stable spin configuration and the ordering temperature strongly depend on the chosen halide. For instance, bulk $CrBr_3$ and CrI_3 become robust ferromagnets below the Curie temperatures $T_C = 37$ K [52] and 68 K [53] respectively, while bulk $CrCl_3$ turns out to be a layered antiferromagnet with the Néel temperature $T_N = 17$ K [54]. So basically the critical temperature $T_{C/N}$ grows with halide's mass or equivalently SOC, suggesting that the latter plays a key role in the enhancement of the magnetically ordered phase's tolerance to thermal excitations. Also the strength of the local magnetic moments follow a similar trend and they tend to align to (lie on) the c axis (a-b plane) for bulk $CrBr_3$ and CrI_3 ($CrCl_3$).

Despite the results of the Mermin-Wagner theorem, the magnetic long-range order is achieved at the monolayer limit, too. As anticipated in Sec. 1.3, such a violation derives from the onset of non-negligible anisotropic contributions to the IEI or SIA tensors. In the specific case of CrX_3 MLs, the dominant anisotropic terms arises from second-neighbour DM and diagonal symmetric exchange interactions, since the first Moriya rule (see Tab. 1.1) is satisfied by the local environment of the 1°NN bonds.

Since the Cr-X-Cr angles are always close to 90° for all the bulk and ML phases, the 1°NN intralayer exchange interaction is always governed by the competition between the direct exchange and the 90°-oriented superexchange. The first mechanism provides a weakly AFM contribution due to the large distances between neighbouring Cr atoms, while the second one is expected to be strongly FM. This results in an effective FM exchange coupling that energetically favors a parallel alignment of the Cr spins within each layer.

As a consequence, all the ML phases become ferromagnets at slightly lower Curie temperatures $T_C = 13$ K [55], 27 K [56] and 45 K [57] for $CrCl_3$, $CrBr_3$ and CrI_3 respectively.

The only exception to this rule is the $CrCl_3$ rhomboedral bulk phase, which in fact differ by the sign of interlayer exchange coupling.

Chapter 4

Results

Here we discuss the main results on the magnetic properties of the CrX_3 series under study. In particular, this chapter is developped around three objectives: the structural relaxation of ML phases, the evaluation of exchange interactions for the initial few NN shells, and the characterization of the associated magnetic transitions. The procedures required to accomplish these tasks are meticulously detailed.
Using DFT with PBEsol [58] exchange-correlation functional, Hubbard-U correction and SOC term, we are able to reproduce the CrX_3 ML structures in good agreement with the experimental bulk analogues and previous computational works. We also target the main IEI and SIA parameters by applying the four-states method. The analysis of the so obtained coupling constants focuses on underlining the crucial role of the halide's SOC and allows to identify the major contributions to the overall exchange interactions. These results are finally used to perform Monte Carlo simulations, aiming at assessing the effect of finite temperatures on a set of relevant observables, including the average magnetization. The Curie temperatures of the CrX_3 MLs can be thus calculated and compared to the available experimental reference values, which are however systematically lower than our estimates.

4.1 Structural relaxation

In contrast with the rhombohedral bulk phase, the current knowledge of the trigonal ML structures is not accurate enough to take the available experimental data as a reliable starting point for the investigation of their magnetic interactions, as they are in fact very sensitive to small variations of the interatomic distances [59].

$CrCl_3$ ML

	This work	Bulk analogue[a]	Previous work[d]
a (Å)	5.979	5.942	5.967
d_{Cr-Cr} (Å)	3.452	3.431	—
$\theta_{Cr-X-Cr}$ (°)	94.57	93.93	—

$CrBr_3$ ML

	This work	Bulk analogue[a]	Previous work[d]
a (Å)	6.344	6.306	6.326
d_{Cr-Cr} (Å)	3.662	3.641	—
$\theta_{Cr-X-Cr}$ (°)	93.86	90.29	—

CrI_3 ML

	This work	Bulk analogue[a]	Previous work[d]
a (Å)	6.894	6.867	6.856
d_{Cr-Cr} (Å)	3.980	3.965	—
$\theta_{Cr-X-Cr}$ (°)	93.62	93.31	—

[a] : Ref. [41]
[b] : Ref. [42]
[c] : Ref. [43]
[d] : Ref. [60]

Table 4.1: Main structural parameters for the relaxed CrX_3 FM MLs. The in-plane lattice constant (a), the Cr-Cr bondlength (d_{Cr-Cr}) and the Cr-X-Cr angle ($\theta_{Cr-X-Cr}$) for all the CrX_3 FM MLs. Bulk analogous quantities and an exemplary computational estimate are also reported to facilitate the comparison with our results.

So we chose to optimize the atomic positions of the ground-state FM ML phases through a DFT-based structural relaxation method, as implemented in the VASP framework. It goes under the name of Residual-Minimization Method Direct Inversion in the Iterative Subspace (RMM-DIIS) algorithm [61] and provides the aimed search directions from very accurate estimates of the forces and the stress tensor. One of the necessary inputs is an initial guess for the ML structure, which in practice was built by substituting the second and third CrX_3 layers in Fig. 3.1a with an empty region of about 20 Åalong the c axis in order to suppress any spurious interaction between the remaining layer and its replicas due to the 3D periodic boundary conditions. Intending to ensure a high accuracy, we also performed a series of convergence tests with respect to the total energy difference between two distinct magnetic configurations down to the $\sim 10^{-6}$ eV order of magnitude. This resulted in a $6 \times 6 \times 1$ k-mesh grid and an energy cutoff

E_{cut} = 450 eV, together with an electronic stop criterion of 10^{-6} eV and a Gaussian smearing width of 0.01 eV for an improved k-space integration. Moreover, the electronic self-consistent cycles were featured by the use of the PBEsol exchange-correlation functional and the incorporation of the SOC effect and the Dudarev's correction terms with $U_{eff} = U - J = 3.0$ eV for Cr d orbitals, in accordance with the constrained Random Phase Approximation (cRPA) data in [62]. Finally, the relaxation procedure was stopped when the norms of all the forces were smaller than 1 meV/Å.

All the most relevant outcomes are presented in Tab. 4.1, along with the experimental data for the rhombohedral bulk counterparts and some computational estimates from a previous *ab initio* calculation that used the same exchange-correlation functional. As a matter of fact, both the in-plane lattice constants and the Cr-Cr bondlengths exhibit an increasing trend passing from a lower to a higher halide mass, while the Cr-X-Cr angles remain nearly unchanged. At the same time, the comparison indicates a high degree of compatibility with the reference values, as our results deviate by no more than 3 %.

4.2 Intersite exchange tensors

The computation of the here reported exchange couplings follows the instructions of the four-states energy-mapping method detailed in Sec. 2.4. In particular, we extended the previous setup for the electronic self-consistent cycles to account for all the necessary spin configurations within VASP. For this purpose, we constrained the local magnetic moments in the system along the desired directions as described in Sec. 2.3 and employed a two-steps procedure to minimize the penalty energy contributions down to $\sim$1 μeV. This turned out to be possible by first performing an electronic self-consistent cycle with LAMBDA=10 and then by restarting the pre-converged calculation with LAMBDA=100. Moreover, in order to isolate the spin pair of interest from their replicas, we adopted a supercell solution that is briefly summarized in Tab. 4.2.

	CrX_3 rhombohedral bulk			CrX_3 ML	
	1°NN	2°NN	3°NN	1°NN	2°NN
Supercell	2×2×2	2×2×2	2×2×3	2×2×1	3×3×1
K-mesh grid	3×3×3	3×3×3	3×3×2	3×3×1	2×2×1

Table 4.2: Supercell solutions for the four-states method in the CrX_3 periodic systems. The choice of the number of elementary unit cells within each supercell solution is aimed to minimize the spurious exchange interactions between spin pair's replicas. The elementary unit cell for the CrX_3 rhombohedral bulk phases (trigonal MLs) consists of the experimental (relaxed) primitive cell. Also, the changes in the k-mesh grid follow the usual inverse proportionality with the number of unit cells per lattice vector, starting from 6×6×6 (6×6×1) for the bulk (ML) primitive unit cell.

For the sake of a practical distinction between the various anisotropic and isotropic contribution to the so obtained IEI tensors $\{J = J^{(i^*j^*)}\}$, we propose the following parametrization of the associated 3×3 matrices

$$J = \begin{bmatrix} J_{xx} & J_{xy} & J_{xz} \\ J_{yx} & J_{yy} & J_{yz} \\ J_{zx} & J_{zy} & J_{zz} \end{bmatrix} = \begin{bmatrix} \bar{J} + K_x & \Gamma_{xy} + D_z & \Gamma_{xz} - D_y \\ \Gamma_{xy} - D_z & \bar{J} + K_y & \Gamma_{yz} + D_x \\ \Gamma_{xz} + D_y & \Gamma_{yz} - D_x & \bar{J} + K_z \end{bmatrix} \tag{4.1}$$

where

$$\begin{aligned} \bar{J} &= \frac{1}{3}(J_{xx} + J_{yy} + J_{zz}), \\ \vec{D} &= (D_x, D_y, D_z) = \frac{1}{2}(J_{yz} - J_{zy}, J_{zx} - J_{xz}, J_{xy} - J_{yx}), \\ \vec{\Gamma} &= (\Gamma_{xy}, \Gamma_{xz}, \Gamma_{yz}) = \frac{1}{2}(J_{xy} + J_{yx}, J_{xz} + J_{zx}, J_{yz} + J_{zy}), \\ \vec{K} &= (K_x, K_y, K_z) = (J_{xx}, J_{yy}, J_{zz}) - \bar{J}. \end{aligned} \tag{4.2}$$

This allows to represent the isotropic, the antisymmetric DM, the off-diagonal symmetric and the diagonal symmetric exchange interaction in terms of scalar or 3D vector parameters. Their strength is thoroughly reported in Figs. 4.1, 4.2 and 4.3 for the first few NN shells of the rhombohedral bulk phases and the trigonal MLs.

As the plots in Fig. 4.1a show, the isotropic contribution to the first NN intralayer exchange interactions $\bar{J}$ is always negative and thus favours a FM alignment of the Cr local magnetic moments. It also turns out to decrease significantly as the associated ligand's SOC increases. This trend can be attributed to the dependence of the FM superexchange coupling (see Eq. 1.36) on the effective hopping integral between Cr d orbitals, which clearly grows as $\sim t_{pd}^2$. Indeed, as the delocalization of the X p electrons intensifies passing from $CrCl_3$ to CrI_3, we expect that the overlap between the X p and Cr d orbitals considerably increases, leading to a larger t_{pd} and thus an even lower isotropic term. Further, we note that $\bar{J}$ take lower values for the rhombohedral bulk phases than for the trigonal MLs by almost $\sim 10\%$.

The anisotropic contributions to the first NN intralayer exchange interactions are instead shown in Figs. 4.1b, 4.1c, 4.1d. The DM term $|\vec{D}|$ is clearly weaker than the others by at least an order of magnitude as a direct consequence of the first Moriya rule. Differently, the symmetric exchange couplings $|\vec{\Gamma}|$ and $|\vec{K}|$ take non-negligible values that are strongly enhanced by the increasing halide's SOC. This feature is observed for both the rhombohedral bulk phases and the trigonal MLs.

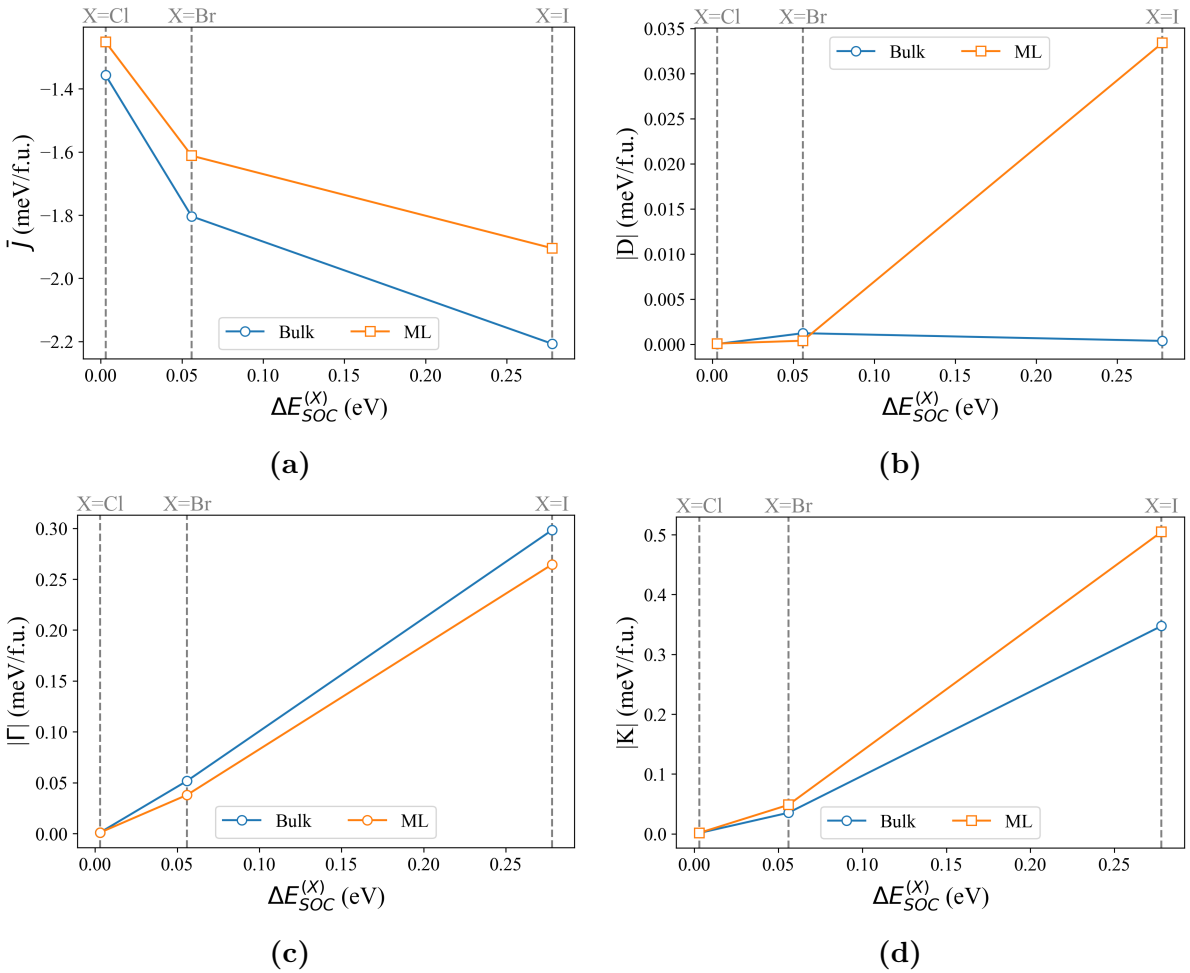

Figure 4.1: 1°NN intralayer exchange parameters as a function of the halide's SOC energy. The isotropic **(a)**, the antisymmetric DM **(b)**, the off-diagonal symmetric **(c)** and the diagonal symmetric exchange **(d)** for all the CrX_3 rhombohedral bulk phases and trigonal MLs, stressing the impact of the halide's SOC energy ($\Delta E_{SOC}^{(X)}$).

Besides, recent ferromagnetic resonance (FMR) experiments [63] have reported that the first NN exchange interactions are indeed enhanced by the halide's SOC as we pointed out. However, some of their findings do not align well with our estimates. As a matter of fact, they suggest that our $|\bar{J}|$ values for the $CrCl_3$ and $CrBr_3$ MLs are actually overestimated. Also they report quite different symmetric anisotropic contributions, for instance $|\Gamma| \simeq 0.08$ meV and $|K| \simeq 0.9$ meV in the case of CrI_3 ML.

Almost in continuity to the just commented IEI tensor, we find that the second NN intralayer exchange interactions are also enhanced by the halide's SOC. Nonetheless, the anisotropic contributions hardly exceed the tens of μeV, if it was not for the exceptional case of CrI_3 ML where they even reach the hundreds of μeV.

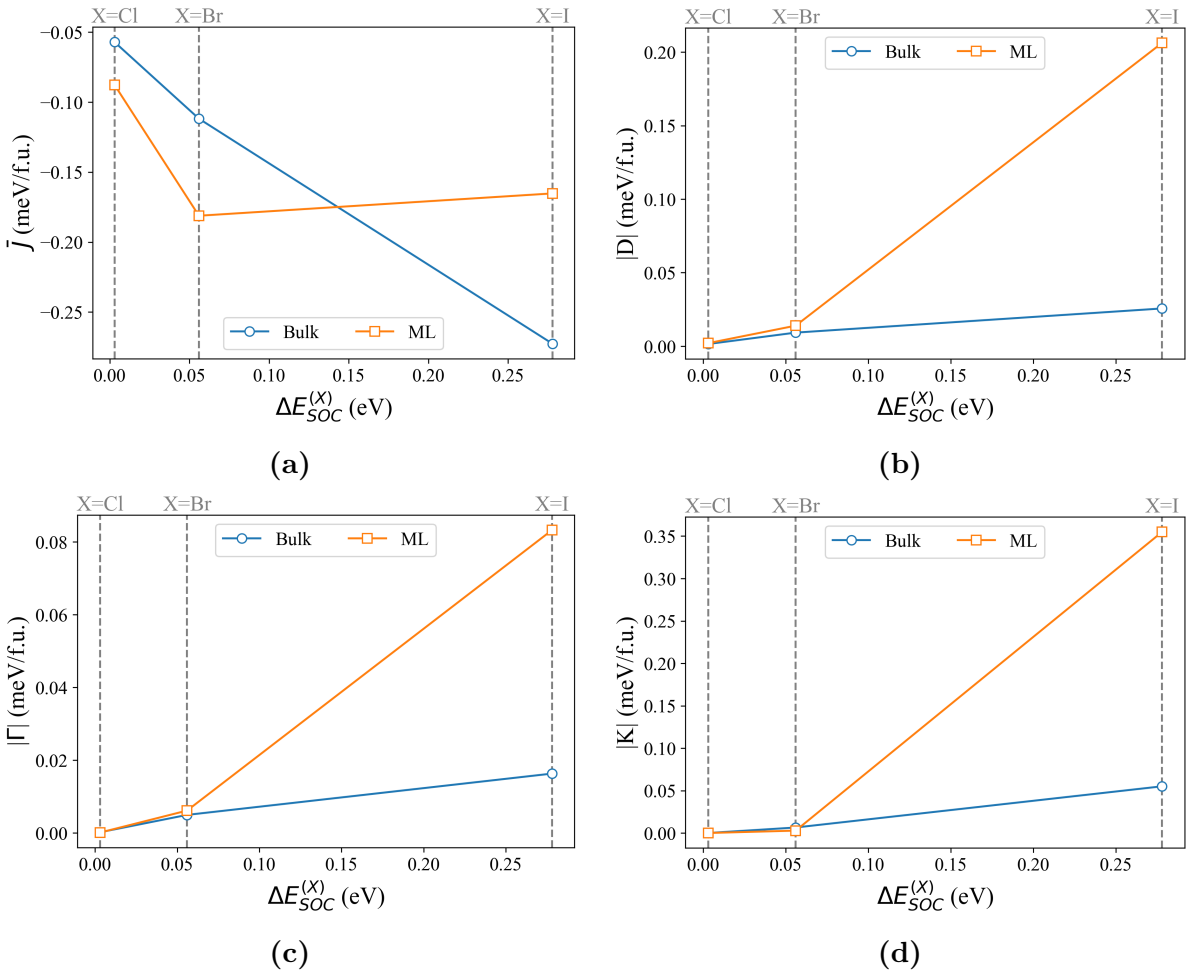

Figure 4.2: 2°NN intralayer exchange parameters as a function of the halide's SOC energy. The isotropic **(a)**, the antisymmetric DM **(b)**, the off-diagonal symmetric **(c)** and the diagonal symmetric exchange **(d)** for all the CrX_3 rhombohedral bulk phases and trigonal MLs, stressing the impact of the halide's SOC energy ($\Delta E_{SOC}^{(X)}$).

The results of the previous computational work [60] further confirm that the first (second) NN isotropic term should take higher (lower) values than our estimate.

Finally, the focus shifts to the features of the interlayer IEI tensors, which are summarized in the plots of Fig. 4.3. Since only the diagonal anisotropic and the isotropic contributions are actually non-vanishing, they reduce to a mere diagonal shape with a strong out-of-plane anisotropy. More interestingly, the isotropic term for the $CrCl_3$ rhombohedral bulk phase becomes positive, in accordance with the experimental evidence of layered antiferromagnetism in that case.

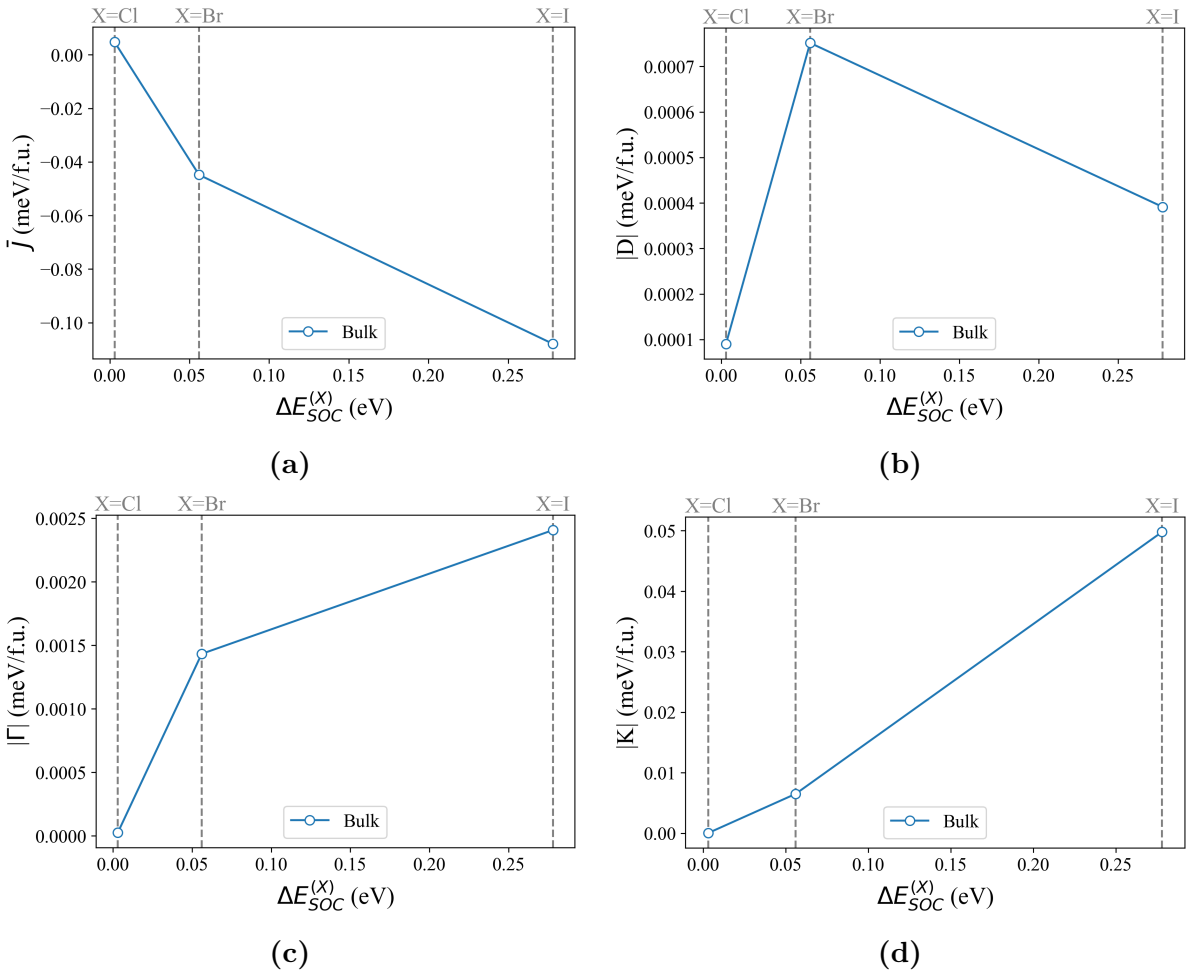

Figure 4.3: 1°NN interlayer exchange parameters as a function of the halide's SOC energy. The isotropic **(a)**, the antisymmetric DM **(b)**, the off-diagonal symmetric **(c)** and the diagonal symmetric exchange **(d)** for all the CrX_3 rhombohedral bulk phases and trigonal MLs, stressing the impact of the halide's SOC energy ($\Delta E_{SOC}^{(X)}$).

It is worth noting that the IEI tensors obtained by the four-states formula refer to the specific spin quantization frame assumed by VASP during the total energy calculations. So, before any of the previous considerations, we made sure to express them in a local reference frame common to all the CrX_3 supercells. Since the choice is arbitrary, we set the x and z axes to be aligned with the interested NN bond and the c lattice direction respectively. If that was not the case by default, the defective IEI tensors J were transformed into

$$J' = R_z^{-1} J R_z \tag{4.3}$$

with R_z as the matrix representation of the rotations around the z axis required to adjust the orientation of the reference frame.

4.3 Single-ion anisotropy

Adopting the same exact computational setup as for the calculation of the first NN IEI tensors, we can compute the dominant SIA term $A_{zz} - A_{xx}$ according to the four-states formula in Eq. 2.50 by imposing $\alpha^* = z$. As the plot in Fig. 4.4 shows, the strength of this coupling is also enhanced by the halide's SOC and reaches significantly non-zero values in the specific case of CrI_3.

Moreover, the vanishment of all other contributions can be ascribed to the symmetry considerations in Ref. [33] for the CrX_3 MLs. For what regards the rhombohedral bulk phases instead, they are not valid. So we report the associated $|A_{zz} - A_{xx}|$ values only for comparative purposes.

Interestingly, the paper [33] also provides a following estimate of $|A_{zz} - A_{xx}| = 0.08$ meV for the CrI_3 ML phase, which turns out to be in excellent agreement with our data despite the different computational setups.

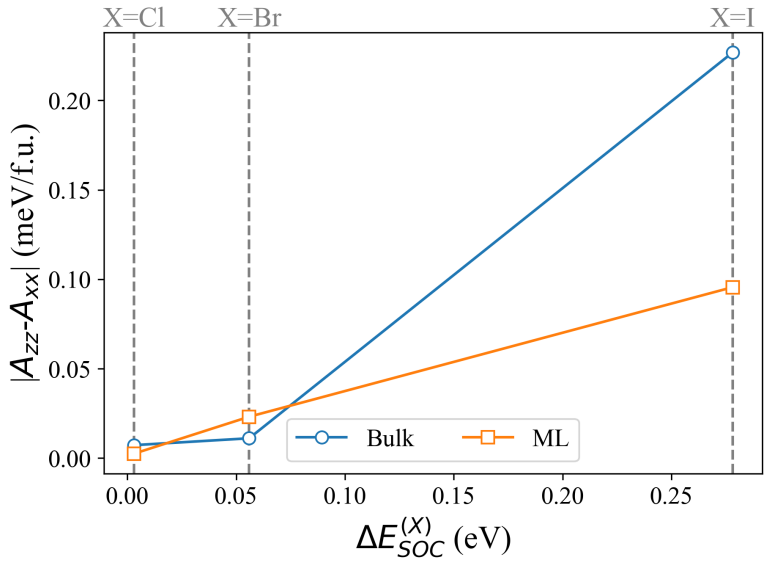

Figure 4.4: Out-of-plane SIA parameter as a function of the halide's SOC energy. The plots aim to stress the impact of the halide's SOC energy ($\Delta E^{(X)}_{SOC}$) in the enhancement of the modulus of $A_{zz} - A_{xx}$.

4.4 Thermal properties

As a first step in the presentation of the MC finite-temperature calculations, we wish to stress some important precautions to ensure a sufficient statistical stability of the MC cumulated averages. For instance, before the sampling of the observables takes place, we extend the system to a $100 \times 100 \times 1$ supercell and perform 2×10^5 thermalization steps, allowing to suppress any spurious dependence on the initial magnetic configuration. It is set to the FM ground-state predicted by the PBEsol+U+SOC method with the Cr magnetic moments' norms in Tab. 4.3.

	$CrCl_3$ ML	$CrBr_3$ ML	CrI_3 ML
$\lvert\vec{\mu}_{Cr}\rvert$ (μ_B)	3.06	3.18	3.37

Table 4.3: The Cr magnetic moments at the FM ground-state of the CrX_3 MLs. The values are compatible with the effective number of unpaired spin-up d electrons at the Cr sites and also increase with the covalent character of the associated CrX_3 MLs.

In order to optimize the representation of the thermodynamical equilibrium phase at each temperature value, we extract the cumulated averages only after 5×10^5 MC iterations. The behaviour of the resulting magnetization as the temperature grows is plotted in Figs. 4.5, alongside with experimental data from recent X-ray Magnetic Circular Dichroism (XMCD) studies [55, 57] and polarization-resolved magnetophotoluminescence (MPL) analyses [56]. By fitting both the experimental and MC data with a function of the form

$$\frac{M(T)}{M(0)} = \left(1 - \frac{T}{T_C}\right)^{\beta}, \tag{4.4}$$

we end up with two independent estimates for the Curie temperature T_C and the critical exponent β that are summarized in Tab. 4.4.

		$CrCl_3$ ML	$CrBr_3$ ML	CrI_3 ML
T_C (K)	Exp. fit:	12.95±0.03	33±1	44.60±0.08
	MC fit:	33.1±0.3	51.6±0.3	68.2±0.7
β	Exp. fit:	0.23±0.02	0.29±0.05	0.123±0.008
	MC fit:	0.38±0.01	0.29±0.01	0.35±0.01

Table 4.4: The Curie temperature and the critical exponent for all the CrX_3 MLs. The here presented estimates are obtained by fitting the experimental data and the MC average magnetization values to the functional form of Eq. 4.4.

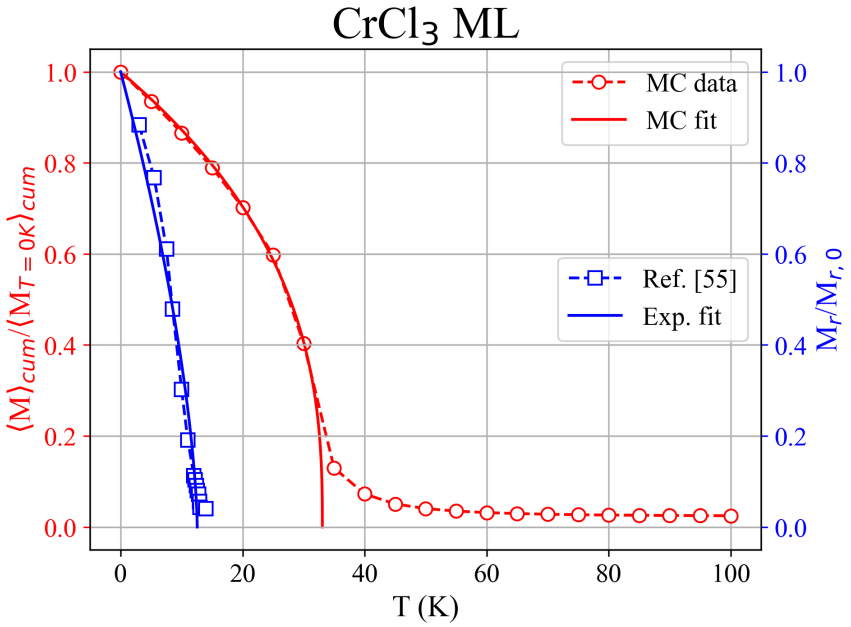
CrCl3 ML
MC data
MC fit
Ref. [55]
Exp. fit
⟨M⟩cum/⟨MT=0K⟩cum
Mr/Mr,0
T (K)

(a)

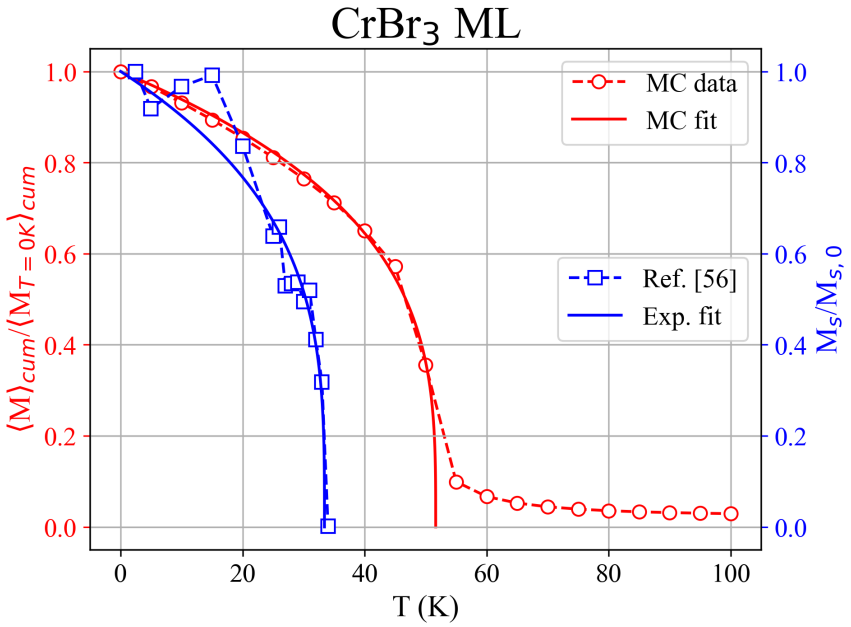
CrBr3 ML
MC data
MC fit
Ref. [56]
Exp. fit
⟨M⟩cum/⟨MT=0K⟩cum
Ms/Ms,0
T (K)

(b)

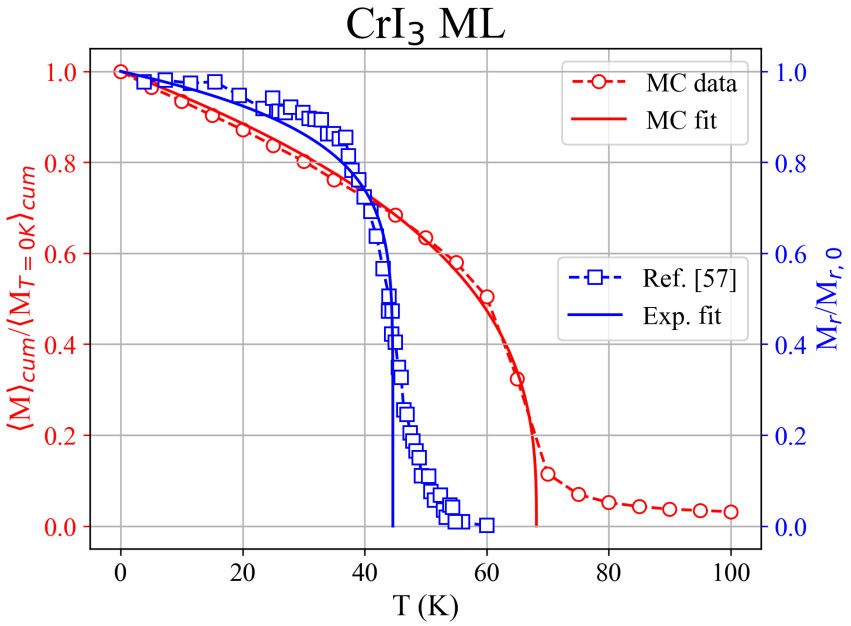

(c)

Figure 4.5: Temperature dependence of the magnetization in CrX_3 MLs. The cumulated average magnetization from the MC simulations are here plotted in the temperature range [0 K; 100 K] with steps of 5 K for $CrCl_3$ **(a)**, $CrBr_3$ **(b)** and CrI_3 **(c)**. They are compared to the experimental data of Refs. [55–57] and are also fitted to the functional form of Eq. 4.4.

They correctly reproduce the increasing trend with the halide's mass, but also result in a significant overestimation of the Curie temperatures of the CrX_3 MLs. A candidate hypothesis for such a discrepancy regards the input IEI tensors obtained by the four-states method. Indeed, the isotropic contribution to the first NN intralayer exchange coupling turned out to be considerably lower than the reference values for the $CrCl_3$ and $CrBr_3$ MLs. However, this is not valid for the CrI_3 ML. One would need to perform further tests to identify the origin of the overestimated T_C in this case.

For the sake of completeness, we also report the magnetic susceptibility, the magnetic specific heat and the 4^{th} order Binder cumulant as a function of the temperature in Figs. 4.6, 4.7 and 4.8.

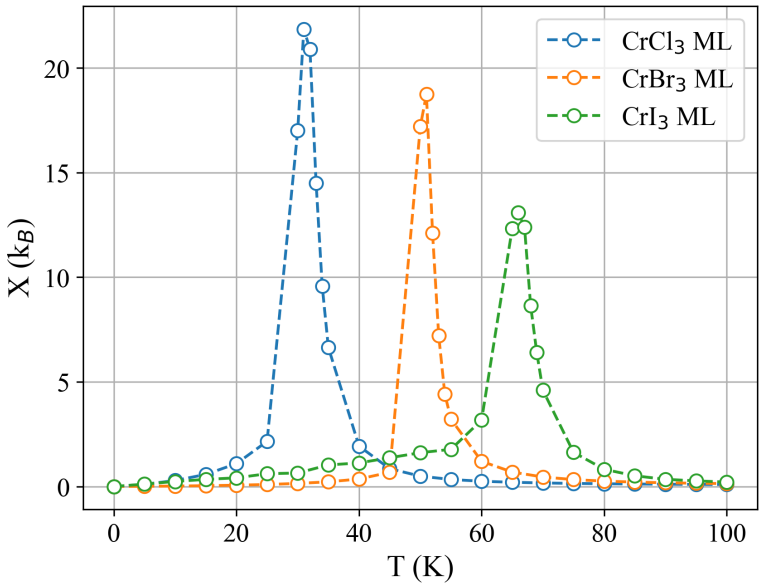

Figure 4.6: Temperature dependence of the magnetic susceptibility in CrX_3 MLs. The data shows a sharp peaked behaviour in correspondence to the MC estimates of the Curie temperature of the CrX_3 MLs.

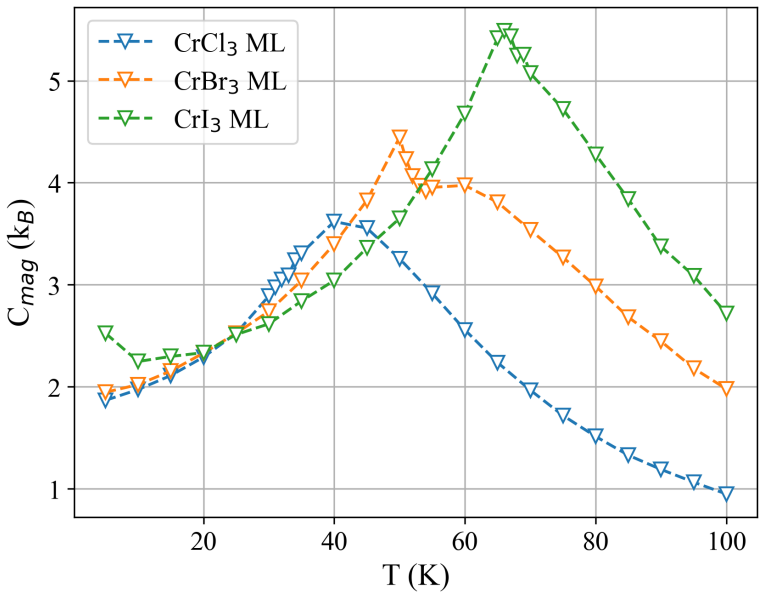

Figure 4.7: Temperature dependence of the magnetic specific heat in CrX_3 MLs. The data shows a broad peak just above the MC estimates of the Curie temperature of the CrX_3 MLs.

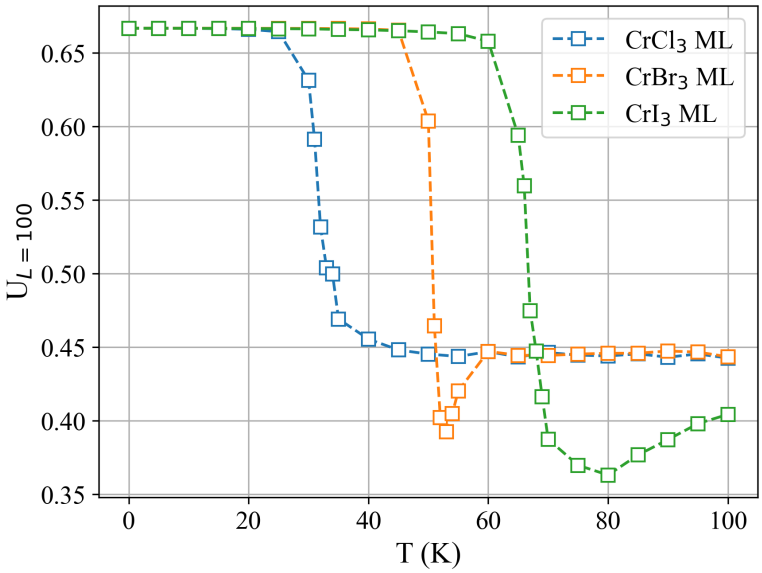

Figure 4.8: Temperature dependence of the 4^{th} order Binder cumulant in CrX_3 MLs. The data shows a steady trend to $\sim \frac{2}{3}$ for low temperatures and a rapid decrease in correspondence to the MC estimates of the Curie temperature of the CrX_3 MLs. Also they approach $\sim \frac{4}{9}$ asymptotically in the high temperature range.

Conclusions

This study aims to contribute to the extensive body of experimental and theoretical research in the field of 2D magnetic materials, focusing specifically on the chromium trihalide series CrX_3 with X = Cl, Br and I. In particular, we present some fundamental models explaining the intrinsically quantum mechanical origin of magnetism in solids and propose the use of various computational methods to characterize the structural, electronic, and magnetic properties of the materials in object at both bulk and ML limits. The objective is to validate the accuracy of these techniques in calculating the IEI and SIA tensors, and to use the so determined values to gain useful insights into the magnetic behavior of the CrX_3 MLs at finite temperatures.

To begin with, the output data from the structural relaxation of the CrX_3 MLs, using the DFT+U+SOC method and the PBEsol exchange-correlation functional show an excellent agreement with previous XRD measurements for the analogous quantities in bulk, as well as with prior computational relaxations.

The four-states methodology is thus employed to address the nature of the exchange interactions in both the low-temperature rhombohedral bulk phases and the trigonal MLs. As recent FMR experiments and *ab initio* calculations claim, our results evidence the crucial role of the halide's SOC in the enhancement of the isotropic and anisotropic contributions to the IEI and SIA tensors, but also we report some non-negligible discrepancies with the references. For instance, our findings on the first NN isotropic term of the $CrCl_3$ and $CrBr_3$ MLs are significantly lower than the reference values and the anisotropic-to-isotropic ratio $\frac{|K|}{|J|}$ $\left(\frac{|\Gamma|}{|J|}\right)$ for the first NN intralayer IEI tensor of the CrI_3 ML is ~ 0.26 (~ 0.13) against the expected ~ 0.40 (~ 0.04). For what regargs the second NN intralayer exchange interactions instead, we observe that the enhancement effect of the anisotropic contributions due to the halide's SOC is much stronger in the trigonal MLs than in the rhombohedral bulk phases. Further, the interlayer IEI tensor for the latter materials takes a diagonal form and its isotropic contribution changes sign in the case of $CrCl_3$.

In conclusion, we use the IEI and SIA tensors obtained by the four-states energy-mapping method and we systematically perform MC simulations based on the Metropolis algorithm for an efficient exploration of the magnetic configurations' space to gain useful insights on the behaviour of the CrX_3 MLs at finite temperatures. The cumulated average

magnetization is thus fitted to the functional form of Eq. 4.4 and compared to XMCD and MPL data. We find that our estimates for the Curie temperatures are significantly overestimated and this may be attributed to the discrepancies we have reported above for the first NN intralayer IEI tensor of the CrX_3 MLs. Further calculations could be used to confirm or reject this hypothesis and also can investigate other interesting aspects of the physics of these materials, such as the spin exchange stiffness and the adiabatic magnon spectra.

Appendices

Appendix A

Input files

A.1 Structural relaxation by VASP

In this Appendix, we report all the VASP input files used for the structural relaxation of the CrX_3 MLs. Further details on the meaning of the flags can be found on the VASP Wiki website.

- **POSCAR**

```
CrCl3 ML extracted from the bulk experimental structure
1.0
        5.9419999123         0.0000000000         0.0000000000
        -2.9709999561         5.1459228733         0.0000000000
        0.0000000000         0.0000000000        20.0000000000
Cr   Cl
2    6
Cartesian
        2.971000045          1.715307676          0.017910640
        0.000000000          3.430615351         -0.017910295
        0.917741705          5.107328489          1.312108113
        -1.910947041          3.387046260          1.312108113
        -1.060052843          1.758876613         -1.312106821
        0.993205408          1.797470998          1.312108113
        1.977794548          3.348451875         -1.312106821
        -0.917741726          5.184517294         -1.312106821

CrBr3 ML extracted from the bulk experimental structure
1.0
        6.3060007095         0.0000000000         0.0000000000
```

```
        -3.1530003548          5.4611568107          0.0000000000
        0.0000000000          0.0000000000         20.0000000000
Cr   Br
2    6
Cartesian
        0.000000000          3.640771316          0.000000000
        3.153000449          1.820385658         -0.003489945
        1.021414912          1.878401361          1.426585837
        2.036964232          3.644157599         -1.426585837
        2.131585349         -0.058015703         -1.426585837
        4.168549769         -0.054629419          1.426585837
        5.290451137          1.875015077         -1.426585837
        4.269036349          3.637385032          1.426585837

CrI3 ML extracted from the bulk experimental structure
1.0
        6.8669972420          0.0000000000          0.0000000000
        -3.4334986210         5.9469940593          0.0000000000
        0.0000000000          0.0000000000         20.0000000000
Cr  I
2   6
Cartesian
        3.433498723          1.982331412         -0.006866305
        0.000000000          3.964662824          0.006866510
        2.406882722          0.007136393          1.564158131
        2.236237697          3.859004281          1.564158131
        1.197260720          2.087989778         -1.564157393
        5.657375411          2.080853442          1.564159311
        4.460114589         -0.007136514         -1.564159754
        4.643120316          3.866140795         -1.564157393
```

- **KPOINTS**

```
Gamma-centered K-mesh Grid
0
Gamma
6 6 1
```

- **INCAR**

```
SYSTEM = CrX3_ML
```

```
# Parallelization Tags
NCORE = 32
KPAR = 2

# Electronic SC loop
GGA = PS
LREAL = .FALSE.
ENCUT = 450.0
PREC = A
EDIFF = 1E-6
NELM = 200
ISMEAR = 0
SIGMA = 0.01

# Ionic relaxation
NSW = 60
ISIF = 8
IBRION = 1
EDIFFG = -0.001
NELMIN = 6

# Method Settings
LDAU = .TRUE.
LSORBIT = .TRUE.

# Density Mixing
AMIN = 0.4
AMIX = 0.3
BMIX = 0.0001
AMIX_MAG = 0.6
BMIX_MAG = 0.0001

# Dudarev Approach to DFT+U
LDAUTYPE = 2
LDAUL = 2 -1
LDAUU = 3.0 0.0
LDAUJ = 0.0 0.0
LDAUPRINT = 1
LMAXMIX = 4
```

A.2 Total energy calculation by VASP

All the VASP input files reported below refer to the CrI_3 ML and specifically allow for the determination of the total energy E_3 in Eq. 2.46 if $i^* = 1$, $j^* = 5$, $\alpha^* = y$ and $\beta^* = z$.

- **POSCAR**

```
CrI3 ML after structural relaxation
1.0
        13.7885494232        0.0000000000        0.0000000000
        -6.8942747116       11.9412340818        0.0000000000
         0.0000000000        0.0000000000       20.0794448853
Cr   I
8   24
Cartesian
         3.447137458          1.990205739          0.000000000
         0.000000102          7.960822780          0.000000000
        10.34141217           1.990205739          0.000000000
         6.894274814          7.960822780          0.000000000
         0.000000000          3.980411479          0.000000000
        -3.44713735           9.951028520          0.000000000
         6.894274712          3.980411479          0.000000000
         3.447137356          9.951028520          0.000000000
         2.434617123          0.000073928          1.569941179
        -1.01252023           5.970690969          1.569941179
         9.328891834          0.000073928          1.569941179
         5.881754478          5.970690969          1.569941179
         2.229892958          3.862139800          1.569941179
        -1.21724439           9.832756841          1.569941179
         9.124167670          3.862139800          1.569941179
         5.677030314          9.832756841          1.569941179
         1.217244193          2.108477241         -1.569940438
        -2.22989316           8.079094282         -1.569940438
         8.111518905          2.108477241         -1.569940438
         4.664381549          8.079094282         -1.569940438
        -1.21737275           2.108403370          1.569942363
        -4.66451011           8.079020411          1.569942363
         5.676901954          2.108403370          1.569942363
         2.229764598          8.079020411          1.569942363
         4.459657658         -0.00007405          -1.569942808
         1.012520303          5.970542991         -1.569942808
        11.35393237          -0.00007405          -1.569942808
```

```
7.906795014        5.970542991        -1.569942808
-2.22976473        3.862213849        -1.569940438
-5.67690209        9.832830890        -1.569940438
4.664509977        3.862213849        -1.569940438
1.217372621        9.832830890        -1.569940438
```

- **KPOINTS**

```
Gamma-centered K-mesh Grid
0
Gamma
3 3 1
```

- **INCAR**

```
SYSTEM = CrI3_ML

# Parallelization Tags
NCORE = 32
KPAR = 2

# Electronic SC loop
ISTART = 1 ! the WAVECAR and CHGCAR file are read from
ICHARG = 1 ! a pre-converged calculation with LAMBDA=10
GGA = PS
LREAL = .FALSE.
ENCUT = 450.0
PREC = A
EDIFF = 1E-7
NELM = 200
ISMEAR = 0
SIGMA = 0.01

# Spin treatment
LORBIT = 11
LNONCOLLINEAR = .TRUE.
GGA_COMPAT = .FALSE.
LASPH = .TRUE.
I_CONSTRAINED_M = 1
LAMBDA = 100 ! or LAMBDA=10 for the preliminary calculation
MAGMOM = 0.0 -4.0 0.0 4.0 0.0 0.0 4.0 0.0 0.0 4.0 0.0 0.0 0.0 0.0 4.0 ...
M_CONSTR = 0.0 -4.0 0.0 4.0 0.0 0.0 4.0 0.0 0.0 4.0 0.0 0.0 0.0 0.0 4.0 ...
```

```
RWIGS = 1.323 1.487 ! to be read from the POTCAR file
SAXIS = 0 0 1

# Density Mixing
AMIN = 0.4
AMIX = 0.2
BMIX = 0.0001
AMIX_MAG = 0.6
BMIX_MAG = 0.0001

# Method Settings
LDAU = .TRUE.
LSORBIT = .TRUE.

# Dudarev Approach to DFT+U
LDAUTYPE = 2
LDAUL = 2 -1
LDAUU = 3.0 0.0
LDAUJ = 0.0 0.0
LDAUPRINT = 1
LMAXMIX = 4
```

A.3 Monte Carlo simulations by UppASD

In this Appendix, we report all the UppASD input files used for the MC simulations that allowed us to represent the magnetic behaviour of the CrX_3 MLs at finite temperatures. Further details on the meaning of the flags can be found on the UppASD Git-hub page.

- **inpsd.dat**

```
simid CrI3_ML

# System settings
ncell             100       100       1
BC                P         P         0
cell
 5.970617241502998        3.447137471609976        0.0000000000000000
 -5.97061724150299        3.447137471609976        0.0000000000000000
 0.000000000000000        0.000000000000000        20.079445790521326
sym               0
mensemble         10
```

```
# Verbosity settings
do_prnstruct         1
do_prn_poscar         1
do_hoc_debug          1

# Path to input files
posfile     ./posfile
momfile     ./momfile
exchange    ./jfile
anisotropy  ./kfile

# Reading specifics
do_jtensor    1
calc_jtensor  .false.
do_anisotropy 1
posfiletype   D
initmag       3

# Initial phase settings
ip_mode    M
ip_temp    TEMP
ip_mcnstep 200000

# Measurement phase settings
mode      M
temp      TEMP
mcnstep   500000

# Observables' settings
do_avrg    Y
plotenergy 1
do_cumu    Y
```

- **posfile**

```
1 1 0.6666666864724036 0.33333334323749 0.1
2 1 0.3333333432374985 0.66666668647499 0.1
```

- **momfile**

```
1 1 3.37 0.0 0.0 1.0
```

```
2 1 3.37 0.0 0.0 1.0
```

- **jfile**

```
1 1 -0.33334 0.33334 0.0 0.3551 -0.0056 0.0009 -0.0055 0.2472 -0.0488 ...
1 1 -0.66668 -0.33334 0.0 0.2694 -0.0440 -0.0418 -0.0439 0.3329 -0.0252 ...
1 1 -0.33334 -0.66668 0.0 0.2790 0.0494 -0.0427 0.0495 0.3233 0.0237 ...
1 1 0.33334 -0.33334 0.0 0.3551 -0.0056 -0.0009 -0.0055 0.2472 0.0488 ...
1 1 0.66668 0.33334 0.0 0.2694 -0.0440 0.0418 -0.0439 0.3329 0.0252 ...
1 1 0.33334 0.66668 0.0 0.2790 0.0494 0.0427 0.0495 0.3233 -0.0237 ...
1 1 -1.4e-17 -1.0 0.0 0.0606 -0.0142 0.0051 0.0147 0.0417 -0.0197 ...
1 1  1.0 1.4e-17 0.0 0.0467 -0.0227 -0.0145 0.0062 0.0556 -0.0143 ...
1 1  1.0 1.0 0.0 0.0462 -0.0064 -0.0196 0.0225 0.0561 0.0054 0.0415 ...
1 1  2.3e-16 1.0 0.0 0.0606 -0.0142 -0.0051 0.0147 0.0417 0.0197 ...
1 1 -1.0 3.5e-16 0.0 0.0467 -0.0227 0.0145 0.0062 0.0556 0.0143 -0.0239 ...
1 1 -1.0 -1.0 0.0 0.0462 -0.0064 0.0196 0.0225 0.0561 -0.0054 -0.0415 ...
```

- **kfile**

```
1 1 -0.0158013256 0.0 0.0 0.0 1.0 0.0
2 1 -0.0158013256 0.0 0.0 0.0 1.0 0.0
```

Appendix B

Exchange interactions within Hubbard-I approximation

The DFT+DMFT(HI) approach detailed in Sec. 2.5 requires the utilization of a series of packages, specifically:

- *WIEN2k* [64] to perform electronic structure calculations using DFT within the (Linearized) Augmented Plane Wave + localized orbital ((L)APW+lo) method, eventually including the Hubbard (+U) term and/or the Spin-Orbit Coupling (SOC) as a relativistic correction;
- *dmftproj* to build the projectors to a set of localized orbitals from the *WIEN2k* output files;
- *TRIQS* [65–67] to implement fully self-consistent or one-shot DMFT calculations;
- *MagInt* [34, 35] to compute the intersite exchange tensor by the Force Theorem in Hubbard-I (FT-HI) using the DMFT atomic self-energy as input.

The chosen values for the on-site Coulomb repulsion and the Hund exchange parameters are $U = 3.0$ eV and $J_H = 0.8$ eV, in accordance with most of the previous works on chromium tihalides, such as Ref. [60].

This procedure was applied to all the CrX_3 bulk and ML phases, but we could adopt the experimental structure only in the first case due to the lack of XRD studies or the insufficient accuracy of other techniques for ultra-thin films in the scientific literature.

Thus, the crystal structure for the CrX_3 MLs were obtained by performing DFT-based relaxations via the conjugate gradient algorithm, available on VASP software. Differently from the *WIEN2k* code, VASP implements DFT using pseudopotentials [68] or the Projector-Augmented-Wave (PAW) method [69].

The electronic calculations were featured by the blocked-Davidson iterative algorithm for the diagonalization of the single-electron Koohn-Sham Hamiltonian matrices and

the Pulay density mixing scheme as set by default. Moreover, the chosen exchange-correlation functionals were standard PBE and PBEsol as it consists of a revised version of PBE especially defined to improve the estimation of structural properties of solids. As suggested by Ref. [51], the non-local *optB88-vdW* exchange potential [70] was also tested.

$CrCl_3$ ML

	PBE	PBEsol	PBE+ *optB88-vdW*	Bulk analogue[a]	PBEsol+U[d]
a (Å)	5.850	5.496	5.639	5.942	5.967
c (Å)	19.69	18.50	18.98	17.33	—
d_{Cr-Cr} (Å)	3.377	3.173	3.256	3.431	—
$\theta_{Cr-X-Cr}$ (°)	93.78	87.74	89.16	93.93	—

$CrBr_3$ ML

	PBE	PBEsol	PBE+ *optB88-vdW*	Bulk analogue[b]	PBEsol+U[d]
a (Å)	6.407	6.062	6.161	6.306	6.326
c (Å)	20.32	19.23	19.54	18.37	—
d_{Cr-Cr} (Å)	3.699	3.499	3.557	3.641	—
$\theta_{Cr-X-Cr}$ (°)	97.27	91.93	91.73	90.29	—

CrI_3 ML

	PBE	PBEsol	PBE+ *optB88-vdW*	Bulk analogue[c]	PBEsol+U[d]
a (Å)	7.013	6.746	6.775	6.867	6.856
c (Å)	20.42	19.65	19.73	19.81	—
d_{Cr-Cr} (Å)	4.049	3.895	3.911	3.965	—
$\theta_{Cr-X-Cr}$ (°)	98.62	95.32	93.80	93.31	—

[a] : Ref. [41]
[b] : Ref. [42]
[c] : Ref. [43]
[d] : Ref. [60]

Table B.1: Main structural parameters for the relaxed CrX_3 paramagnetic MLs. The in-plane (a) and out-of-plane (c) lattice constants, the Cr-Cr bondlength (d_{Cr-Cr}) and the Cr-X-Cr angle ($\theta_{Cr-X-Cr}$) for all the CrX_3 paramagnetic MLs. Bulk analogous quantities and an exemplary computational estimate are also reported to facilitate the comparison with our results.

Next, both the cut-off energy E_{cut} and the number of k-points per reciprocal lattice direction were carefully optimized until the total energy accuracy reached the threshold 0.1 meV per atom in the unit cell. The final values were $E_{cut} = 450$ eV (500 eV) for the PBE (PBEsol) functional and $13 \times 13 \times 1$ k-mesh grid for both cases.

To conclude, the stop criterion for the structural optimization loops were set to stop as soon as the total energy difference between the current iteration and the previous one was lower than 1 meV per atom in the unit cell.

First of all, we report the outcomes of the structural relaxation of the CrX_3 paramagnetic MLs into Tab. B.1, all together with reference values from the bulk experimental structure and the PBEsol+U relaxation in [60]. The use of PBEsol and PBE+$optB88-vdW$ exchange-correlation functional turns out to underestimate significantly the in-plane lattice constant a (Å) at equilibrium, resulting in lower Cr-Cr bondlengths d_{Cr-Cr} (Å) and Cr-X-Cr angles $\theta_{Cr-X-Cr}$ (°) as a consequence. This would also impact the evaluation of the IEI tensors via *MagInt* due to the undoubted relevance of orbitals' overlapping for the hopping processes that are involved in both direct exchange and super-exchange mechanisms. So we chose the PBE-relaxed structures as input to the DFT+DMFT(HI) approach.

Table B.2 instead shows the strength of the isotropic and anisotropic contributions to the IEI tensors of the first three (two) NN shells for the CrX_3 bulk (ML) phases via the LDA+DMFT(HI) approach. The related pDOS are plotted in Fig. B.1 and they also allowed to have a rough estimation of the energy bandgap E_{gap} (eV), as reported in Tab. 3.2 with some computational and experimental references.

Due to the conventional choice of the Hamiltonian as specified in Eq. 2.60, the positive isotropic exchange couplings imply that the antiparallel ordering of the Cr local magnetic moments is energetically favoured. This is however in contrast with the results from previous calculations and experiments in the scientific literature.

At the same time, one can also notice some aspects that are compatible with the expectations. For instance, when the ligands' SOC increases passing from $CrCl_3$ to CrI_3 through $CrBr_3$, an overall positive trend of the anisotropic terms ($|\vec{\Gamma}|, |\vec{K}|, |\vec{D}|$) is registered. In particular, the dominant terms apart from the isotropic ones come from the second-neighbour DM and the diagonal symmetric exchange interactions. A further increase is reported when we compare the interaction parameters for the rhombohedral bulk phase and those for the trigonal ML. This effect is especially enhanced for CrI_3, suggesting that the ligands' SOC plays indeed a fundamental role in the determination of the magnetic interactions for the CrX_3 series as expected. Moreover, due to the lower symmetry of the crystal structure for the monoclinic bulk phase the exchange couplings within each NN shell split up into two groups with slightly different associated values. So even variations of $\sim 5 \times 10^{-3}$ Å to the Cr-Cr bond lengths d_{Cr-Cr} impact on the IEI tensors, especially their isotropic component. Another interesting feature concerns the magnetic interactions of the interlayer bond, as they turn out to be purely isotropic (see the 2°NN column for the rhombohedral structures and 3°NN for the monoclinic ones).

$CrCl_3$

	Rhombohedral bulk			Monoclinic bulk			Trigonal ML	
	1°NN	2°NN	3°NN	1°NN	2°NN	3°NN	1°NN	2°NN
$\bar{J}$ (meV)	10.03	0.768	0.635	9.977,9.839	0.450,0.474	0.243	13.02	0.410
$\lvert\vec{\Gamma}\rvert$ (meV)	0.021	—	—	0.021,0.062	—	—	0.021	—
$\lvert\vec{K}\rvert$ (meV)	0.011	—	0.001	0.011,0.021	—	—	0.008	0.001
$\lvert\vec{D}\rvert$ (meV)	—	—	0.014	—	0.012	—	—	0.016

$CrBr_3$

	Rhombohedral bulk			Monoclinic bulk			Trigonal ML	
	1°NN	2°NN	3°NN	1°NN	2°NN	3°NN	1°NN	2°NN
$\bar{J}$ (meV)	6.50	0.719	0.927	5.964,5.714	0.553,0.594	0.320	8.668	0.50
$\lvert\vec{\Gamma}\rvert$ (meV)	0.019	—	—	0.011,0.007	—	—	0.017	—
$\lvert\vec{K}\rvert$ (meV)	0.011	—	0.004	0.012,0.019	0.007,0.005	—	0.008	0.009
$\lvert\vec{D}\rvert$ (meV)	—	—	0.063	—	0.047,0.050	—	—	0.060

CrI_3

	Rhombohedral bulk			Monoclinic bulk			Trigonal ML	
	1°NN	2°NN	3°NN	1°NN	2°NN	3°NN	1°NN	2°NN
$\bar{J}$ (meV)	2.772	1.170	0.861	2.899,3.041	0.775,0.868	0.480	8.919	0.752
$\lvert\vec{\Gamma}\rvert$ (meV)	0.061	—	0.029	0.051,0.061	0.017,0.020	0.008	0.040	—
$\lvert\vec{K}\rvert$ (meV)	0.013	—	0.033	0.047,0.045	0.047,0.045	0.018	0.102	0.199
$\lvert\vec{D}\rvert$ (meV)	—	—	0.193	—	0.179,0.203	—	—	0.224

Table B.2: IEI parameters by the magnetic force theorem within HI approximation. The isotropic and anisotropic contributions are extracted from the estimated IEI tensors by assuming the parametrization proposed in Eqs. 4.1 and 4.2.

Coming back to the main issue here, we have found out that the incorrect sign of the isotropic term in the first NN exchange coupling cannot be attributed to an improper choice of the exchange-correlation functional within the DFT framework or the U/J_H ratio. However, Refs. [62,71] claim that these systems require a more advanced treatment of the X p orbitals. Indeed, one shows that the 1°NN FM exchange coupling is not governed by the standard 90°-oriented Goodenough-Kanamori rule but a non-negligible contribution from superexchange mechanisms involving higher-order hopping processes, while the latter demonstrates that the incoming error may be ascribed to the exclusion of X p orbitals from the wannierization step.

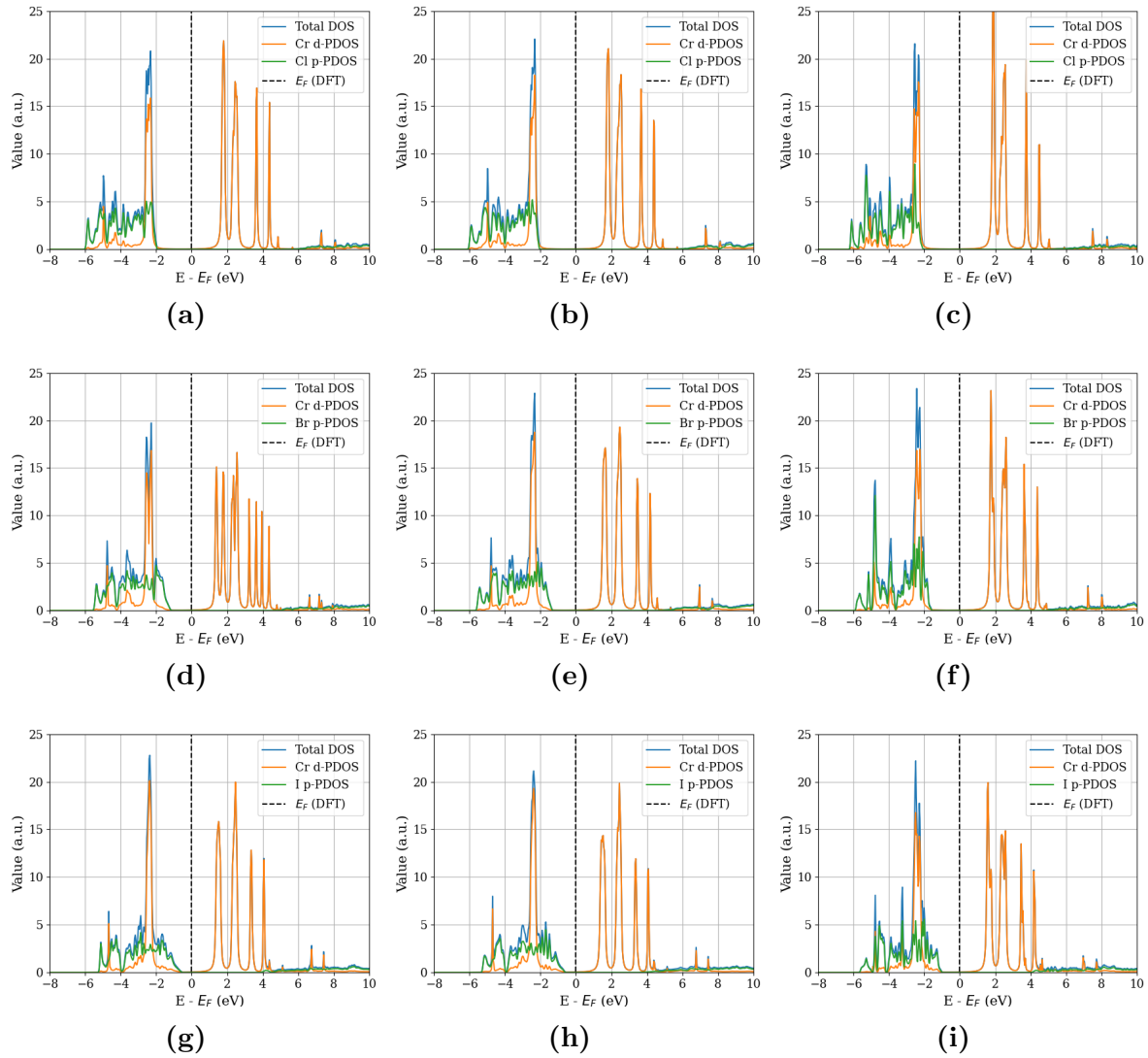

Figure B.1: Partial and total electronic DOS for all the CrX_3 phases. The first three plots **(a)-(b)-(c)** are referred to $CrCl_3$, while the second **(d)-(e)-(f)** and third triplets **(g)-(h)-(i)** respectively to $CrBr_3$ and CrI_3. From left to right instead we pass from the rhombohedral and the monoclinic bulk phases to the trigonal MLs.

For example, if we include the Cl p orbitals into the localized basis for the $CrCl_3$ rhombohedral bulk phase, the shape of the lowest-energy Cr d band is no longer featured by a sharp peak, but rather it is broadened by the surrounding Cl p band as shown in Fig. In order to restore the typical behaviour of ground-state peaks within HI approximation the X p band is artificially shifted down in energy.

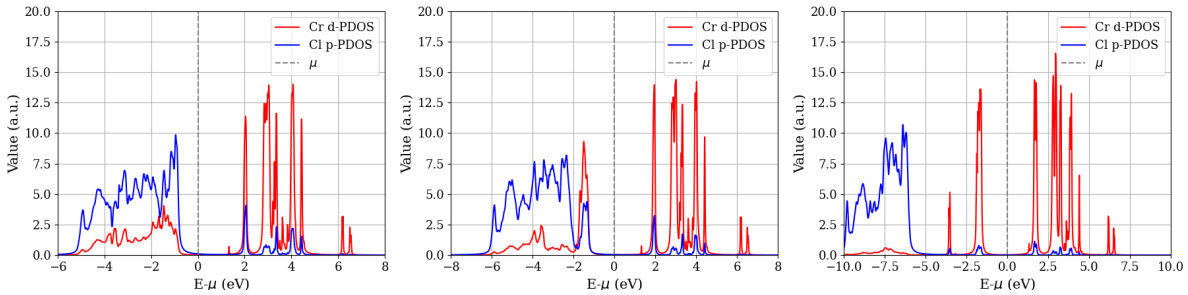

(a) **(b)** **(c)**

Figure B.2: Partial DOS for bulk $CrCl_3$ with shifted Cl p band. The plots in **(a)**, **(b)** and **(c)** differ by the size of the energy shift applied to the Cl p band, respectively 0, -1 eV and -5 eV.

The isotropic component of the resulting 1°NN IEI tensors is reported in Tab. B.3, but the agreement with the FM expectation does not improve. It even gets worse when the quasi-atomic limit is restored by artificially shifting down the Cl p band.

$\Delta\Sigma_p$ (eV)	0	-1	-5
$\bar{J}_1$ (meV)	7.673	9.429	15.86

Table B.3: 1°NN isotropic exchange coupling as a function of $\Delta\Sigma_p$ for bulk $CrCl_3$.

Bibliography

[1] K. S. Novoselov, A. K. Geim, S. V. Morozov, D. Jiang, Y. Zhang, S. V. Dubonos, I. V. Grigorieva and A. A. Firsov . Electric field effect in atomically thin carbon films. *Science*, 306(5696):666–669, 2004. URL: https://www.science.org/doi/abs/10.1126/science.1102896, arXiv: https://www.science.org/doi/pdf/10.1126/science.1102896, doi:10.1126/science.1102896.

[2] Sachs, B. and Wehling, T. O. and Novoselov, K. S. and Lichtenstein, A. I. and Katsnelson, M. I. Ferromagnetic two-dimensional crystals: Single layers of K_2CuF_4. *Physical Review B*, 88:201402, Nov 2013. URL: https://link.aps.org/doi/10.1103/PhysRevB.88.201402, doi:{10.1103/PhysRevB.88.201402}.

[3] Huang, Bevin and Clark, Genevieve and Navarro-Moratalla, Efrén and Klein, Dahlia and Cheng, Ran and Seyler, Kyle L. and Zhong, Ding and Schmidgall, Emma McGuire, Michael A. and Cobden, David H. and Yao, Wang and Xiao, Di and Jarillo-Herrero, Pablo and Xu, Xiaodong. Layer-dependent ferromagnetism in a van der Waals crystal down to the monolayer limit. *Nature*, 546:270–273, 2017.

[4] Cheng Gong, Lin Li, Zhenglu Li, Huiwen Ji, Alex Stern, Yang Xia, Ting Cao, Wei Bao, Chenzhe Wang, Yuan Wang, Z. Q. Qiu, R. J. Cava, Steven G. Louie, Jing Xia, and Xiang Zhang. Discovery of intrinsic ferromagnetism in two-dimensional van der waals crystals. *Nature*, 546(7657):265–269, 2017. URL: https://doi.org/10.1038/nature22060, doi:{10.1038/nature22060}.

[5] Sarah Jenkins, Levente Rózsa, Unai Atxitia, Richard F. L. Evans, Kostya S. Novoselov, and Elton J. G. Santos. Breaking through the mermin-wagner limit in 2d van der waals magnets. *Nature Communications*, 13(1):6917, 2022. URL: https://doi.org/10.1038/s41467-022-34389-0, doi:{10.1038/s41467-022-34389-0}.

[6] Kong, Tai and Stolze, Karoline and Timmons, Erik I. and Tao, Jing and Ni, Danrui and Guo, Shu and Yang, Zoë and Prozorov, Ruslan and Cava, Robert J. VI3—a New Layered Ferromagnetic Semiconductor. *Advanced Materials*, 31(17):1808074, 2019. URL: https://onlinelibrary.wiley.com/doi/abs/10.1002/adma.201808074,

arXiv:https://onlinelibrary.wiley.com/doi/pdf/10.1002/adma.201808074, doi:10.1002/adma.201808074.

[7] Yujun Deng, Yijun Yu, Yichen Song, Jingzhao Zhang, Nai Zhou Wang, Zeyuan Sun, Yangfan Yi, Yi Zheng Wu, Shiwei Wu, Junyi Zhu, Jing Wang, Xian Hui Chen, and Yuanbo Zhang. Gate-tunable room-temperature ferromagnetism in two-dimensional Fe_3GeTe_2. *Nature*, 563(7729):94–99, November 2018. URL: https://doi.org/10.1038/s41586-018-0626-9, doi:{10.1038/s41586-018-0626-9}.

[8] Xingdan Sun, Wanying Li, Xiao Wang, Qi Sui, Tongyao Zhang, Zhi Wang, Long Liu, Da Li, Shun Feng, Siyu Zhong, Hanwen Wang, Vincent Bouchiat, Manuel Nunez Regueiro, Nicolas Rougemaille, Johann Coraux, Anike Purbawati, Abdellali Hadj-Azzem, Zhenhua Wang, Baojuan Dong, Xing Wu, Teng Yang, Guoqiang Yu, Bingwu Wang, Zheng Han, Xiufeng Han, and Zhidong Zhang. Room temperature ferromagnetism in ultra-thin van der Waals crystals of 1T-$CrTe_2$. *Nano Research*, 13(12):3358–3363, December 2020. URL: https://doi.org/10.1007/s12274-020-3021-4, doi:{10.1007/s12274-020-3021-4}.

[9] Erik Koch. Exchange mechanisms. In *Orbital Physics in Correlated Matter*, volume 13 of *Modeling and Simulation*, pages 5.1–31, Jülich, Sep 2023. Autumn School on Correlated Electrons, Jülich (Germany), 18 Sep 2023 - 22 Sep 2023, Forschungszentrum Jülich. URL: https://juser.fz-juelich.de/record/1018555, doi:{10.34734/FZJ-2023-04883}.

[10] John B. Goodenough. Theory of the Role of Covalence in the Perovskite-Type Manganites [La, M(II)]MnO_3. *Physical Review*, 100:564–573, Oct 1955. URL: https://link.aps.org/doi/10.1103/PhysRev.100.564, doi:{10.1103/PhysRev.100.564}.

[11] John B. Goodenough. An interpretation of the magnetic properties of the perovskite-type mixed crystals La1-xSrxCoO3-λ. *Journal of Physics and Chemistry of Solids*, 6(2):287–297, 1958. URL: https://www.sciencedirect.com/science/article/pii/0022369758901070, doi:{https://doi.org/10.1016/0022-3697(58)90107-0}.

[12] Junjiro Kanamori. Superexchange interaction and symmetry properties of electron orbitals. *Journal of Physics and Chemistry of Solids*, 10(2):87–98, 1959. URL: https://www.sciencedirect.com/science/article/pii/0022369759900617, doi:{https://doi.org/10.1016/0022-3697(59)90061-7}.

[13] I. Dzyaloshinskii. A thermodynamic theory of weak ferromagnetism of antiferromagnetics. *Journal of Physics and Chemistry of Solids*, 4(4):241–255, 1958. URL: https://www.sciencedirect.com/science/article/pii/0022369758900763, doi:{https://doi.org/10.1016/0022-3697(58)90076-3}.

[14] T. Moriya. Anisotropic superexchange interaction and weak ferromagnetism. *Physical Review*, 120:91–98, Oct 1960. URL: https://link.aps.org/doi/10.1103/PhysRev.120.91, doi:{10.1103/PhysRev.120.91}.

[15] N. D. Mermin and H. Wagner. Absence of Ferromagnetism or Antiferromagnetism in One- or Two-Dimensional Isotropic Heisenberg Models. *Physical Review Letters*, 17:1133–1136, Nov 1966. URL: https://link.aps.org/doi/10.1103/PhysRevLett.17.1133, doi:{10.1103/PhysRevLett.17.1133}.

[16] P. Hohenberg and W. Kohn. Inhomogeneous electron gas. *Physical Review*, 136:B864–B871, Nov 1964. URL: https://link.aps.org/doi/10.1103/PhysRev.136.B864, doi:10.1103/PhysRev.136.B864.

[17] W. Kohn and L. J. Sham. Self-Consistent Equations Including Exchange and Correlation Effects. *Physical Review*, 140:A1133–A1138, Nov 1965. URL: https://link.aps.org/doi/10.1103/PhysRev.140.A1133, doi:10.1103/PhysRev.140.A1133.

[18] G. Kresse and J. Hafner. Ab initio molecular-dynamics simulation of the liquid-metal-amorphous-semiconductor transition in germanium. *Physical Review B*, 49, May 1994. doi:10.1103/PhysRevB.49.14251.

[19] G. Kresse and J. Furthmümuller. Efficiency of ab-initio total energy calculations for metals and semiconductors using a plane-wave basis set. *Computational Materials Science*, 6:15–50, Jul 1996. doi:10.1016/0927-0256(96)00008-0.

[20] G. Kresse and J. Furthmümuller. Efficient iterative schemes for ab initio total-energy calculations using a plane-wave basis set. *Physical Review B*, 54, Oct 1996. doi:10.1103/PhysRevB.54.11169.

[21] John P. Perdew, Kieron Burke, and Matthias Ernzerhof. Generalized gradient approximation made simple. *Phys. Rev. Lett.*, 77:3865–3868, Oct 1996. URL: https://link.aps.org/doi/10.1103/PhysRevLett.77.3865, doi:10.1103/PhysRevLett.77.3865.

[22] A. Ruzsinszky J. Sun and J. P. Perdew. Strongly constrained and appropriately normed semilocal density functional. *Physical Review Letters*, 115:036402, Jul 2015. URL: https://link.aps.org/doi/10.1103/PhysRevLett.115.036402, doi:10.1103/PhysRevLett.115.036402.

[23] Aliaksandr V. Krukau, Oleg A. Vydrov, Artur F. Izmaylov, and Gustavo E. Scuseria. Influence of the exchange screening parameter on the performance of screened hybrid functionals. *The Journal of Chemical Physics*, 125(22):224106, 12 2006. doi:10.1063/1.2404663.

[24] C. Adamo and V. Barone. Toward reliable density functional methods without adjustable parameters: The PBE0 model. *The Journal of Chemical Physics*, 110(13):6158–6170, 04 1999. doi:10.1063/1.478522.

[25] P. J. Stephens, F. J. Devlin, C. F. Chabalowski, M. J. Frisch. Ab initio calculation of vibrational absorption and circular dichroism spectra using density functional force fields. *The Journal of Physical Chemistry*, 98:11623–11627, Nov 1994. doi:10.1021/j100096a001.

[26] A. I. Liechtenstein, V. I. Anisimov and J. Zaanen. Density-functional theory and strong interactions: Orbital ordering in Mott-Hubbard insulators. *Physical Review B*, 52:R5467–R5470, Aug 1995. URL: https://link.aps.org/doi/10.1103/PhysRevB.52.R5467, doi:10.1103/PhysRevB.52.R5467.

[27] S. L. Dudarev, G. A. Botton, S. Y. Savrasov, C. J. Humphreys and A. P. Sutton. Electron-energy-loss spectra and the structural stability of nickel oxide: An LSDA+U study. *Physical Review B*, 57:1505–1509, Jan 1998. URL: https://link.aps.org/doi/10.1103/PhysRevB.57.1505, doi:10.1103/PhysRevB.57.1505.

[28] M. S. Hybertsen and S. G. Louie. Electron correlation in semiconductors and insulators: Band gaps and quasiparticle energies. *Physical Review B*, 34:5390–5413, Oct 1986. URL: https://link.aps.org/doi/10.1103/PhysRevB.34.5390, doi:10.1103/PhysRevB.34.5390.

[29] A. I. Lichtenstein and M. I. Katsnelson. Ab initio calculations of quasiparticle band structure in correlated systems: LDA++ approach. *Physical Review B*, 57:6884–6895, Mar 1998. URL: https://link.aps.org/doi/10.1103/PhysRevB.57.6884, doi:10.1103/PhysRevB.57.6884.

[30] P. Ma and S. L. Dudarev. Constrained density functional for noncollinear magnetism. *Physical Review B*, 91:054420, Feb 2015. URL: https://link.aps.org/doi/10.1103/PhysRevB.91.054420, doi:10.1103/PhysRevB.91.054420.

[31] H. J. Xiang, E. J. Kan, S. Wei, M. H. Whangbo and X. G. Gong. Predicting the spin-lattice order of frustrated systems from first principles. *Physical Review B*, 84:224429, Dec 2011. URL: https://link.aps.org/doi/10.1103/PhysRevB.84.224429, doi:10.1103/PhysRevB.84.224429.

[32] Xiang, Hongjun and Lee, Changhoon and Koo, Hyun-Joo and Gong, Xingao and Whangbo, Myung-Hwan. Magnetic properties and energy-mapping analysis. *Dalton Trans.*, 42:823–853, 2013. URL: http://dx.doi.org/10.1039/C2DT31662E, doi:10.1039/C2DT31662E.

[33] D. Sabani, C. Bacaksiz and M. V. Milosevic. Ab initio methodology for magnetic exchange parameters: Generic four-state energy mapping onto a Heisenberg spin Hamiltonian. *Physical Review B*, 102, Jul 2020. doi:10.1103/PhysRevB.102.014457.

[34] L. V. Pourovskii. Two-site fluctuations and multipolar intersite exchange interactions in strongly correlated systems. *Physical Review B*, 94, Sep 2016. doi:10.1103/PhysRevB.94.115117.

[35] D. F. Mosca, H. Schnait, L. Celiberti, M. Aichhorn, C. Franchini. The Mott transition in the 5d 1 compound Ba 2 NaOsO 6 : A DFT+DMFT study with PAW spinor projectors. *Computational Materials Science*, 233, Jan 2024. doi:10.1016/j.commatsci.2023.112764.

[36] B. Skubic, J. Hellsvik, L. Nordström and O Eriksson. A method for atomistic spin dynamics simulations: implementation and examples. *Journal of Physics: Condensed Matter*, 20(31):315203, Jul 2008. URL: https://dx.doi.org/10.1088/0953-8984/20/31/315203, doi:{10.1088/0953-8984/20/31/315203}.

[37] V. P. Antropov, M. I. Katsnelson, B. N. Harmon, M. van Schilfgaarde and D. Kusnezov. Spin dynamics in magnets: Equation of motion and finite temperature effects. *Physical Review B*, 54:1019–1035, Jul 1996. URL: https://link.aps.org/doi/10.1103/PhysRevB.54.1019, doi:{10.1103/PhysRevB.54.1019}.

[38] García-Palacios, JoséL. and Lázaro, Francisco J. Anisotropy effects on the nonlinear magnetic susceptibilities of superparamagnetic particles. *Physical Review B*, 55:1006–1010, Jan 1997. URL: https://link.aps.org/doi/10.1103/PhysRevB.55.1006, doi:{10.1103/PhysRevB.55.1006}.

[39] L. Bergqvist O. Eriksson, A. Bergman and J. Hellsvik. *Atomistic Spin Dynamics: Foundations and Applications*. Oxford University Press, 02 2017. URL: https://doi.org/10.1093/oso/9780198788669.001.0001, doi:{10.1093/oso/9780198788669.001.0001}.

[40] N. Metropolis, A. W. Rosenbluth, M. N. Rosenbluth, A. H. Teller and E. Teller. Equation of state calculations by fast computing machines. *The Journal of Chemical Physics*, 21(6):1087–1092, 06 1953. URL: https://doi.org/10.1063/1.1699114, arXiv:{https://pubs.aip.org/aip/jcp/article-pdf/21/6/1087/18802390/1087_1_online.pdf}, doi:{10.1063/1.1699114}.

[41] B. Morosin and A. Narath. X-Ray Diffraction and Nuclear Quadrupole Resonance Studies of Chromium Trichloride. *J. Chem. Phys.*, 40, Apr 1964. doi:10.1063/1.1725428.

[42] S. Yang, X. Xu*, B. Han, P. Gu, R. Guzman, Y. Song, Z. Lin, P. Gao, W. Zhou, J. Yang, Z. Chen, and Y. Ye. Controlling the 2D Magnetism of CrBr3 by van der Waals Stacking Engineering. *J. Am. Chem. Soc.*, 145, Dec 2023. doi:10.1021/jacs.3c10777.

[43] M. A. McGuire, H. Dixit, V. R. Cooper and B. C. Sales. Coupling of Crystal Structure and Magnetism in the Layered, Ferromagnetic Insulator CrI3. *Chem. Mat.*, 27, Dec 2015. doi:10.1021/cm504242t.

[44] K. Momma and F. Izumi. An integrated three-dimensional visualization system VESTA using wxWidgets. *Commission on Crystallographic Computing, IUCr Newsletter*, 7, Nov 2006.

[45] K. Momma and F. Izumi. Three-Dimensional Visualization in Powder Diffraction. *Solid State Phenomena*, 130, 2007. doi:10.4028/www.scientific.net/SSP.130.

[46] K. Momma and F. Izumi. VESTA: a three-dimensional visualization system for electronic and structural analysis. *Journal of Applied Crystallography*, 41, 2008. doi:10.1107/S0021889808012016.

[47] K. Momma and F. Izumi. VESTA 3 for three-dimensional visualization of crystal, volumetric and morphology data. *Journal of Applied Crystallography*, 44, 2011. doi:10.1107/S0021889811038970.

[48] W. Chen, Z. Sun, Z. Wang, L. Gu, X. Xu, S. Wu and C. Gao . Direct observation of van der waals stacking–dependent interlayer magnetism. *Science*, 366(6468):983–987, 2019. URL: https://www.science.org/doi/abs/10.1126/science.aav1937, arXiv:{https://www.science.org/doi/pdf/10.1126/science.aav1937}, doi:{10.1126/science.aav1937}.

[49] S. Lu, D. Guo, Z. Cheng, Y. Guo, C. Wang, J. Deng, Y. Bai, C. Tian, L. Zhou, Y. Shi, J. He, W. Ji and C. Zhang. Controllable dimensionality conversion between 1d and 2d crcl3 magnetic nanostructures. *Nature Communications*, 14, 2023. URL: https://doi.org/10.1038/s41467-023-38175-4, doi:{10.1038/s41467-023-38175-4}.

[50] I. Pollini. Electron correlations and hybridization in chromium compounds. *Solid State Communications*, 106(8):549–554, 1998. URL: https://www.sciencedirect.com/science/article/pii/S0038109898000349, doi:10.1016/S0038-1098(98)00034-9.

[51] W. Zhang, Q. Qu, P. Zhu and C. Lam. Robust Intrinsic Ferromagnetism and Half Semiconductivity in Stable Two-Dimensional Single-Layer Chromium Trihalides. *Journal of Materials Chemistry C*, 3, Nov 2015. doi:10.1039/C5TC02840J.

[52] Tsubokawa Ichiro. On the magnetic properties of a crbr3 single crystal. *Journal of the Physical Society of Japan*, 15(9):1664–1668, 1960. URL: https://doi.org/10.1143/JPSJ.15.1664, arXiv:{https://doi.org/10.1143/JPSJ.15.1664}, doi:{10.1143/JPSJ.15.1664}.

[53] Dillon, J. F., Jr. and Olson, C. E. Magnetization, resonance, and optical properties of the ferromagnet cri3. *Journal of Applied Physics*, 36(3):1259–1260, 03 1965. URL: https://doi.org/10.1063/1.1714194, arXiv:{https://pubs.aip.org/aip/jap/article-pdf/36/3/1259/18334605/1259_1_online.pdf}, doi:{10.1063/1.1714194}.

[54] J.W. Cable, M.K. Wilkinson, and E.O. Wollan. Neutron diffraction investigation of antiferromagnetism in crcl3. *Journal of Physics and Chemistry of Solids*, 19(1):29–34, 1961. URL: https://www.sciencedirect.com/science/article/pii/0022369761900531, doi:{https://doi.org/10.1016/0022-3697(61)90053-1}.

[55] A. Bedoya-Pinto, J. Ji, A. K. Pandeya, P. Gargiani, M. Valvidares, P. Sessi, J. M. Taylor, F. Radu, K. Chang and S. S. P. Parkin . Intrinsic 2D-XY ferromagnetism in a van der Waals monolayer. *Science*, 374(6567):616–620, 2021. URL: https://www.science.org/doi/abs/10.1126/science.abd5146, arXiv:{https://www.science.org/doi/pdf/10.1126/science.abd5146}, doi:{10.1126/science.abd5146}.

[56] Z. Zhang, J. Shang, C. Jiang, A. Rasmita, W. Gao and T. Yu. Direct Photoluminescence Probing of Ferromagnetism in Monolayer Two-Dimensional CrBr3. *Nano Letters*, 19(5):3138–3142, 2019. PMID: 30945874. URL: https://doi.org/10.1021/acs.nanolett.9b00553, arXiv:{https://doi.org/10.1021/acs.nanolett.9b00553}, doi:{10.1021/acs.nanolett.9b00553}.

[57] S. Jiang, L. Li, Z. Wang, K. F. Mak and J. Shan. Controlling magnetism in 2d cri3 by electrostatic doping. *Nature Nanotechnology*, 13:549–553, 2018. URL: https://doi.org/10.1038/s41565-018-0135-x, doi:{10.1038/s41565-018-0135-x}.

[58] John P. Perdew, Adrienn Ruzsinszky, Gábor I. Csonka, Oleg A. Vydrov, Gustavo E. Scuseria, Lucian A. Constantin, Xiaolan Zhou, and Kieron Burke. Restoring the density-gradient expansion for exchange in solids and surfaces. *Phys. Rev. Lett.*, 100:136406, Apr 2008. URL: https://link.aps.org/doi/10.1103/PhysRevLett.100.136406, doi:10.1103/PhysRevLett.100.136406.

[59] Inducing magnetic phase transitions in monolayer cri3 via lattice deformations.

[60] Y. O. Kvashnin, A. Bergman, A. I. Lichtenstein and M. I. Katsnelson. Relativistic exchange interactions in CrX3 (X = Cl, Br, I) monolayers. *Physical Review B*, 102, Sep 2020. doi:10.1021/cm504242t.

[61] Péter Pulay. Convergence acceleration of iterative sequences. the case of scf iteration. *Chemical Physics Letters*, 73(2):393–398, 1980. URL: https://www.sciencedirect.com/science/article/pii/0009261480803964, doi:{https://doi.org/10.1016/0009-2614(80)80396-4}.

[62] D. Soriano, A. N. Rudenko, M. I. Katsnelson and M. Rösner. Environmental screening and ligand-field effects to magnetism in CrI 3 monolayer. *Compuational Materials*, 162, 2021. doi:10.1038/s41524-021-00631-4.

[63] I. Lee, J. Cen, O. Molchanov, S. Feng, W. L. Huey, J. van Tol, J. E. Goldberger, N. Trivedi, H.-Y. Kee and P. C. Hammel. Spin-orbit coupling controlled two-dimensional magnetism in chromium trihalides, 2024. URL: https://arxiv.org/abs/2405.16709, arXiv:2405.16709.

[64] P. Blaha, K. Schwarz, F. Tran, R. Laskowski, G. K. H. Madsen and L. D. Marks. WIEN2k: An APW+lo program for calculating the properties of solids. *J. Chem. Phys.*, 152, Feb 2020. doi:10.1063/1.5143061.

[65] M. Aichhorn, L. Pourovskii, P. Seth, V. Vildosola, M. Zingl, O. E. Peil, X. Deng, J. Mravlje, G. J. Kraberger, C. Martins, M. Ferrero, O. Parcollet. TRIQS/DFTTools: A TRIQS application for ab initio calculations of correlated materials. *Computer Physics Communications*, 204, Jul 2016. doi:10.1016/j.cpc.2016.03.014.

[66] M. Aichhorn, L. Pourovskii and A. Georges. Importance of electronic correlations for structural and magnetic properties of the iron pnictide superconductor LaFeAsO. *Physical Review B*, 84, Aug 2011. doi:10.1103/PhysRevB.84.054529.

[67] M. Aichhorn, L. Pourovskii, V. Vildosola, M. Ferrero, O. Parcollet, T. Miyake, A. Georges and S. Biermann. Dynamical mean-field theory within an augmented plane-wave framework: Assessing electronic correlations in the iron pnictide LaFeAsO. *Physical Review B*, 80, Aug 2009. doi:10.1103/PhysRevB.80.085101.

[68] G. Kresse and J. Hafner. Norm-conserving and ultrasoft pseudopotentials for first-row and transition elements. *Journal of Physics: Condensed Matter*, 6(40):8245, oct 1994. URL: https://dx.doi.org/10.1088/0953-8984/6/40/015, doi:{10.1088/0953-8984/6/40/015}.

[69] Blöchl, P. E. Projector augmented-wave method. *Physical Review B*, 50:17953–17979, Dec 1994. URL: https://link.aps.org/doi/10.1103/PhysRevB.50.17953, doi:{10.1103/PhysRevB.50.17953}.

[70] Jiří Klimeš, David R Bowler, and Angelos Michaelides. Chemical accuracy for the van der waals density functional. *Journal of Physics: Condensed Matter*,

22(2):022201, dec 2009. URL: https://dx.doi.org/10.1088/0953-8984/22/2/022201, doi:10.1088/0953-8984/22/2/022201.

[71] K. W. Song and V. I. Fal'ko. Superexchange and spin-orbit coupling in monolayer and bilayer chromium trihalides. *Physical Review B*, 106, Dec 2022. doi:10.1103/PhysRevB.106.245111.